THERMAL DESORPTION ANALYSIS OF HELIUM TRAPPING IN ION-IMPLANTED BERYLLIUM

By

YAHYA MOUNIR ZAKARIA, B.Sc., M.Sc.

A Thesis

Submitted to the School of Graduate Studies

in Partial Fulfilment of the Requirements

for the Degree

Doctor of Philosophy

McMaster University

DOCTOR OF PHILOSOPHY (1996)
(Engineering Physics)

McMASTER UNIVERSITY
Hamilton, Ontario

TITLE: Thermal Desorption Analysis of Helium Trapping in Ion-Implanted Beryllium.

AUTHOR: Yahya Mounir Zakaria, B.Sc. (Department of Nuclear Engineering, Alexandria University, Egypt)
M.Sc. (Department of Engineering Physics, Alexandria University, Egypt)

SUPERVISOR: Professor D.A. Thompson

NUMBER OF PAGES: xii, 159

THERMAL RELEASE OF HELIUM FROM ION-IMPLANTED BERYLLIUM

Acknowledgements

With deep gratitude I wish to express my sincere appreciation to my supervisor, Professor David A. Thompson, for his suggestion of this problem and his continued support and understanding throughout the entire course of this work. The helpful suggestions and encouragement of Professor John A. Davies and Professor Archie A. Harms, who were both members of my supervisory committee, are gratefully acknowledged.

I am especially grateful to Dr. Richard G. Macaulay-Newcombe for instructing me from the first day I started my experiments, for our many valuable discussions and for his instrumental association in helping me bringing this thesis towards a successful completion.

Thanks are also due to Ms. Doris Stevanovic for her endless patience in carrying out the ion implantations and to J. Hudak for the scanning electron microscopy.

The financial assistance provided by McMaster University and the Engineering Physics Department, through a Teaching assistantship, is gratefully appreciated.

Finally, I wish to acknowledge the role of my family in making it all possible. The prayers of my parents and sister back home were a great blessing. The moral support, understanding and friendship of my wife, Mayssa, and the smiles and joy from our son, Yaser, were my real motivation during our "cold" days in Canada. Without you this pilgrimage could not even have been attempted and to you I dedicate this thesis with all my love.

Abstract

Trapping of 30 keV ion-implanted helium by the radiation-produced damage in hot isostatic pressed beryllium foils of 99.5 wt% purity has been investigated by a series of ion implantation/thermal desorption experiments. Different experimental regimes were designed to obtain some fundamental insight into the behaviour of helium in beryllium. The helium release was related to the surface morphology changes observed on the desorbed surfaces by scanning electron microscopy.

The nature of helium trapping in beryllium has been found to strongly depend on the implantation parameters as well as on the thermal treatment of the implanted samples. Desorption peaks have been analyzed in terms of the dissociation of simple helium-vacancy trapping centres and/or helium release from microbubbles that nucleate and grow during the annealing of the implanted samples.

Linear-ramp annealing following room-temperature 30 keV He^+ implantation in beryllium to a total fluence in the range of 10^{20} to 10^{21} $/m^2$ has produced two desorption stages above 890 K and below 830 K, respectively. The high temperature desorption peak was analyzed in terms of a first-order dissociation mechanism with an activation energy that depends on the relative

occupation of the trapping site. The low temperature peak corresponds to a higher-order helium-vacancy cluster that begins to fill once the deeper trapping site approaches saturation. A third trapping site, with higher dissociation energy, has been inferred from the fact that a sizeable fraction of the implanted helium has not been released after heating up to 75% of the melting temperature.

Some samples have been heated by a stepped anneal regime, for two hours at 573 or 773 K, that allows reconfiguration of the trapped helium before being desorbed. The release spectra and the desorbed surface morphology show that the nature of helium trapping has changed to a more stable form of helium bubbles. A model is proposed to account for the helium bubble nucleation and growth by a migration and coalescence mechanism. Linearly ramped thermal desorption after high temperature implantations at 600 and 773 K reveals the formation of more stable trapping sites. The helium release has been related to the formation of holes on the surface and the desorption was inferred to result from microbubble growth by thermal vacancy assisted mechanism.

Some of the samples have been deliberately corroded to investigate the effect of the surface contamination on the helium release. The desorption curves show the formation of an additional broad desorption peak at temperatures higher than 950 K. This is associated with a relative drop in the population of the primary and secondary desorption peaks and implies that the corroded surface contains additional trapping sites that delay the release of the helium detrapped from the bulk.

TABLE OF CONTENTS

List of Figures

List of Tables

CHAPTER 1

Introduction

Helium is an inevitable by-product of the irradiation of reactor structural materials with energetic neutrons. In fusion reactor devices, helium may accumulate at a rate of several hundred atomic parts per million per year in the heavily irradiated first wall and blanket components. The energy of solution of helium in crystalline solids is large and, since helium does not form chemical compounds with its host, it tends to accumulate at pre-existing or radiation-induced crystal defects. Helium is expected to become preferentially bound with vacancies. Theoretical investigations indicate that the binding energy of helium atoms with metal vacancies is greater than about 2 eV and is stronger than binding with other helium atoms, self interstitial atoms, impurities and dislocations. Still, helium achieves its lowest energy state in bubbles which weaken grain boundaries and are known to be the major reason for high temperature embrittlement and surface blister formation. Understanding the behaviour of helium in fusion reactor candidate materials is therefore imperative to face the anticipated technological problems of such devices.

The interest in beryllium as a plasma-facing material for fusion energy

reactors has increased significantly in the last several years. This interest has been driven by the material's low atomic number, its good thermal characteristics and its ability to getter oxygen in the plasma environment. Beryllium has long been proposed as a neutron multiplier in the blanket of fusion reactors and the results from the "beryllium phase" in experimental reactors has proven to be promising. However there is still a strong need for data on a number of practical aspects; one of them is understanding the helium behaviour in beryllium at the temperatures of design interest. Very few studies have been performed in this area and many of these studies have targeted the swelling effects of helium rather than the preceding stages of helium trapping and the growth mechanisms of helium bubbles.

Thermal desorption spectroscopy (TDS) has proved to be a powerful method of studying the basic processes associated with the introduction of helium to metallic lattices. On the basis of such studies, four critical parameters have been defined, namely: the ion fluence, the implantation temperature, the presence of gas sinks (*e.g.*, the surface) in the vicinity of the region in which the helium is deposited and the annealing procedure through which the implanted sample is desorbed. In the present work, the TDS technique has been used to study the trapping of 30 keV helium implanted into hot isostatic pressed (HIP) polycrystalline beryllium samples as a function of these parameters. Variation of the annealing regime has been accomplished by changing the ramping rate as well as by using a step-annealing approach. The ion energy used results in an implantation range well within the material bulk, hence eliminating the interference of surface effects on the trapping of the injected helium.

Chapter 2 presents a literature review on the behaviour of helium in metals. The presentation is organized into two parts covering the topics of defect trapping in helium implanted metals and the nucleation and growth of helium bubbles during annealing, both are directly related to the results presented in this work. These two subjects are separated since they belong to different theoretical backgrounds, yet both are linked by the fact that simple trapping is the precursor process for bubble formation. Chapter 3 deals with the different analysis procedures for thermal desorption spectra. Although the usage of complete methods, with no or minimal assumptions are preferable, some easier methods that utilize approximations can be justified based on the TDS results. The experimental procedures and apparatus used in the present thesis are described in detail in Chapter 4 and the results and analysis of the TDS experiments and surface morphology observations by Scanning Electron Microscopy (SEM) are given in Chapter 5. Finally, the conclusions and recommendations of the present study are summarized in Chapter 6.

CHAPTER 2

Helium Behaviour in Metals

Part I. Transport and Defect Trapping of Helium in Metals

2.1. Introduction

The properties of single helium atoms or small clusters in a metal lattice are the basis for any fundamental understanding of helium effects. Precipitation of helium in irradiated metals, even at low concentrations, assists the nucleation and growth of cavities. This is considered as one of the lifetime determining processes in structural components of the proposed fusion reactors. The configuration energies of helium atoms within the host lattice are the crucial parameters for studying helium behaviour in metals since they determine the solubility, the paths of diffusion, the trapping to defects and the early stages of cluster formation. Theoretical calculations of these energies have been tackled successfully by computer simulation of model crystals in which the atoms interact via suitably chosen interatomic potentials. Different experimental techniques are applied to investigate these theoretical predictions and the helium behaviour has been found generally to depend on the method of its introduction to metals.

Helium is known to have a negligible solubility in metals [Ullmaier 1983]. It is usually introduced into metals by energetic processes, such as ion-implantation, nuclear transmutation from neutron bombardment or by using the "tritium trick": natural tritium decay to ^{3}He. The first two techniques are usually associated with the creation of radiation damage which can strongly trap the injected atoms, preventing the study of pure lattice helium mobility and the interaction of helium with intrinsic defects. An exception is sub-threshold ion implantation, where helium is implanted at energies low enough to cause no atomic displacements. However, at such low energies the implanted helium is expected to reside in the near-surface region. For high energy implantation, an understanding of the radiation produced defects is essential to the analysis of helium retention.

The displacement of a lattice atom may result in the formation of a single Frenkel pair, a compact displacement cascade or in a large and more dilute cascade that may incorporate several compact sub-cascades. Primary cascade damage in metals has been investigated by different experimental methods such as transmission electron microscopy (TEM) [Yoshida 1994] as well as by computer simulations using Monte Carlo [Heinisch *et al.* 1993] and molecular dynamics [Foreman *et al.* 1992] techniques. Both types of simulation studies have shown that in cascades, vacancies and self-interstitial atoms (SIAs) are generated in a highly localized and segregated fashion resulting in efficient clustering of both types of defect. In addition, it has been found that at least some of the SIA clusters are mobile.

Helium atoms introduced into a solid can reside in an interstitial position, in a substitutional position, or in clusters of helium within vacancies and vacancy clusters, which at larger sizes are termed cavities. Vacancies have proven essentially to be unsaturable trapping sites for helium due to the reduced electron density that is an energetically favoured environment compared to an interstitial solution site. Furthermore, there is a positive binding energy between a single interstitial helium atom and a helium-vacancy cluster (HeVC) of any size. Thus, a single vacancy will collect several helium atoms and will continue to accept further gas atoms by ejecting SIAs. This process forms the precursor to bubble nucleation and is discussed in detail in the second part of this chapter.

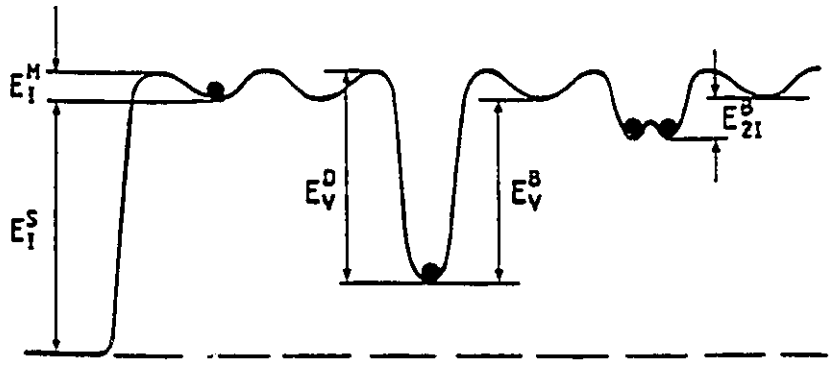

Fig. 2.1. Schematic diagram of helium energies of solution into interstitial sites (E_I^S), interstitial migration (E_I^M), dissociation from vacancy (E_V^D), binding to a vacancy (E_V^B) and binding of two atoms in an interstitial site (E_{2I}^B) [Ullmaier 1983].

Figure 2.1 illustrates the energies of helium atoms at different sites in perfect and imperfect lattices. In order to introduce a helium atom from a gas

phase into an interstitial position, the solution energy for incorporation into an interstitial site, E_I^S, has to be provided. When a helium atom is substitutionally trapped at a vacancy, the binding energy E_V^B is gained. The activation energy for dissociation of a helium atom out of a vacancy is given by $E_V^D = E_V^B + E_I^M$, where E_I^M is the activation energy for migration of an interstitial helium atom. In the following sections of Part I, different atomistic models developed to describe helium trapping and transport in metals are presented followed by a sample of the experimental observations relevant to the present thesis work. Part II is devoted to a review of the literature on helium cluster formation and growth in helium-irradiated metals.

2.2. Atomistics of helium interactions in metals

The earliest work on the configuration of inert gases in metals employed interatomic potentials for the gas-lattice atom interaction which were obtained by averaging the known gas-gas and metal-metal potentials [Rimmer *et al.* 1957]. Table 2.1 presents estimates made for the formation energies of inert gas solutions in copper. The substitutional energy $(E_V^D)_1$ defines the energy barrier for the introduction of a gas atom into a vacancy while $(E_V^D)_2$, which results from direct gas replacement of a lattice atom, requires adding the self-interstitial formation energy to $(E_V^D)_1$. These results show that if helium is injected into a crystal lattice at sub-threshold energies it should reside interstitially or diffuse out of the lattice, depending on its migration energy, unless it is trapped at pre-existing defects. Helium may dissolve substitutionally when vacancies are

available, but not otherwise. However, the averaging procedure used in calculating the gas-lattice interatomic potentials had little theoretical basis and more extensive research was necessary to justify its usage.

Table 2.1
Early estimated energies for solution of inert gases in copper in eV

Solution	He	Ne	Ar	Kr	Xe
Interstitial, E_I^S	2.5	4.6	13.6	19.5	31.0
Substitutional, $(E_V^D)_1$	1.0	1.4	3.9	6.2	11.2
Gas-metal replacement, $(E_V^D)_2$	5.5	5.9	8.4	10.7	15.7

An approximate quantum mechanical model for the incorporation of inert gas atoms in metals was developed [Wilson *et al.* 1971]. The model eliminates averaging and fitting procedures in calculating the gas-metal potentials. Instead, the total energy of interaction between the two charge distributions was determined as the sum of the electron-electron E_{ee}, electron-nuclear E_{en}, nuclear-nuclear E_{nn}, kinetic E_k and exchange E_a energies. The calculated interaction energies were found to be in excellent agreement with all known inert gas diatomic potentials as well as with the short range Cu-Cu potential widely used in defect calculations [Gibson *et al.* 1960]. This model was applied to the calculation of various helium defect configurations in fcc and bcc metals [Wilson *et al.* 1972]. The helium-host lattice potentials were calculated and then calculations of the energies of both helium interstitial migration and detrapping of helium atoms from substitutional sites were presented.

Two independent methods for the helium defect calculations were investigated. In the first method, a symmetrical shell of atoms distributed about the defect configuration was moved to an estimated minimum and the energy change noted. It was then held while the next shell was released. The result was obtained after about six successively smaller iterations usually ending with a final shell shift of about 0.001 of the half lattice constant, r_o. Relaxation of ≈ 200 atoms with a final shift of the size mentioned was sufficient to define the total energy change to within 0.01 eV.

In the second method, all the atoms involved were allowed to move simultaneously. The initial forces on each atom, $F(t_o)$, were calculated from the interatomic potentials at time t_o; then the relaxed coordinates after a time interval $\Delta t = t - t_o$ were computed from a set of equations of the form $x(t) = x(t_o) + [F(t_o)(\Delta t)^2/(2m)]$, so as to give the energy change. Forces at the new coordinates were then computed and the process repeated as many times as necessary to obtain zero force conditions; *i.e.*, reaching a rest position. This usually amounted to ≈ 100 steps. A test comparison between the two methods showed little differences other than in relative computational speeds. As a result, calculations were made with the faster method for each lattice structure, the first method for fcc and the second method for bcc metals.

These methods were used to calculate the formation energies, relative to the perfect lattice, of helium in various interstitial positions. Some of the proposed positions in both fcc and bcc lattices are shown in fig. 2.2. The interstitial migration energy was calculated in each case by taking the difference

between the lowest two interstitial configurations. Generally, E_I^M in bcc metals was $\approx$0.3 eV whereas in the fcc metals the values were less consistent ranging from 0.08 to 1.74 eV. In a similar way, the formation energy of helium in an existing vacancy was calculated for both lattices and the values for E_V^D were found to be consistently high.

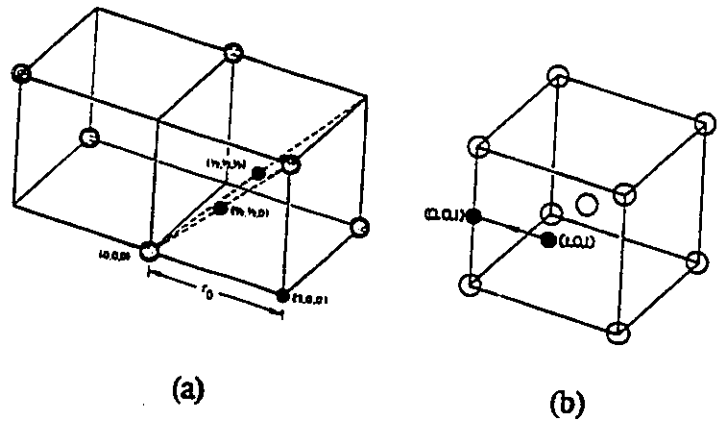

Fig. 2.2. Symmetrical helium interstitial positions in metal lattices. (a) in fcc; (b) in bcc [Wilson *et al.* 1972].

A detailed study of helium diffusion in the fcc-Cu and the bcc-W lattices was carefully done based on the second method [Wilson *et al.* 1973]. The approach was to calculate the energy needed to move a helium atom from a substitutional to an interstitial site by mapping the interstitial energy contours surrounding an existing vacancy. Table 2.2 summarizes some of the predicted energies for helium defects in a number of metals as calculated by the quantum mechanical model.

Table 2.2
Theoretically predicted energies of helium defects in metals in eV

	Cu [a]	W [b]	Al [a]	Ni [a]	Mo [b]
Interstitial solution energy, E_I^S	1.93	5.91	1.32	4.02	4.97
Interstitial migration energy, E_I^M	0.63	0.29	0.33	0.66	0.30
Helium-vacancy dissociation energy, E_V^D	2.76	5.07	1.55	3.29	4.20

[a] Baskes *et al.* (1979).
[b] Picraux (1981).

2.3. Mechanisms for helium transport in irradiated metals

Under irradiation conditions, when helium atoms are introduced concurrently with displacement damage, the diffusion of helium through bulk material is influenced by the following processes: (a) trapping in and thermal detrapping of helium from single vacancies, divacancies and higher order vacancy clusters; (b) helium trapping at intrinsic defects (*e.g.*, dislocations and grain boundaries); (c) replacement of helium bound to single vacancies by SIAs; (d) helium clustering into HeVCs; (e) displacement of trapped helium atoms by irradiation and (f) migration of helium as an interstitial atom or in a highly mobile divacancy.

Because of the complexity of processes involving helium transport, simplified models for helium diffusion in metals have previously been developed. For example, one model considered the thermal detrapping of helium from radiation produced vacancies as the only phenomenon contributing to the diffusion

process [Reed 1977]. In this case, the effective helium diffusion coefficient is expressed as

$$D_{He}^{eff} = \nu_{He} \frac{\lambda^2}{6} C_V^{-2/3} \exp(-E_V^D / kT) \quad , \qquad (2.1)$$

where ν_{He} is the helium jump frequency, λ is the jump distance and C_V is the thermal equilibrium vacancy concentration. Other approaches have related the increase in the void nucleation rates in irradiated metals to the presence of mobile helium atoms [Wiedersich *et al.* 1974 and 1977]. In these studies, however, the opposite effect of how the cluster formation affects the migration of helium atoms was not considered.

For a fuller understanding of helium diffusion under homogeneous point defect production two main mechanisms have been proposed: (a) interstitial diffusion between detrapping from and retrapping by vacancies [Ghoniem *et al.* 1983] and (b) radiation enhanced diffusion by substitutional vacancy mechanism [Foreman *et al.* 1986]. The basic assumption in these models was that helium-point defect interactions are homogeneous in time and space. As a result, the discontinuous defect production nature due to the generation of collision cascades was not treated. Recent studies showed that the presence of these cascades would affect helium diffusion and bubble nucleation only if helium diffuses rapidly between defect clusters as, for example, by the replacement mechanism [Trinkaus *et al.* 1990 a and b]. However, for such fast helium diffusion, cascade effects would result in a strong temperature dependence of the helium bubble density.

Since no experimental data has showed such a dependence, it has been concluded that the homogeneity assumption made in the helium migration models is valid.

2.3.1. Interstitial (Dissociative) diffusion mechanism

Helium diffusion by a dissociative mechanism involves both dissociation of the trapped helium atom from a vacancy into an interstitial position and subsequent interstitial diffusion. The effective diffusion energy of helium to overcome this barrier is (see fig. 2.1)

$$E_{DIS} = E_V^B + E_I^M - E_V^F , \qquad (2.2)$$

where E_V^F is the vacancy formation energy. Chemical reaction rate theory has been used to write a set of differential equations that describe the time-dependent concentrations of various helium-point defect clusters [Ghoniem *et al.* 1983]. These include unoccupied vacancies, self-interstitial atoms, interstitial helium, divacancies and complexes containing M vacancies and N helium atoms. Both analytical and numerical solutions for these equations have shown that the effective helium diffusion coefficient during irradiation is dictated by three different physical processes: (a) the primary knocked out interstitial atoms can supply enough energy to detrap a helium from a vacancy or vacancy cluster at relatively low temperatures; (b) the competition between SIAs and helium atoms to react with vacancies may lead to a replacement detrapping at intermediate temperatures and (c) thermal detrapping of helium atoms at high temperatures by agglomerating to thermal rather than radiation-produced vacancies.

The contribution of the interstitial mechanism to the helium diffusion coefficient is given by the interstitial helium diffusion coefficient, D_{He}, times the fraction of interstitial helium [Schilling 1982]

$$D_{He}^{eff} = D_{He} \frac{c_{He}}{c_{HV} + c_{He}}, \qquad (2.3)$$

where c_{He} and c_{HV} are the relative atomic concentrations of interstitial and substitutional helium, respectively. If the helium concentration in interstitial sites is small, the total helium concentration may then be approximated by the concentration of helium in substitutional sites. Under the conditions of kinetic equilibrium, this yields

$$\frac{c_{He}}{c_{HV} + c_{He}} \approx \frac{c_{He}}{c_{HV}} \approx \frac{D_{He} \exp(-E_V^B / kT) + D_I c_I}{D_{He} c_V}, \qquad (2.4)$$

where c_I and c_V are the relative atomic concentrations of SIAs and vacancies, respectively and D_I is the diffusion coefficient of self-interstitial atoms.

2.3.2. Substitutional (Vacancy) diffusion mechanism

In the vacancy migration model, the helium atom jumps from its substitutional lattice site into a neighbouring vacancy in a manner similar to most impurity diffusion in metals [Foreman *et al.* 1986]. The activation energy needed

for this jump is most probably lower than that to reach an interstitial position and is of the same order as the self diffusion of the host metal. Depending on whether the activation energy of self diffusion is that of a mono- or di-vacancy mechanism [Peterson 1978], it can be estimated that the diffusion energy for the vacancy mechanism, E_{VAC}, is bracketed by the following values [Sciani *et al.* 1983]

$$Q_{2V} - E_V^F < E_V^D < Q_V , \tag{2.5}$$

where Q_V and Q_{2V} are the self diffusion energies by one- and two vacancy mechanisms, respectively.

The possibility that helium might diffuse by a substitutional mechanism during irradiation has been studied in two thermal ranges. At high temperatures, the diffusion process was found to be purely thermal in agreement with desorption experiments, while below half the melting temperature, T_m, diffusion is enhanced by the irradiation produced vacancies. In the latter case, the effective diffusion coefficient is expressed as

$$D_{He}^{eff} = Z C_V D_V , \tag{2.6}$$

where Z is a combinatorial factor and D_V is the vacancy diffusion coefficient. The factor Z reflects, but is not equal to, the number of sites from which the second vacancy would spontaneously combine with the substitutional helium.

This is expected to occur from second nearest neighbour sites, due to the pressure exerted by the helium atom on the intervening metal atom.

2.4. Experimental observations of helium diffusion in metals

Measurements of the effect of helium entrapment in metals on both the host lattice properties and the helium migration behaviour are of great importance for the nuclear technology. Reviewing all the available literature on the experimental detection of these effects is well beyond the scope of this thesis. However in the following sub-sections as well as throughout the discussion in Part II, a concise summary of these observations directly related to the present work is given.

2.4.1. Low temperature helium migration

Because of the strong interaction of helium with vacancies, its high mobility and its strong tendency to form clusters, interstitial diffusion can only be studied when the helium-introduction procedure meets the following requirements: (a) low temperature to avoid helium migration, (b) energies below the threshold for atomic displacement to avoid defect production and (c) low helium concentrations to avoid clustering when the atoms become mobile. This means that helium should be introduced only by either sub-threshold implantation or by the use of tritium decay. In the first approach, the helium implantation energy is chosen so that the maximum kinetic energy transfer to a metal atom is

less than the lattice displacement energy which typically lies in the range of 20 to 40 eV. Since the energy transfer to metal atoms is related to their masses, the maximum injected helium energy will vary from about 50 eV for a light metal like aluminum to about 400 eV for heavy metals, such as tungsten. It is obvious that the range of these low energy ions will be very short, limiting the use of this technique to thin film type of measurements.

Thermal desorption studies of interstitial helium migration in nickel were carried out following sub-threshold implantations at 77 K [Philipps *et al.* 1982]. The results obtained showed that helium could be retained in the crystal only if the sample was pre-doped with vacancies. This means that interstitial helium is already mobile at that temperature with $E_I^M \leq 0.3$ eV. Using lower implantation temperatures (18 K), a release peak was observed at around 50 K [Poker 1983]. If this peak is attributed to the onset of helium diffusion, a value of 0.14 eV for the migration energy can be estimated. However, the implantation energy at that study (35 keV) was high enough to create Frenkel pairs. The observed peak could then be attributed to the dissociation of helium from vacancies by self-interstitial recombination mechanism since in nickel self-interstitial atoms are mobile around 50 K. This indicates that the helium must be mobile at even lower temperatures and so the quoted 0.14 eV value may serve as an upper limit of E_I^M. Similar experiments were carried out for γ-iron [Philipps *et al.* 1983] and gold at 80 and 300 K [Thomas *et al.* 1981]. Estimated values of E_I^M were found to be ≈ 0.1 eV in the case of γ-iron and to vary within the range of 0.3 to 0.7 eV for gold.

Natural tritium decay to ^{3}He (half life = 12.3 years) is a complementary method to the low energy implantations in that it can be used to study bulk phenomena in the absence of damage. The low-energy β particle emitted in the tritium decay process is of insufficient energy (18 keV maximum) to displace metal atoms. Furthermore, the average recoil energy of the ^{3}He decay product is only ~ 1 eV, which is much less than that required to create damage sites during implantation. The major limitation of this method is that a clear interpretation of the observed helium behaviour depends on an accurate knowledge of the tritium distribution throughout the ageing period. For example, trapping or segregation of tritium at dislocations, grain boundaries or impurities will result in an enhanced generation rate of ^{3}He in these regions compared to the average bulk material.

Helium release measurements have been performed in three metals (nickel, aluminum and 304-type stainless steel) after tritium charging of 125 μm-thick samples and ageing at 80 K to various helium concentrations [Thomas 1983]. The following general observations can be made from the results displayed in fig. 2.3: (a) helium is mobile in all three metals above ≈ 100 K, indicating helium migration energies of the order of 0.35 eV; (b) in all cases, most of the helium is deeply and efficiently trapped and (c) the helium release fraction depends strongly on the initial helium concentration. Since the nickel and aluminum samples were of high purity and well-annealed materials and the stainless steel with low helium concentration was solution-treated and annealed, it appeared that pre-existing defects were not primarily responsible for the observed trapping. Observation of similar strong trapping in single crystal nickel samples indicates

that grain boundaries are not the major trapping sites either [Thomas *et al.* 1979]. The fact that the helium release fraction decreases with increasing ^3He concentrations suggests that helium-helium interactions are important in this process.

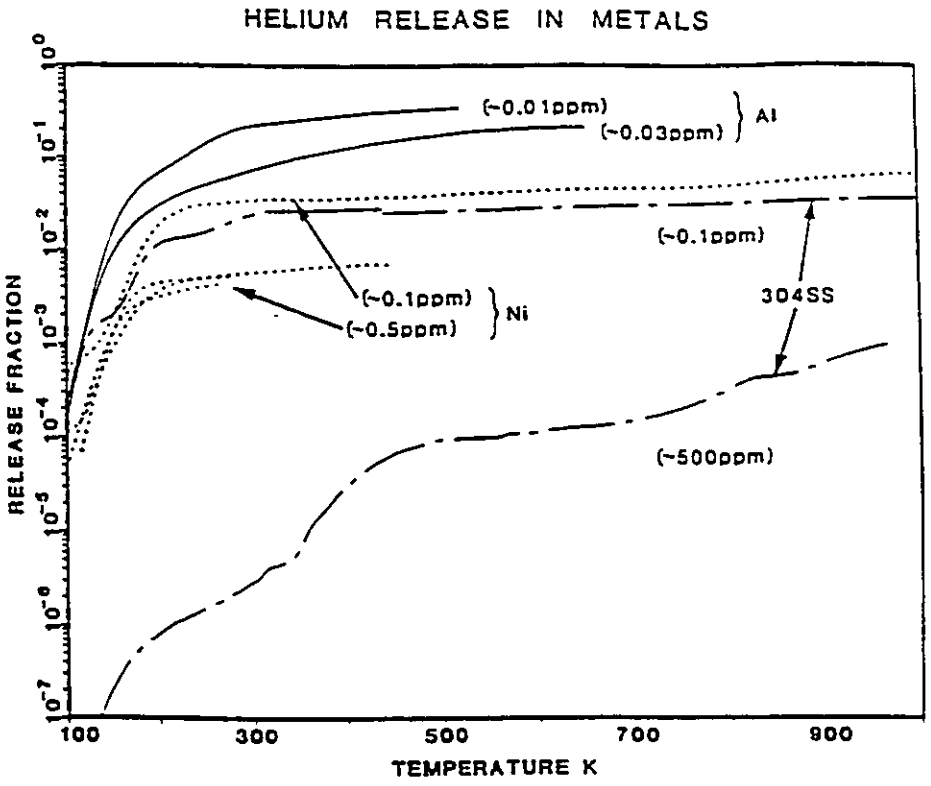

Fig. 2.3. Helium release fraction as a function of temperature during linear ramp annealing for three different tritium-charged metals. The initial helium concentration in each sample is given for each curve. All samples but the high concentration stainless steel have aged at 80 K. The ~500 ppm 304SS sample has aged near room temperature [Thomas 1983].

The spectra shown in fig. 2.3 were consistent with the self-trapping model of helium in metals [Baskes *et al.* 1983]. At a critical number of clustered

interstitial helium atoms, the stored energy becomes high enough for lattice relaxation by spontaneous formation of a Frenkel pair. The formed vacancy increases the binding energy of the interstitial cluster forming a bubble nucleus produced without radiation-induced lattice displacements. This mechanism as a form of "trap mutation" is discussed in detail in section 2.6.3.

2.4.2. Dependence on the implantation fluence

The experimental work on the trapping behaviour of helium after implantation into metals can be divided into two parts, depending on the implantation fluence used. At low fluences (generally below 10^{19} He/m^2) most of the investigations were done by thermal desorption spectroscopy (TDS). In these studies, thermal release measurements were applied to a simple detrapping process of a helium atom from a trap. Experimentally obtained activation energies for helium release were found to agree reasonably with the calculated values of the dissociation energy of simple HeVCs in metals [Caspers *et al.* (bcc) 1978, Jung *et al.* (fcc) 1988 and Vassen *et al.* (hcp) 1991]. Only at very low concentrations has it been possible to investigate atomic helium diffusion in metals as discussed in the previous section.

At higher fluences, overlapping of desorption peaks due to thermal release out of larger HeVCs or helium bubbles makes it very difficult to relate the observed peaks to specific release processes. Therefore, other methods such as scanning electron microscopy (SEM) [Manuaba *et al.* 1990], TEM [Niwase *et al.* 1988], electron energy loss spectroscopy (EELS) [Jäger *et al.* 1983] and optical

absorption spectroscopy (OAS) [Donnelly *et al.* 1983] have been applied. These methods have made it possible to observe such processes as the formation of helium gas bubble super-lattices in a variety of metals [Johnson *et al.* 1980] and to measure the density of helium in the formed bubbles [Manzke *et al.* 1982].

Only few thermal desorption studies have been performed following helium implantations of bulk materials up to fluences where surface structure modifications such as blisters occur. Such measurements indicate that helium desorbs from surface related traps which are created at the critical fluence for blistering [Ehrenberg *et al.* 1983]. The trapping and release behaviour of implanted helium proves not to depend on the implantation energy, *i.e.*, no dependence on the depth where helium is deposited. This confirms that diffusion does not determine the release process, rather it is controlled by dissociation from possible trapping sites.

2.4.3. Dissociation energies of helium-vacancy defects

The group that pioneered the work on the trapping of helium in metals is that of Kornelsen and co-workers from the National Research Council of Canada. In their studies, single crystals of tungsten [Kornelsen 1972] and nickel [Kornelsen *et al.* 1974] were bombarded initially with heavy rare-gas ions at energies of a few keV in order to create Frenkel defects as traps for the subsequently implanted helium. In addition, helium implantation was performed at sub-threshold energies to suppress additional defect creation during the implantation. The advantage of this approach is that the defect and helium

introduction are independently controlled. In fig. 2.4 the helium desorption spectra from tungsten are shown after helium injection to a fluence of 2.4×10^{17} He/m^2 at 250 eV for an undamaged crystal and for a crystal with a prior 5 keV damage bombardment with 2.4×10^{15} Kr/m^2. The lack of retention in the undamaged crystal is consistent with a high mobility of interstitial helium at room temperature and the release at high temperatures indicates strong trapping to defects. Both observations are consistent with the theoretical predictions of Wilson *et al.* (1972 and 1973). The observed release spectra have been interpreted in terms of helium trapping to mono-, di- and higher order vacancy clusters.

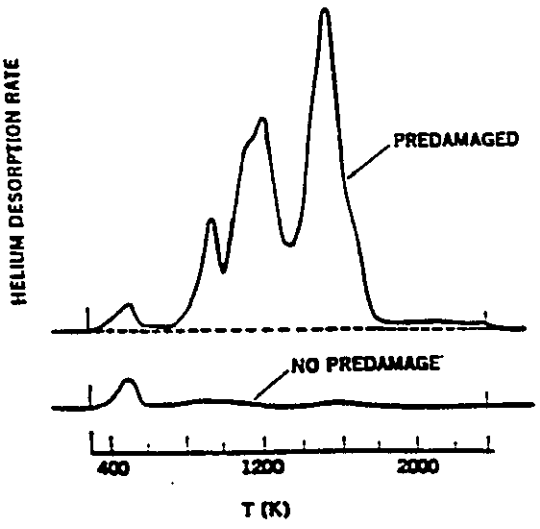

Fig. 2.4. Helium desorption rate as a function of temperature in tungsten after 2.4×10^{17} He/m^2 implant at 250 eV with and without damage produced by 2.4×10^{15} Kr/m^2 at 5 keV [Kornelsen 1972].

The same group also carried out a series of TDS measurements for the binding of helium to substitutional rare gas atoms and to detect the initial stage

of nucleation and cluster growth for the case of helium in tungsten [Kornelsen *et al.* 1980]. A summary of the obtained results is shown in fig. 2.5, where the temperature corresponding to the peak's maximum is plotted as a function of the number of helium atoms filling each trap for each of the gases.

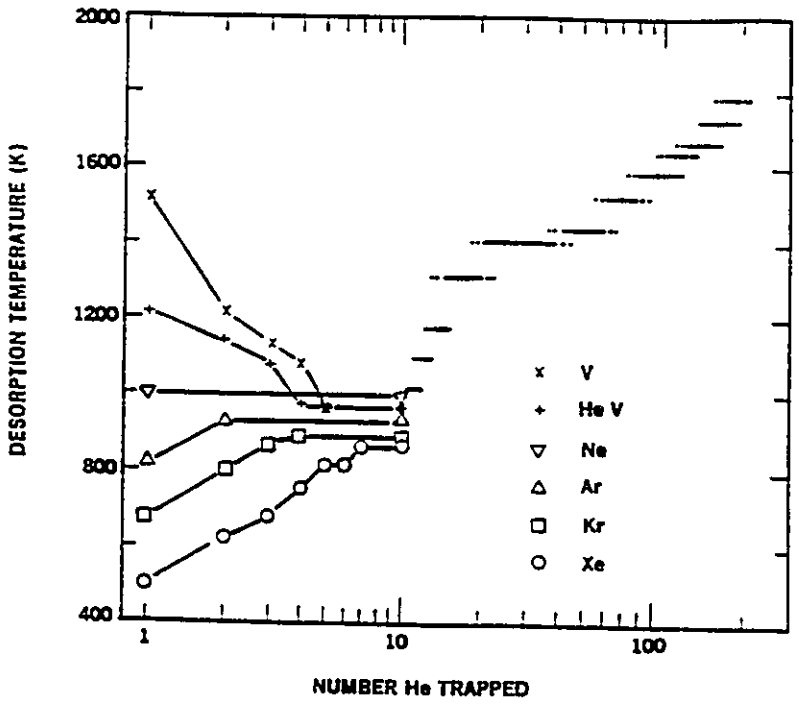

Fig. 2.5. Helium desorption peak temperatures as a function of the number of trapped atoms for the indicated inert gas or vacancy nucleating centres in tungsten [Kornelsen *et al.* 1980].

It can be seen that in the region of 1 to 10 helium atoms in a cluster, the binding energy of each additional helium for a vacancy nucleus drops with the number of trapped helium atoms; is relatively flat for a neon trap and increases for heavier inert gases. The first helium atom is deeply trapped to vacancies with

dissociation energy ≈ 3 eV. From the figure it can also be inferred that for more than 10 helium atoms per trap, no difference can be distinguished for different trap nuclei. Increasing the number of helium atoms per trap after that results in binding energies (indicated by line and dots in fig. 2.5) that increase monotonically with the number of helium atoms up to ≈ 100 trapped atoms. These results clearly demonstrate how energetically favourable it is for bubble nucleation and growth to result from simple helium-vacancy trap centres in implanted metals.

A second group that has independently tackled the study of helium behaviour in metals both experimentally and by numerical modelling is that of Delft University in The Netherlands. They have computed the formation energies of various helium-vacancy configurations in molybdenum [Fastenau *et al.* 1976] and tungsten [van Veen *et al.* 1977]. In a series of TDS measurements on molybdenum, the dissociation energies of helium as one from a tri-mer, one from a di-mer or present singly in a vacancy have been obtained [Caspers *et al.* 1976]. Their experimental procedure was similar to that employed by the Canadian group for the helium-tungsten system [Kornelsen 1972]. A summary of both the experimental observations and the calculated activation energies of the reactions proposed by both groups is given in Table 2.3.

In addition, measurements were made for the trapping of helium in a simple vacancy as a function of the temperature to which the pre-damaging krypton irradiation was annealed before the helium implantation [van Veen *et al.* 1975]. It was observed that a reduction in the quantity of gas released from

Table 2.3
Comparison of experimental and theoretical helium-vacancy dissociation energies for tungsten and molybdenum

Reaction	Experiment [a]		Theory	
	Peak temperature (K)	Dissociation energy (eV)	Wilson *et al.*[b] (eV)	Caspers *et al.*[c] (eV)
W: $He\,V \rightarrow He + V$	1560	4.05	4.39	5.07
$He_2V \rightarrow He + HeV$	1220	3.14	2.89	3.43
$He_3V \rightarrow He + He_2V$	1120	2.88	2.52	3.02
$He_4V \rightarrow He + He_3V$	950	2.41	2.50	2.94
Mo: $HeV \rightarrow He + V$	1180	3.05	4.19	4.20
$He_2V \rightarrow He + HeV$	960	2.50	-	2.82
$He_3V \rightarrow He + He_2V$	900	2.30	-	2.50
$He_{4,5,6,}V \rightarrow He + He_{3,4,5,}V$	800	2.05	-	2.37

[a] W results from Kornelsen (1972) and Mo results from Caspers *et al.* (1976).
[b] Wilson *et al.* (1972 and 1974).
[c] Caspers *et al.* (1976).

vacancies containing one helium occurred following pre-loading annealing to progressively higher temperatures. This reduction after annealing in the temperature range 400 to 500 K, analogous to Stage III recovery in molybdenum, was attributed to the gradual reduction in the quantity of vacancies left after the initial damaging irradiation.

2.4.4. Helium migration by interstitial and substitutional mechanisms

The rate of diffusion of helium atoms depends on the positions occupied

by these atoms. The diffusion coefficient of interstitial helium is significantly larger than that of substitutional helium atoms, *i.e.*, $D_{DIS} \gg D_{VAC}$. However, interstitial helium atoms are easily captured by vacancies, small HeVCs being formed as a result. Several experiments on helium desorption from irradiated materials indicate that the majority of such clusters contain one vacancy and one helium atom and thus are simply substitutional helium atoms [Lewis *et al.* 1986]. Helium diffusion by the vacancy mechanism is activated by the presence of a second vacancy in the vicinity of the trapped helium so that the following reaction takes place

$$(HeV) + V' \leftrightarrows (HeV') + V . \tag{2.7}$$

Some metals, however, show an unusually low activation energy which suggests the dissociative mechanism, where helium atoms pass from a substitutional position to an interstitial one according to the reaction

$$(HeV) + I \leftrightarrows He . \tag{2.8}$$

Experimental investigations of both mechanisms are done by measuring the helium release from foils of various thicknesses in isothermal as well as linear-heating desorption regimes. Helium ions are normally introduced homogeneously throughout the foil thickness by variable energy α-bombardment and examination of the dependence of the release spectra on time, thickness and concentration makes it possible to separate free diffusion from trapping or

agglomeration processes.

At constant temperature, the fraction of released helium $(c_o\text{-}c)/c_o$ at time t in a diffusion controlled desorption is described by the diffusion theory as [Crank 1979]

$$\frac{c_o - c}{c_o} = \left(\frac{16 D_{He}\, t}{\pi d^2}\right)^{1/2} \quad for \quad \frac{c_o - c}{c_o} \leq 0.5 \ , \qquad (2.9)$$

where c_o and d are the initial helium concentration and the specimen thickness, respectively. Equation (2.9) shows that free diffusion can only be assumed if the released fraction is independent of c_o and is proportional to $t^{1/2}$ and d^{-1} for $c \geq 0.5\, c_o$. The activation energy of the diffusion coefficient D_{He} can be used to identify the diffusion mechanism. Figure 2.6 shows the fraction of helium released isothermally from 13 μm silver foils as a function of time. The initial atomic concentration was about 1.4×10^{-8} in all specimens [Jung 1991]. Deviation from free diffusion at longer time periods was related to the fact that helium has become immobilized by trapping and/or clustering.

Diffusion constants of helium derived from measurements similar to that depicted in fig. 2.6 are given in fig. 2.7 for copper, gold and silver. In gold the activation energy as well as the absolute values of the diffusion constant are in close agreement with self-diffusion data. In silver, helium diffusion is significantly faster than self diffusion and has a somewhat smaller activation energy (1.5 versus 1.76 eV). For copper, the discrepancy is huge and the

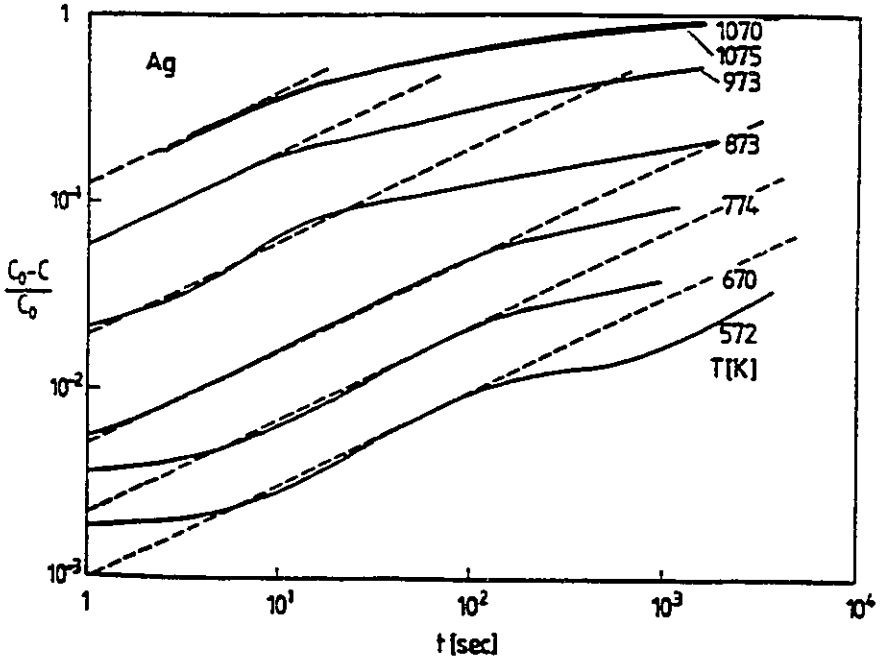

Fig. 2.6. Fraction of helium released by free diffusion from 13 μm silver foils during isothermal desorption experiments [Jung 1991].

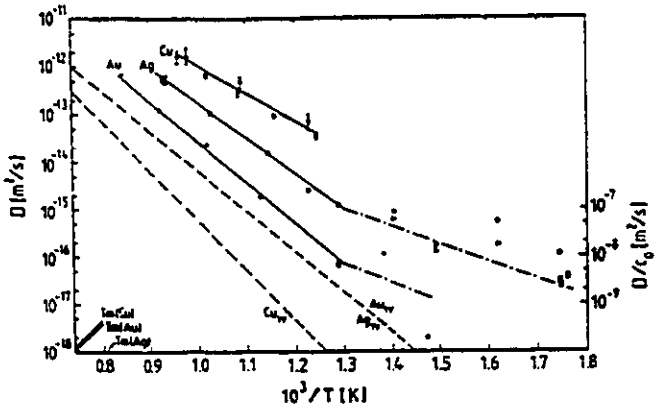

Fig. 2.7. Diffusion coefficients of helium in copper, silver and gold. The dashed lines give self diffusion by the mono-vacancy process. The scatter of the low temperature ($10^3/T > 1.3$) gold and silver data is reduced by dividing by the atomic fraction (new ordinate is on the right hand side) [Jung 1991].

activation energy is even below the lower limit $Q_{2V} - E_V^F$ conceivable for diffusion by a vacancy mechanism. Such observations indicate that the vacancy mechanism controls the helium diffusion in gold and probably also in silver, while in copper helium diffuses by the dissociative mechanism. Comparison of the diffusion coefficient pre-factors for the host lattice and helium, as obtained from the y-axis intercepts in fig. 2.7, confirms these conclusions. For gold and silver, the measured values are about 10^{-5} m^2/s, in close agreement with self diffusion values. On the other hand, for copper a value of only about 10^{-6} m^2/s is derived. This is less than the self diffusion coefficient by almost one order of magnitude and was ascribed to the shorter diffusion steps in the dissociative mechanism.

Part II. Nucleation and Growth of Helium Bubbles in Metals

2.5. Stages of helium-vacancy clustering

The insolubility of helium in metals results in the aggregation of the implanted helium at irradiation-produced vacancies, forming small clusters. These microbubbles grow by accumulating further gas atoms and vacancies, preferentially nucleating at inhomogeneities like dislocations and grain boundaries. Of special importance to fusion technology is the role which helium plays in the nucleation of voids in the plasma-facing materials since this directly results in such phenomena as high temperature embrittlement and enhanced swelling. Therefore, considerable research has been devoted to establishing the basic mechanisms controlling the nucleation and growth of helium bubbles in the candidate first wall materials.

Helium bubbles may be divided into three characteristic size classes as summarized in Table 2.4. The lower size classes with radii less than 10 Å comprise the simple $He_N V_M$ clusters. As discussed in Part I, helium-metal interactions affect all the helium atoms within such clusters and the energetics of formation are readily derived by atomistic modeliing. As the values of N and M increase, the fraction of helium atoms and vacancies at the cluster surface decreases as $N^{-1/3}$ and $M^{-1/3}$ and the helium-metal interaction for helium

atoms in the cluster interior becomes negligible. With further increase in the number of helium atoms and vacancies, statistical mechanics methods are used to describe the energy of the HeVCs [Trinkaus 1982]. Nucleation of helium bubbles, *i.e.*, the formation of stable HeVCs independent of helium-metal interactions, occurs in the first two size ranges. Above 10 Å helium bubbles are very stable up to temperatures close to the melting point of the metal. Once helium bubbles have been nucleated they can grow under helium supply and stress- or irradiation-induced vacancy supersaturation [Brailsford *et al.* 1973]. But even in the absence of both, they can grow by a number of mechanisms, the most common of which is migration and coalescence. These mechanisms will be discussed in the following section.

Table 2.4
Classification of helium bubbles in metals

Size range	≤ 1 Å	few Å	1 - 10 nm	10 - 100 nm	0.1 - 1 μm
Helium content	few appm	< 0.1 at%	0.1 - 10 at%	10 - 30 at%	> 30 at%
Type of cluster	<----- Bubble -----> |	<-- Non-ideal gas bubbles --> |		<- Ideal -->	
	nuclei				gas bubbles
Energetics	<-- Helium-metal interaction for all He atoms -> |	<---- Helium-metal interaction restricted to bubble surface --->			
Kinetics	<---- Nucleation ---> |	<---------- Growth ---------->			
Theory	<---- Computer simulation ----> |	<---------- Statistical mechanics ---------->			

2.6. Formation kinetics of helium bubbles

The precipitation kinetics of helium in metals are determined by the helium deposition rate and temperature as well as by the displacement rate. Three characteristic regions can be distinguished [Trinkaus 1983]. For high helium deposition rates and/or low temperatures ($\leq T_m/3$), diffusion-controlled clustering of thermal- or irradiation-induced vacancies is too slow to contribute to the formation of helium bubbles. In these cases, helium precipitation occurs spontaneously and in a homogeneous fashion by athermal processes such as spontaneous formation of Frenkel pairs. For low helium deposition rates and high temperatures ($\geq 0.5\ T_m$), a defect cluster or helium bubble can absorb a sufficient number of thermally activated vacancies to keep the internal pressure close to its equilibrium value. In this case helium precipitation can be either heterogeneous or homogeneous depending on the production rate of helium, temperature and microstructure of the metal. For low helium deposition rates at intermediate temperatures, helium can assist void formation and precipitates into existing voids, but does not contribute significantly to the growth of such clusters.

Small helium bubbles can in principle grow by one or more of a number of mechanisms. Under appropriate conditions of gas pressure, temperature, defect concentration and bubble density, bubbles may attract mobile vacancies; they may emit SIAs; they may eject plates of atoms as interstitial dislocation loops; they may ripen by re-solution of the gas in small bubbles and re-precipitation into larger cavities nearby (Ostwald ripening); or they may migrate through the metal until they collide and coalesce.

2.6.1. Gas pressure-driven models

The first gas pressure-driven model was the dislocation loop punching mechanism, proposed as a possible means of stress relief in overpressurized bubbles [Seitz 1950]. Excess bubble pressure deforms the surrounding atom planes by punching out a platelet of interstitial atoms along a glide plane thus producing an interstitial dislocation loop. A schematic diagram of this mechanism is given in fig. 2.8.

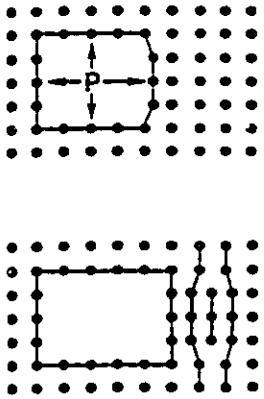

Fig. 2.8. Bubble growth by dislocation loop punching mechanism. (a) Excess bubble pressure deforms surrounding atom planes; (b) Punching allows expansion of bubble and creation of an interstitial loop [Evans 1978].

By considering the energetics involved in these processes, the minimum pressure required for loop punching, P_{lp}, is given by [Greenwood *et al.* 1959]

$$P_{lp} = \frac{2\gamma}{R} + \frac{\mu\, b \ln(R/b)}{2\pi R} \quad , \tag{2.10}$$

where R and γ are the bubble radius and surface energy, respectively, μ is

the shear modulus of the host material and b is the Burgers vector of the resulting dislocation loop. The importance of this mechanism has been noted for the helium case and direct TEM observations support its operation in different materials [Evans *et al.* 1981].

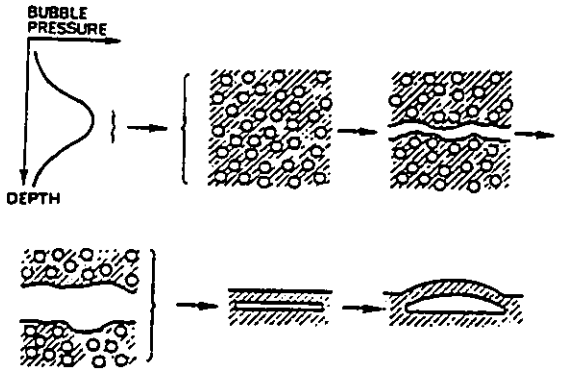

Fig. 2.9. Schematic diagram of interbubble fracture mechanism for helium bubble formation [Evans 1977].

Another gas pressure-driven mechanism that was suggested to explain the formation of blisters on helium irradiated surfaces is the interbubble fracture model [Evans 1977 and 1978]. A schematic outline of this mechanism is given in fig. 2.9. During helium implantation of metals, the resulting vacancies and gas atoms combine with one another to form cavities in the matrix. As the fluence increases, the density of the cavities increases, the overpressurized bubbles grow, their spacings decrease and the added internal pressure of several adjacent bubbles eventually creates a local stress sufficient to crack open the plane joining the bubbles. Due to coalescence, bubbles adjacent to the original crack

act to widen it and increase the pressure. As a result the ultimate tensile strength of the material is exceeded and the skin of the cavity is plastically deformed and pushed upwards causing the formation of a blister.

The pressure at which this process occurs depends on the bubble concentration, C_B, as well as the fracture stress of the material, σ_f. For co-planar bubbles the required fracture pressure, P_f is given by

$$P_f = \frac{2\gamma}{R} + \sigma_f [(\pi R^2 C_B^{2/3})^{-1} - 1] \quad . \qquad (2.11)$$

It is interesting to note that when eqs. (2.10) and (2.11) are compared, it can be shown that small bubbles will always relieve their excess pressure by loop punching, *i.e.*, $P_{lp} < P_f$ for small values of R. At larger bubble sizes the two equations converge significantly until a critical value of bubble radius and pressure where the interbubble fracture process takes over. Extensive bubble coalescence and internal helium release may then occur and lead naturally to the formation of surface blisters [Donnelly 1985].

It is expected in the gas pressure-driven models that the depth at which the skin separates from the bulk, *i.e.*, the blister skin thickness, d_s, should correspond to the peak in the projected range probability distribution, r_p. This had been observed for a number of metals implanted with helium ions at energies higher than 60 keV [Das *et al.* 1980]. However, subsequent measurements at energies below 20 keV have shown d_s to be no longer in agreement with the

expected values of r_p. These observations have led several groups to propose a lateral stress model that does not require the blister skin to separate at r_p.

2.6.2. Lateral stress-driven model

In the lateral stress model, it is suggested that the large lateral stresses introduced in the implanted surface layer lead to elastic instability and buckling of the implanted surface layer above the weakened interface region, and thus the gas pressure would not be a driving force behind the cavity formation [EerNisse *et al.* 1977]. Figure 2.10 illustrates a pictorial representation of the mechanism.

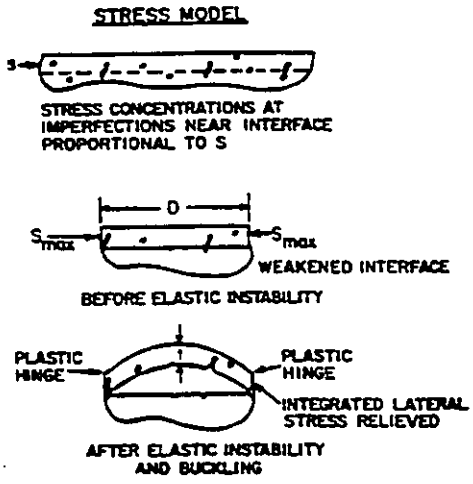

Fig. 2.10. Schematic diagram of lateral stress model of helium bubbles in metals [Das 1980].

Helium induced lattice imperfections result in the formation of an unstable interface region. Shear stresses that concentrate in the vicinity of defects are proportional to S, the integrated lateral stress (*i.e.*, force per unit width) acting between the implanted layer and the substrate. Just below the point of elastic

instability, the stress reaches a maximum value acting on an equivalent elastic plate with diameter D of the weakened interface and at the elastic instability point the plate buckles forming a plastic hinge around its perimeter.

The stress model assumes that the shear stresses that initiate blister skin separation are proportional to the gradient of the volume swelling, and hence the projected range profile, so that separation occurs at depths where the integrated lateral stress exceeds its critical value. As a first approximation, the skin thickness is assumed to be equal to $r_p + \Delta r_p$, where Δr_p is the straggling in the projected range distribution. For high incident energies, Δr_p is small compared to r_p and thus d_s is nearly equal to r_p. However, at low energies, Δr_p is comparable in magnitude to r_p, and therefore d_s is predicted to be considerably larger than r_p.

There are several conflicts between the gas pressure models and the lateral stress model such as the absence of blister formation in the ion beam studies involving void-swelling, where the stress systems should be similar and the suggested relationship between the blister diameter and the skin thickness is $D \propto d_s^{1.5}$. In order to make such a correlation meaningful, a thorough study has considered the effects of such parameters as the target temperature, total fluence and target microstructure on the blister diameter [Das *et al.* 1979]. The exponent of proportion between D and d_s was found to depend on the investigated material (*e.g.*, $D \propto d_s^{1.25}$ for Be and $d_s^{0.85}$ for V at room temperature implantation), in direct contrast to the prediction of the stress model of a constant exponent of 1.5 independent of both the material and the irradiation temperature.

Other experimental investigations have clearly showed that the discrepancy between d_s as measured by SEM and the calculated values of r_p for energies below 20 keV is due to the large swelling of the blister skin, thus favouring the gas pressure driven models as the operative mechanism to explain the formation of surface blisters on helium implanted metals [Das *et al.* 1978].

2.6.3. Trap mutation models

Trap mutation is a notable effect that has been discovered in the transition region of helium bubble nucleation. At early phases, the growth of the bubble nuclei proceeds by helium atoms filling a vacancy. However with each helium atom added the local Frenkel pair formation energy is lowered, such that after a certain number of clustered helium interstitials (about 5 to 10), the stored energy becomes high enough to allow relaxation of the cluster by spontaneous formation of a Frenkel pair. By such, the created vacancy helped to further stabilize the defect cluster in what is known as the self-trapping mechanism [Wilson *et al.* 1981]. If thermal- or irradiation-induced vacancies are present in the metal, helium will fill them up and stabilize them against recombination at about six helium atoms per vacancy. After some transient time a similar stage will be reached as after the spontaneous formation of Frenkel pairs. If additional helium is supplied, further metal SIAs will be ejected, staying close to the HeVC and increasing its volume. Such a process would be expected to provide a strong driving force for the growth of helium gas bubbles.

For an SIA to be created, the work done by the helium pressure in

increasing the size of the cluster by one metal atomic volume has to be at least equal to the self interstitial formation energy, E_i^F. Thus, the minimum pressure for SIA emission is given by [Galsgow *et al.* 1984]

$$P_{SIA} \approx \frac{2\gamma}{R} + \frac{E_i^F}{\Omega} \quad , \tag{2.12}$$

where Ω is the atomic volume of the host lattice. This threshold pressure can reach values higher than 100 GPa (15.4 GPa for Be).

Experimental evidence for this trap mutation process has been found for helium implanted into molybdenum [Caspers *et al.* 1978]. The mechanism has been confirmed by interpreting the thermal desorption spectra in conjunction with cluster calculations. The following trap mutation reaction was proposed

$$He + He_N V \rightarrow He_{N+1} V_2 + I \quad or \quad He_N V \rightarrow He_N V_2 + I \tag{2.13a}$$

as the first of a series of reactions

$$He + He_N V_M \rightarrow He_{N+1} V_{M+1} + I$$

or

$$He_N V_M \rightarrow He_N V_{M+1} + I \ , \quad M \geq 2 \ . \qquad (2.13b)$$

Thus not only helium atoms, but also vacancies are added to the defect center, increasing its stability and providing for its eventual growth into a gas bubble. A similar effect has also been inferred for tungsten at $N \simeq 6$ helium atoms [van Veen *et al.* 1977]. Computer simulations in bcc metals have linked the nucleation of helium bubbles to the mutation of simple He-V trapping sites in a fashion similar to the reactions (2.13) [Caspers *et al.* 1981].

Another form of trap mutation is the interconnection or percolation of simple He-V defect configurations. It has been discovered in an extension to the atomistic calculations of helium trapping in metals and has been explored as a means of bubble growth in the low temperature regimes [Baskes *et al.* 1978]. The models predicted that $He_6 V$ defects could connect at up to the fourth nearest neighbour distance in cubic lattices. A statistical treatment by Monte Carlo methods allowed defects within a certain distance of one another to rearrange spontaneously to the lowest energy configuration. The new defect thus found was then itself allowed to recombine with any defects lying within its critical radius. In this way, at a critical concentration of defects, growth of the largest bubble was observed to occur and was successfully identified with the critical fluence for blister formation for niobium, molybdenum and vanadium.

Another Monte Carlo procedure has been used to model the nucleation and growth of helium bubbles [Baskes *et al.* 1981]. In this case the results showed that if helium can create lattice vacancies and if the resulting SIAs

remain attached to the cluster, helium bubbles readily grow. By including SIA trapping at helium filled vacancies, percolation followed by interbubble rupture could also explain blistering at about the experimentally observed helium content in a number of metals. It is worth noting here that the loop punching mechanism is considered as a logical extension of the trap mutation by SIA creation. Emission of metal interstitial clusters by overpressurized bubbles is energetically more favourable than the emission of single interstitials since in the former the binding energy of the interstitials to the cluster is saved.

2.6.4. Migration and coalescence

The possibility of inert gas bubble migration has been predicted in theoretical studies [Greenwood *et al.* 1963] and direct TEM observations showed that small helium bubbles could migrate up a temperature gradient at significant rates at temperatures slightly above half the melting point [Barnes *et al.* 1963]. It was later reported that random Brownian motion of helium bubbles occurs in the absence of any long range driving force (*i.e.*, no temperature or pressure gradients) and can account for isothermal bubble growth at temperatures as low as 0.4 T_m [Tyler *et al.* 1980]. Such motion would lead to bubble collision and, since there is effectively no short range repulsion between two bubbles, to coalescence.

The most important characteristic of the migration and coalescence (MC) process is the rate controlling mechanism for bubble migration. Bubble motion through a solid essentially requires the transfer of atoms from the leading surface

to the trailing surface. Three routes are available to the atoms: they can diffuse via the vapour phase within the bubble; they can diffuse around the surface of the bubbles; or they can diffuse via the vacancy diffusion mechanism in the opposite direction, through the crystal lattice bulk near the bubble. These routes are summarized schematically in fig. 2.11 (a). Each mechanism leads to a different growth rate and should therefore be distinguishable from isothermal bubble growth experiments.

The main assumptions, which are almost universally made in the derivation of theoretical expressions to fit the results obtained from those experiments, are that the gas in the bubbles obeys the ideal gas law, that the bubbles are spherical and that there is no barrier to the coalescence of two bubbles if they touch. Under these conditions, the mean bubble radius is related to the annealing time by the simple power law [Gruber 1967]

$$R \propto t^{1/n} \quad , \tag{2.14}$$

where n is a function of both the migration mechanism and the bubble pressure. The value of n was found to be 2 for Ostwald ripening, 3 for vapour transport across equilibrium bubbles, 4 for volume diffusion around equilibrium bubbles, 5 for vapour transport across or volume diffusion around bubbles at constant pressure or for surface diffusion around equilibrium bubbles and 6 for surface diffusion around bubbles at constant pressure [Kaletta 1983]. It certainly seemed likely from the early experimental results that surface diffusion dominates at temperatures up to at least 0.6 T_m [Cottrell 1967] and it has later been

established that this is indeed the case for several metals and, by implication, for most [Goodhew *et al.* 1981].

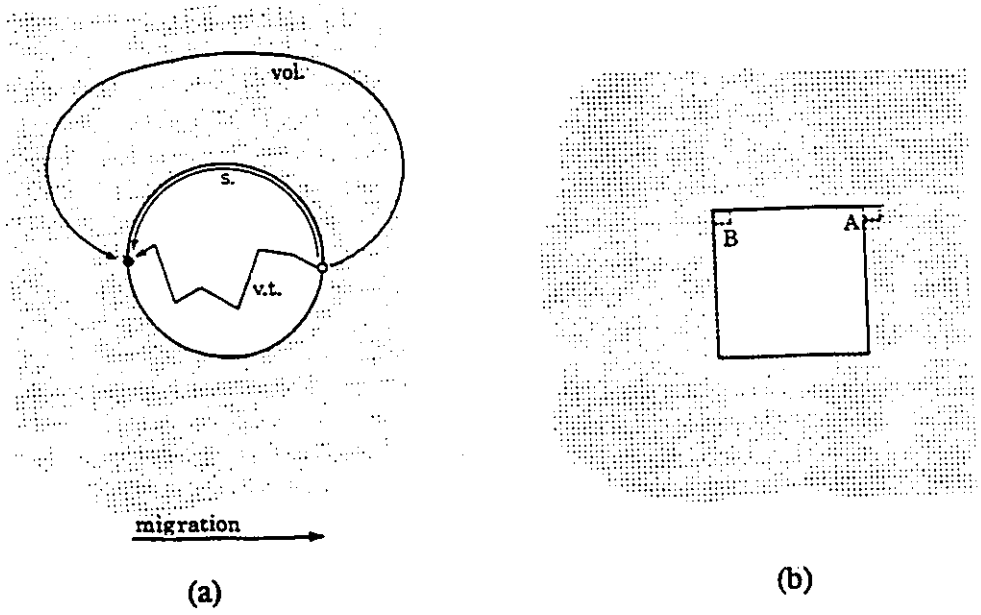

Fig. 2.11. (a) Possible mechanisms for bubble migration through a lattice: vapour transport (v.t.), surface diffusion (s.) and volume diffusion (vol.); (b) For a faceted bubble to migrate from left to right atoms must be moved from sites such as *A* and deposited at sites such as *B*. The rate controlling process is the nucleation of a step at *A* [Goodhew *et al.* 1981].

It was reasonable to assume that the rate of bubble migration is controlled by the magnitude of the dominant diffusion mechanism. However, this is not necessarily the case: there may be an interfacial reaction which inhibits growth and becomes rate controlling. Such a case was observed for large faceted bubbles when transport by surface diffusion is limited by the need to nucleate ledges on atomically flat facets. A simple depiction of this situation is shown in fig. 2.11 (b). This effect has proved to be efficient in restricting the growth of bubble

populations, since large faceted bubbles become essentially immobile. The effect still operates when bubbles are very small, but the problem becomes how to determine that the bubbles are faceted if they are too small to be detected by conventional electron microscopy. However, it appears that for most metals, the size at which ledge nucleation turns to be rate limiting is also the size at which it becomes relatively easy to see the facets by TEM [Tyler *et al.* 1980].

Another effect which acts to slow MC of helium bubbles is the presence of extremely high gas pressures. A bubble containing gas at pressures high enough to reduce the gas-phase atomic spacings to values similar to those in a solid will act as a solid precipitate. Instead of surface diffusion around the inside of the bubble, the process more closely resembles interfacial diffusion at a phase boundary and thus is much slower. For example, experimental evidence has been obtained showing that very small helium bubbles in nickel were prevented from migrating until sufficient vacancies arrived to reduce the gas pressure and thus increasing the atomic spacings [Marochov *et al.* 1987].

2.6.5. Other growth mechanisms

Other competing bubble growth mechanisms are the net collection of newly introduced gas atoms and vacancies by every bubble driven by its excess internal pressure [Barnes *et al.* 1958] and Ostwald ripening through the transfer of vacancies and helium atoms from smaller shrinking bubbles to larger ones [Nelson 1969]. The acquisition of vacancies from their abundant sources (the free surface on one side of the implantation region and the grain boundaries in

the bulk on the other side) was proposed, almost forty years ago, as another possible rate-limiting mechanism for the growth of helium bubbles in metals. Small overpressurized bubbles are an excellent net sink for vacancies until they reach their equilibrium pressure, $2\gamma/R$. Only then does the vacancy flux in and out of each bubble approach a steady state. Therefore, very few vacancies from the surface will get past the outer bubbles of the implanted layer until these bubbles reach their equilibrium size. Then the penetration of the vacancies to the bulk allows the interior bubbles to grow as well [Chernikov *et al.* 1990]. This vacancy-collection-limited behaviour, however, is not by itself a mechanism by which bubbles are likely to grow by large amounts. It will in principle be superimposed on any MC growth process functioning mainly by lowering the gas pressure and enabling the other growth mechanisms to operate.

Helium bubble ripening via helium re-solution and re-absorption is expected to become efficient only above $T_m/2$. In this high temperature range, thermal vacancy absorption is fast enough to keep the pressure within the bubbles at the equilibrium value. The growth characteristics of the bubbles in this range are of special interest since they give direct information on the permeation coefficient of helium. However, the vacancy collection and ripening mechanisms have been found to dominate only at very high temperatures, or at very small bubble sizes with high gas pressures. For the regimes of most practical interest, including normal operation of a thermonuclear fusion reactor, MC is the most significant mechanism in controlling the growth of helium bubbles.

CHAPTER 3

Thermal Desorption of Gases from Metal Surfaces

3.1. Introduction

The application of transmission electron microscope techniques to the study of void formation and bubble growth in implanted materials has provided considerable information on the gas defect interactions which occur during the later stages of the development of these features. However, an understanding of the fundamentals of the trapping processes requires a knowledge of the behaviour of gas atoms trapped in the lattice prior to the formation of complexes visible in the microscope and it is in this low fluence regime that gas release measurements have made the major contribution.

Thermal desorption spectroscopy (TDS) is the most widely used analytical method to study the interactions of ion implanted gases in solids. In principle, TDS is identical to the "flash filament" method used to study the kinetics of the desorption of chemisorbed atoms or molecules from solid surfaces [Ehrlich 1961]. An ion implantation-thermal desorption experiment consists of ionizing the gas of interest and implanting it at a known energy and to the required fluence. After

the implantation, the temperature of the sample, T, is varied with time from its original value, T_o , according to a controlled tempering schedule. This is typically either a linear increase with time ($T=T_o+\beta t$) or reciprocal decrease ($1/T=1/T_o+\beta t$), where β is the ramping rate. The resultant gas release rate is usually monitored using a calibrated mass spectrometer in an ultra-high vacuum system, or, by counting methods if radioactive ion species were employed [Baldwin *et al.* 1991].

During desorption and if there is no re-adsorption on the sample surface, the rate of desorption per unit area is calculated as

$$\frac{d\theta}{dt} = \left(\frac{V}{AkT}\right)\left[\frac{dP}{dt} + \left(\frac{s}{V}\right)P\right] \quad , \tag{3.1}$$

where θ is the surface coverage, P is the pressure increase above the background, V is the volume of the desorption chamber, s is the system pumping speed and A is the sample surface area. The assumption of no adsorption on the sample during the desorption cycle is valid for the desorption of ionically trapped inert gases in solids. The term "surface coverage" has been widely used in desorption analysis to describe the integrated area under the desorption rate curves. Although in the case of ion implantation experiments more physically accepted descriptions might be "peak population per unit area" or "integrated desorption rate", the traditional use of the term "surface coverage", or simply "coverage", will be retained through the discussion part in the present work.

The desorption peaks which comprise the spectrum are used to define the nature of the atomistic trapping and release processes within the solid. Assuming a release mechanism can be specified, the desorption spectrum may yield information on the number of different types of traps, the extent to which each type is occupied and the activation energies for release. The analysis is particularly straightforward when the gas release is due either to a single activated jump out of a trapping site, analogous to first order desorption of chemically adsorbed species, or to a process where gas atoms trapped at some depth below the surface thermally diffuse prior to release. In this Chapter, the most commonly applied procedures in interpreting thermal desorption spectra will be reviewed with the necessary conditions and limitations associated with each of them.

3.2. Thermal desorption analysis procedures

Thermal desorption is usually described in terms of the Polanyi-Wigner equation (PWE) that gives r, the desorption rate per unit area, as

$$r(\theta) = - \frac{d\theta}{dt} = \nu(\theta)\,\theta^n \exp(-Q(\theta)/kT) \quad , \qquad (3.2)$$

where ν is the attempt frequency and n and Q are the order and activation energy of desorption, respectively. In the case where lateral interactions exist between the adsorbate particles, both ν and Q may depend on coverage. The

desorption rate curve, fig. 3.1, has a maximum when $dr/dt=0$, which corresponds to

$$n\left(\frac{d\theta}{dT}\right)_{T_P} = \frac{\theta_P Q}{k T_P^2} \quad , \tag{3.3}$$

where T_P is the temperature at which the desorption rate is maximum, *i.e.*, $r=r_P$.

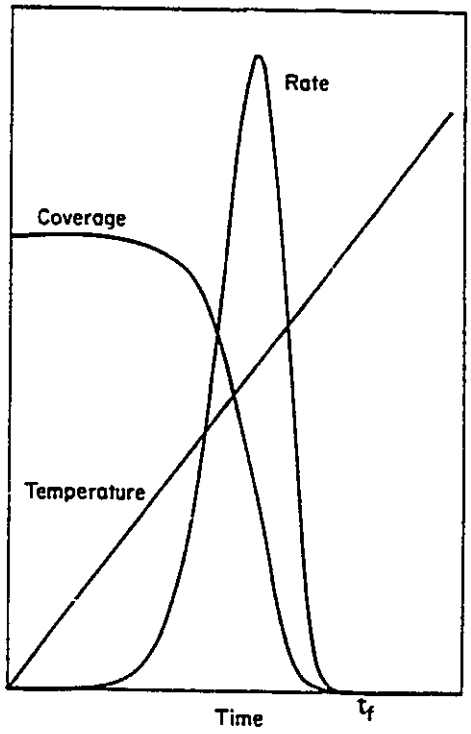

Fig. 3.1. Temperature, desorption rate and surface coverage dependence on time during a linear desorption regime. The surface coverage θ_t is the integrated area under the desorption rate curve from any time t to t_f.

A variety of methods are available for deducing values of these parameters from the experimental desorption spectra [Falconer *et al.* 1983]. Some of these procedures are based on the PWE without further assumptions. These "complete methods" usually require a collection of desorption curves from which the required parameters are directly derived. To avoid the complexity of the complete methods, many investigators use simplified, approximate methods, which make use of easily accessible features, such as T_P, peak widths and parameters which reflect the shape of the desorption spectra. These methods are attractive because they are rapid, relatively simple and can be applied to a single desorption curve.

3.2.1. Lineshape analysis

The lineshape procedure is based on the rigorous application of the PWE [King 1975]. A distinction is made between two cases of desorption spectra depending on their structure. For a single-peak desorption curve, if the pumping speed to volume ratio is large and the ramping rate β is low, the desorption rate, as defined in eq. (3.1), is conveniently proportional to the pressure increase P since $dP/dt \ll (s/V)P$. The surface coverage at time t is therefore given by

$$\theta_t = s/(AkT) \int_t^\infty P\,dt \quad . \tag{3.4}$$

From a family of desorption curves corresponding to different initial coverages higher than θ_t, eq. (3.2) is used to construct a family of curves of θ_t

as a function of t. For a given value of θ_t, several values of t, corresponding to a range of values of the sample temperature T, can be obtained as shown in fig. 3.2. The desorption rate for each combination of θ_t and T is known from the desorption curve and an Arrhenius plot of all $ln(r)$ versus $1/T$ can be constructed corresponding to the constant coverage θ_t. Since the attempt frequency is constant at constant θ, the slope of the Arrhenius plot yields $Q(\theta)$ at θ_t, independent of the value of either ν or n. Repeating this procedure for different values of θ_t, a plot of Q as a function of θ can be constructed. The intercepts on the Arrhenius plots yield $ln\ \nu(\theta_t)+n\ ln(\theta_t)$; thus if the plot of intercepts against $ln(\theta)$ is linear, ν is coverage-independent and is directly obtained from the second intercept and n is unambiguously given by the slope. However, if this plot is non-linear, integral values of n must be tried to determine $\nu(\theta)$, which leads to possible ambiguities.

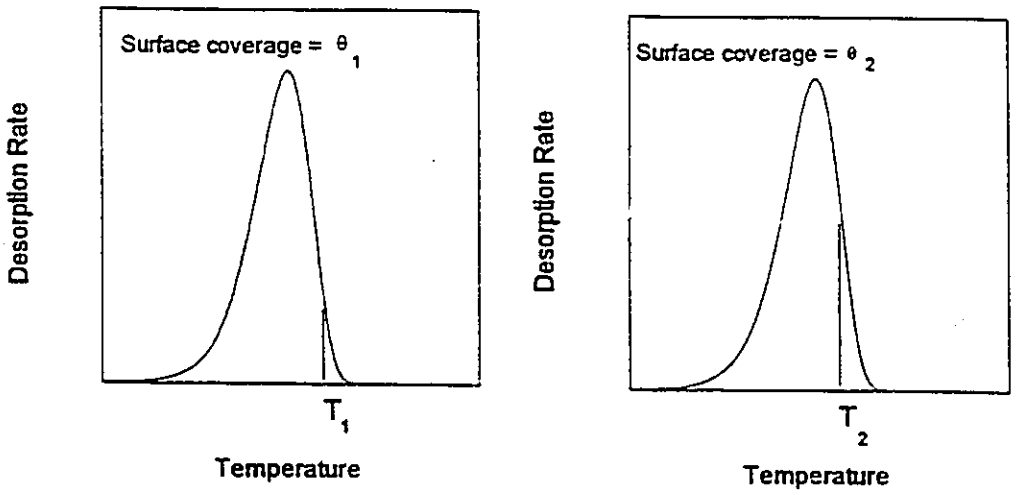

Fig. 3.2. Lineshape analysis of thermal desorption curves. Two desorption curves with surface coverages $\theta_1 > \theta_2 > \theta_t$ are used to estimate the temperatures T_1 and T_2 and the corresponding desorption rates at a constant surface coverage θ_t.

For multiple-peak desorption spectra, the simplest and most common method employed is to de-convolute the desorption curve into component monotonic units on the basis of the structural features of the spectrum. Then, the order of desorption for each state is deduced from the behaviour of T_P with coverage as can be seen from eq. (3.3). A first order desorption with a fixed activation energy is characterized by a constant T_P independent of the coverage. If the value of T_P decreases with increasing coverage, the desorption may be either of second order with fixed activation energy or of first order with an activation energy dependent on the coverage. After that, assuming a proper value for ν, estimates for Q can be made using the same equation.

A more sophisticated lineshape procedure has been developed considering the possible effects of readsorption to the surface [Winterbottom 1973]. The rate of desorption from binding state i is

$$\frac{d\theta_i}{dt} = \nu_i \theta_i^n \exp\left(\frac{-Q_i}{kT}\right) + \alpha_i P (2\pi m k T)^{-1/2} + F_i \quad , \qquad (3.5)$$

where α_i is the sticking probability for the i^{th} state and F_i is the net inter-conversion rate of other binding states to or from state i during the desorption. The total rate of desorption as obtained from the experimental spectrum through eq. (3.2) is then given by $d\theta/dt = \sum (d\theta_i/dt)$. The detailed procedure involves use of low, medium and high coverage desorption spectra to resolve the curve into its i components, making use of the fact that preferential filling occurs at low coverages of states with the highest activation energies. Best-fit values for

ν, n and Q pertaining to each binding state are finally extracted from the data.

A detailed statistical examination of the application of this procedure has, however, pointed to the uncertainties resulting from it [Pisani *et al.* 1974]. Figure 3.3 displays the results of a lineshape analysis of a single desorption curve with a two-state, β_1 and β_2, model. For the analysis presented in fig. 3.3 (a), it was assumed that the β_1 state desorbs with first order kinetics and β_2 with second order kinetics; while for fig. 3.3 (b) both were assumed to desorb with second order kinetics. No choice was possible between the two models, and even the statistical calculations indicated equivalent standard deviations from the experimental data. Actually, a wide range of values for both ν and Q was found to produce equally good "best-fit" curves. The conclusion was thus made that the analysis of complex desorption spectra is inherently ambiguous, even within the framework of the simple multistate model.

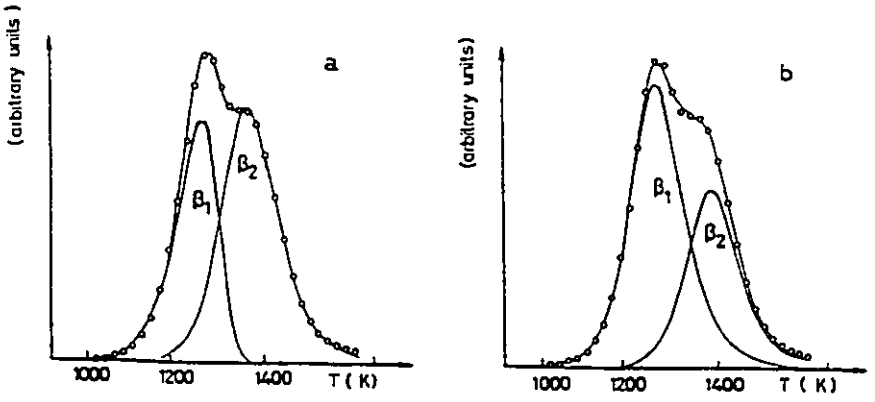

Fig. 3.3. Fit of a desorption curve de-convoluted into two components β_1 and β_2 according to (a) first order desorption for β_1, second order for β_2 and (b) second order for both binding states [Pisani *et al.* 1974].

3.2.2. The leading edge analysis

This is another complete method that derives the desorption energies from the experimental spectra with minimal assumptions on the attempt frequency and regardless of the surface coverage [Habenschaden *et al.* 1984]. The analysis starts from the PWE and assumes a linear heating regime so that

$$\frac{d\ln(d\theta_d/dT)}{d(1/T)} = -\frac{Q}{k} + \frac{d\ln(\nu/\beta)}{d(1/T)} + n\frac{d\ln\theta}{d(1/T)} \quad , \qquad (3.6)$$

where θ_d denotes the surface density of the already desorbed particles. The left side of eq. (3.6) is equivalent to $d[ln(P)]/d[1/T]$ where P is the measured pressure increase in the desorption experiment. Therefore, a plot of $ln(P)$ versus T^{-1} gives a straight line with a slope of $-Q/k$ as long as the variations of ν and θ with T may be neglected. To satisfy such a condition, a small temperature interval is selected at the low temperature-high coverage side of the desorption peak and an Arrhenius plot is constructed from that leading edge. The advantage of the leading edge analysis is that it rests only on one assumption that the variation of the desorption parameters is negligible over the temperature window of interest. However, the limitations of the procedure result from the need to measure the desorption rate or the pressure increase with high accuracy while the temperature region which may be used to extract Q is rather small. Numerical calculations have shown that the width of this region decreases with decreasing Q and as a result the accuracy is inherently low.

3.2.3. *Peak temperature method*

This is the most popular analytical method used in deriving the thermal desorption parameters from the experimental spectra. Ironically, the method was developed independently and simultaneously in 1962 by two scientists and has widely been referred to since then [Redhead 1962 and Carter 1962]. The main assumption made in this procedure is that the desorption energy is independent of coverage, so the PWE is treated as a simple differential equation. If eq. (3.3) is solved for T_P, the solution depends on the desorption order and may be written as

$$\frac{Q}{kT_P^2} = \left(\frac{\nu}{\beta}\right) \exp(-Q/kT_P) \quad \text{for } n = 1 \ , \tag{3.7a}$$

and

$$\frac{Q}{kT_P^2} = \left(\frac{\nu\,\theta_o}{\beta}\right) \exp(-Q/kT_P) \quad \text{for } n = 2 \ , \tag{3.7b}$$

where θ_o is the initial surface coverage. Since the order of desorption is readily deduced from the variation of T_P with coverage, the fixed energy of desorption can be then found directly using eqs. (3.7). Redhead found the relation between Q and T_P for first order desorption to be very nearly linear and, for the range $10^{13} > \nu/\beta > 10^8$ (K^{-1}), is given to $\pm 1.5\%$ by

$$\frac{Q}{kT_P} = \ln \frac{\nu T_P}{\beta} - 3.64 \quad . \tag{3.8}$$

The activation energy can be determined even without the need of assuming a value for ν. This is possible by varying β, plotting $ln(T_P)$ against $ln(\beta)$ and then deriving Q from

$$\frac{Q}{kT_P} + 2 = \frac{d(\ln \beta)}{d(\ln T_P)} \quad . \tag{3.9}$$

The attempt frequency can also be found by substituting Q back into eq. (3.7a). With increased heating rate, desorption peaks shift to higher temperatures and have larger amplitudes, but reach a maximum rate in a shorter time. For reasonable accuracy β must be varied by at least a factor of 10 between successive points on that plot. In some cases this application was successful even when the activation energy varies with coverage.

For second order desorption reactions, the initial surface coverage may be found from the area under the curve of desorption rate as a function of time. If $ln(\theta_o T_P^2)$ is plotted against $1/T_P$, a straight line is obtained with slope $-Q/k$. The attempt frequency is then determined by substitution into eq. (3.7b). The straight line behaviour of $ln(\theta_o T_P^2)$ versus $1/T_P$ can be used to distinguish between the two possibilities associated with the decrease of T_P with increasing coverage since a first order desorption with a coverage dependent activation energy does not yield a straight line relation.

A second feature of the peak temperature method is that the shape of the experimental curve of the desorption rate as a function of the sample temperature can be used to determine: (a) the order of the desorption reaction and (b) whether the activation energy is constant or a function of the surface coverage. Assuming a linear temperature ramping regime, integration of the PWE results in

$$-\int_{\theta_1}^{\theta_2} \frac{d\theta}{\theta^n} = \frac{\nu}{\beta}\int_{T_1}^{T_2} \exp\left(-\frac{Q}{kT}\right) dT \quad . \tag{3.10}$$

The left side is readily solved as $ln(\theta_1/\theta_2)$ for $n=1$ and $1/\theta_2 - 1/\theta_1$ for $n=2$. The integral on the right side may be evaluated by integrating by parts and expanding the argument to get

$$\frac{\nu}{\beta}\int_{T_1}^{T_2} \exp\left(-\frac{Q}{kT}\right)dT = \frac{\nu k}{\beta Q}\left[T_2^2\exp\left(-\frac{Q}{kT_2}\right) - T_1^2\exp\left(-\frac{Q}{kT_1}\right)\right]. \tag{3.11}$$

Then for the first order case, using eq. (3.7a), gives

$$\ln(\theta_o/\theta_P) = 1 - (T_o/T_P)^2\exp[-Q(T_P - T_o)/kT_PT_o] \approx 1 . \tag{3.12}$$

Therefore, at the temperature where the desorption rate peaks, the surface coverage is approximately given by 0.3679 θ_o. By substituting back into eq. (3.2), the shape of the desorption rate spectrum for first order kinetics can be

written as [Redhead 1962]

$$\ln\left(\frac{r_P}{r}\right) = \frac{Q}{k}\left(\frac{1}{T} - \frac{1}{T_P}\right) + \left(\frac{T}{T_P}\right)^2 \exp\left[-\frac{Q}{k}\left(\frac{1}{T} - \frac{1}{T_P}\right)\right] - 1 , \qquad (3.13)$$

where r_P is the desorption rate at T_P. It can be seen that, in this case, the desorption rate curve is asymmetric about the maximum at T_P (see, for example, fig. 3.4).

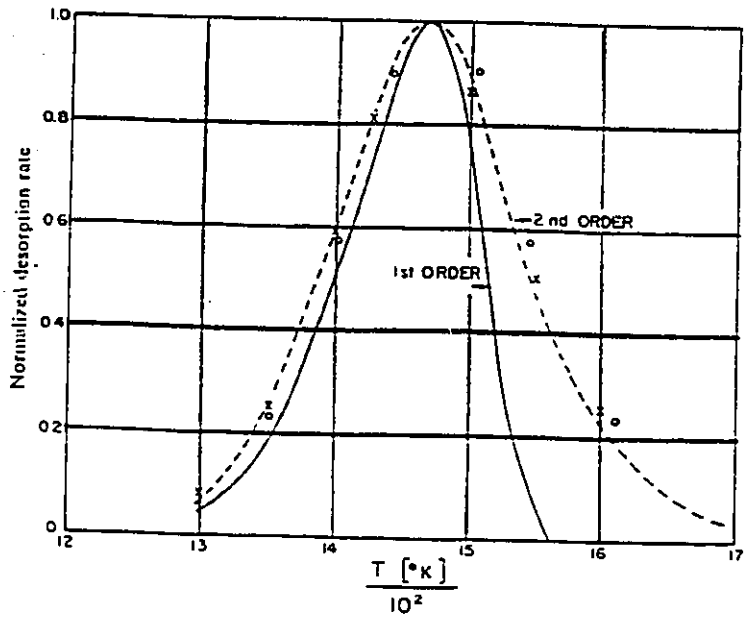

Fig. 3.4. Normalized desorption rate as a function of temperature for a first order (Q = 3.97 eV) and a second order (Q = 3.78 eV) reactions. The circles show the $\cosh^2$ approximation and the crosses indicate experimental points for which the spectra were obtained [Redhead 1962].

Similarly for the second order kinetics it can be shown that the surface

coverage at T_P is half the initial coverage and that the shape of the desorption rate curve is given by

$$\frac{r_P}{r} \approx \cosh^2[-\frac{Q}{2k}(\frac{1}{T}-\frac{1}{T_P})] \quad for \quad (\frac{T}{T_P})^2 \to 1 \quad . \qquad (3.14)$$

This means that the desorption rate curve is symmetric about the maximum T_P in the direct vicinity of the peak. Figure 3.4 shows the theoretical desorption rate spectra for a first order desorption with Q=3.97 eV, and a second order desorption with Q=3.78 eV. The $\cosh^2$ approximation for the second order case is shown by circles along the exact curve.

The above relationships can be used to determine independently the activation energy and attempt frequency from the desorption rate curves. From eqs. (3.2) and (3.7) and using the relations between θ_o and θ_P as derived in this section, the activation energy for first and second order desorption can be written as

$$Q = \frac{n r_P}{\beta \theta_P} k T_P^2 \quad , \qquad (3.15)$$

and similarly for the attempt frequency

$$\nu = \frac{n r_P}{\theta_P} \exp(\frac{n r_P T_P}{\beta \theta_P}) \quad . \qquad (3.16)$$

The peak temperature technique presents therefore a useful set of equations to determine the desorption parameters in an easy way. The main assumption made, of no dependence on the surface coverage, defines the limitation boundaries of the method. However, the reliance on the original PWE and the pictorial inspection of the parameter relationships allows for fair justification for employing the technique when used.

3.2.4. Shape analysis

Several attempts have been made to characterize the asymmetry of a thermal desorption spectrum with one parameter, which then serves as an indicator of the desorption order. The skewness parameter method [Chan *et al.* 1978] uses the fact that first and second order desorption peaks differ in their symmetry around T_P. The halfwidth skewness parameter $\chi_{1/2}$ is calculated from the peak maximum temperature and the two temperatures T' and T'' where the desorption curve has an amplitude equal to half the maximum rate, as shown in fig. 3.5 (a). Similar calculations are also made at three-quarters amplitude. The equation used is

$$\chi = 100 \times [(T'' - T_P) - (T_P - T')] / (T'' - T') \quad . \qquad (3.17)$$

First or second order desorption each correspond to a certain range of values for the skewness parameter, as defined in Table 3.1. The simplicity of the method and its ability to resolve the order of slightly overlapped peaks are what make it attractive.

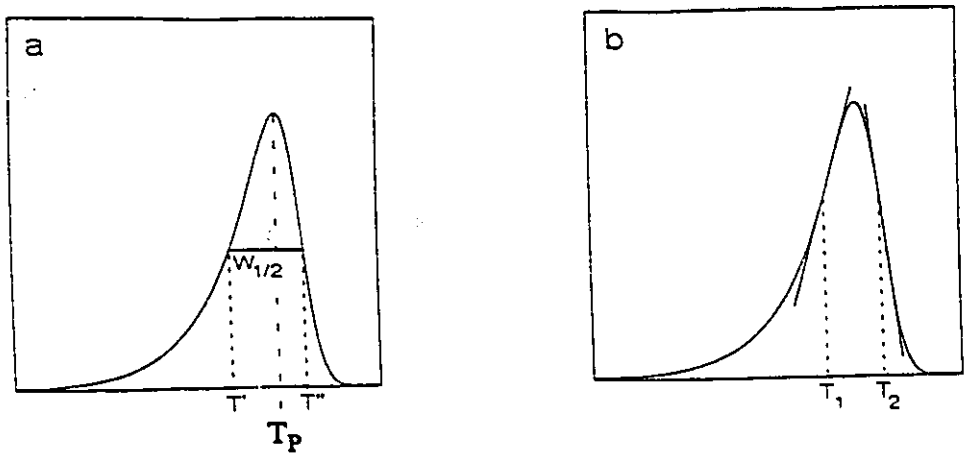

Fig. 3.5. Definition of parameters used in the shape analysis techniques: (a) The skewness parameter method [Chan *et al.* 1978]; (b) The shape index method [Konvalinka *et al.* 1977].

A similar approach but based on a differently defined property is the shape index method [Konvalinka *et al.* 1977]. The shape index σ is defined as the ratio of $-(dr/dT)_{T2}$ to $(dr/dT)_{T1}$ where T_1 and T_2 are the inflection points of the thermal desorption curves as shown in fig. 3.5 (b). The value of σ not only reveals the desorption order but also indicates whether or not readsorption of the desorbed species occurs. For the range of desorption energies where $Q/kT \gg 1$, the calculated values for σ are given in Table 3.1 for both first and second order desorption either when readsorption takes place or not. This method has the advantage of simplicity since it uses only one spectrum to characterize the desorption. However, it needs an accurate measurement of σ since the suggested values differ within a very short range that makes it often difficult to determine the desorption order.

Table 3.1
Predicted values for the skewness parameters $\chi_{1/2}$, $\chi_{3/4}$ and the shape index σ for first and second order desorption kinetics.

First order	Second order
$-18 < \chi_{1/2} < -15$	$3 < \chi_{1/2} < 5$
$-11 < \chi_{3/4} < -10$	$2 < \chi_{3/4} < 3$
$\sigma = 0.76$ no readsorption	$\sigma = 1.46$ no readsorption
$\sigma = 0.55$ equilibrated readsorption	$\sigma = 0.86$ equilibrated readsorption

A third method based on easily accessible features of the desorption spectrum is the peak width analysis [Edwards 1976]. If the desorption order is known, equations can be derived to express $Q(\theta)$ in terms of T_P and the peak width W, either at half or at three quarters of the maximum desorption rate. A number of equation sets exist in the literature, the most popular of which is the Chan-Aris-Weinberg (CAW) equations [Chan *et al.* 1978]. For a first order desorption

$$\frac{Q}{kT_P} = -1 + \left[1 + \frac{5.832\,T_P^2}{W_{1/2}^2}\right]^{1/2} \quad , \qquad (3.18a)$$

and

$$\frac{Q}{kT_P} = -1 + \left[1 + \frac{2.353\,T_P^2}{W_{3/4}^2}\right]^{1/2} \quad , \qquad (3.18b)$$

while for a second order desorption

$$\frac{Q}{kT_P} = 2\left[-1+\left(1+\frac{3.117\,T_P^2}{W_{1/2}^2}\right)^{1/2}\right] \quad , \qquad (3.18c)$$

and

$$\frac{Q}{kT_P} = 2\left[-1+\left(1+\frac{1.209\,T_P^2}{W_{3/4}^2}\right)^{1/2}\right] \quad . \qquad (3.18d)$$

These equations are easy to apply, valid over a wide range of parameters and allow Q to be estimated in two ways. The method apparently assumes that Q is independent of both the ramping rate and surface coverage. However, it is worth noting that $W_{1/2}$, $W_{3/4}$ and T_P are invariant with coverage for first order desorption, while $W_{1/2}$ and $W_{3/4}$ increase and T_P decreases as coverage increases for second order desorption.

3.2.5. Arrhenius plots

An inspection of the PWE shows that if the desorption spectrum is plotted as $ln(r/\theta^n)$ against T^{-1} for the three possible values of $n=\{0,1,2\}$, the plot corresponding to the correct order should be the one closest to a straight line. This method directly results in the best estimate of the desorption order and also gives averages of Q and ν over the spectrum from the slope and the intercept of the Arrhenius plot. An example of this method, applied on zeroth order

desorption spectra, has been reported on the study of lateral interactions between adsorbed Ag and Au on a ruthenium substrate [Niemantsverdriet *et al.* 1987].

3.3. Helium trapping in metals

Definite interpretation of thermal desorption curves of helium from metal surfaces is possible only under circumstances where simple release peaks are observed, for example the spectra shown in fig. 3.6 for the release of 250 eV helium implanted into a tungsten single crystal at different fluences [Kornelsen 1972]. Each implantation was preceded by a 8×10^{15} /m^2 5 keV Kr^+ damaging bombardment. In this case, the occurrence of simple, first order, single step release is confirmed by the characteristic width and shape of the low fluence peaks and by the observation that the temperature at which the maximum desorption rate was recorded is independent of the initial coverage. During such experiments, having established the mode of release, the activation energy and attempt frequency can be calculated on the basis of one of the theories discussed in the section 3.2. The same kind of analysis was carried out for several metals and under various implantation conditions. A first order helium desorption peak was observed for example in a pre-damaged molybdenum crystal implanted with 250 eV helium to a fluence of 1.9×10^{17} m^{-2} [van Veen *et al.* 1975], in an annealed single crystal of nickel implanted with 400 eV He^+ to a fluence of 5.6×10^{16} m^{-2} [Edwards *et al.* 1974] and in polycrystalline silver implanted with 20 keV He^+ to fluences ranging from 5×10^{20} to 5×10^{21} m^{-2}.

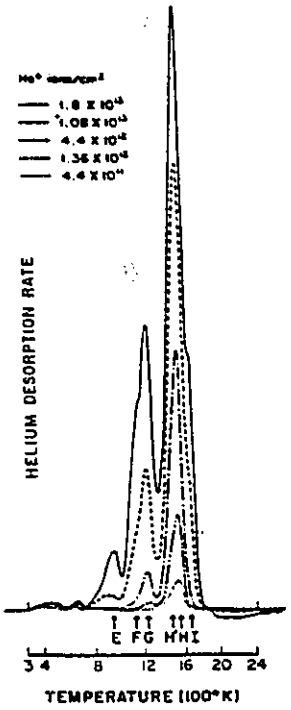

Fig. 3.6. Desorption spectra for helium from tungsten. Helium fluences are indicated. A damaging beam of 5 keV Kr preceded each implantation [Kornelsen 1972].

Typical desorption spectra, however, are complicated by the presence of release transients that do not allow certain determination of the nature of the desorption processes. For these types of spectra, a more qualitative approach, based on the classification of the gas release processes into a number of different stages has generally been adopted [Kelly *et al.* 1967]. The method is based on the analysis of a number of different ion-solid systems over a wide ion energy range. The release is divided into five stages which are broadly grouped into release below, at and above the temperature of normal self-diffusion in the material concerned.

The lowest release temperature, stage IA, which occurs close to the

implantation temperature, is associated with gas located in non-normal lattice positions (*e.g.*, interstitial sites) or in irregular high mobility sites close to the surface where strain fields or impurity effects may influence the migration process. This is followed by stage IB which is considered to be due to gas release from normal lattice sites via some form of defect or disorder annealing process such as migration of radiation induced vacancies. Gas release at temperatures close to normal self-diffusion temperatures is described by stages IIA and IIB where the former is due to gas migrating by the appropriate self diffusion mechanism for the solid material and the latter, which occurs at higher temperatures, refers to a similar movement hindered by processes such as temporary retrapping at stable defect sites or collective interaction with other gas atoms.

The final release stage, stage III, is only observed at high gas concentrations where significant cooperative effects occur and is due to the release of gas from highly stable bubbles. Generally, gas trapped in this type of site only becomes mobile at temperatures close to the melting point of the host material and the observed release is often related to the evaporation of the surface. These release stages categorize the interaction of the gas atoms with various types of radiation produced damage from the points of view of both trapping and subsequent thermally activated migration. That is why experimental studies of helium diffusion in metals are actually directed to the investigation of this phenomenon as a probe for lattice defects.

In thermal desorption experiments, helium release that can be associated

with all five stages has been observed in a number of metals. For example, in the case of helium desorption from type 304 stainless steel [Carter *et al.* 1980], the release data have been interpreted in terms of trapping in sites which exhibit either a continuum of activation energies or discrete energies which are too closely spaced to be experimentally resolved. Figure 3.7 illustrates the desorption rates of various 1 keV He fluences from stainless steel.

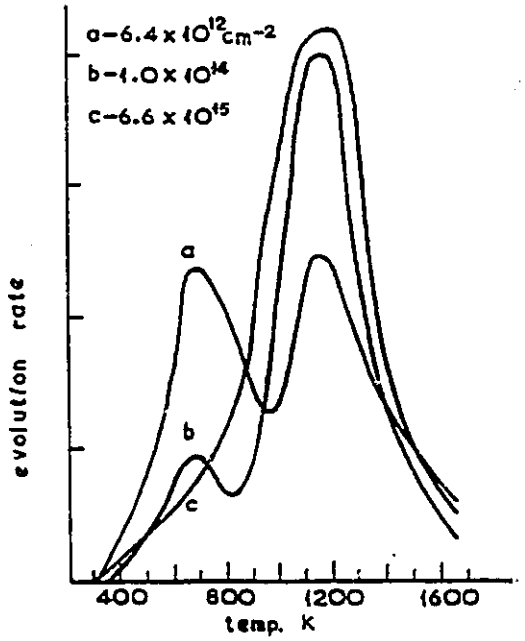

Fig. 3.7. Fluence dependence of the desorption spectra of 1 keV He^+ implanted into type 304 stainless steel [Carter *et al.* 1980].

The release can be roughly divided into low and high temperature regions centred around temperatures of 700 K and 1150 K. Both peaks are, however, considerably wider, by a factor of about four, than those expected for single

activation energy processes and the explanation that a range of activation energies is involved seems reasonable in view of the complexity of the material. On the basis of the marked similarities in the helium release behaviour in both the low and high temperature regions, the release below 800 K has been tentatively ascribed to vacancy migration. The absence of any significant broadening or temperature shift in the high temperature region of the spectra for an energy increase up to 450 keV suggests that a substitutional mechanism, rather than diffusion, is responsible for the release.

Another interesting and analytically useful feature of helium release from metals is the change that occurs in the occupancy of sites that contribute to the very high (stage III) and very low (stage IA) temperature release regions as the fluence is increased. For the case of low energy implantation into single crystal nickel, the dependence of the desorption curves on fluence is dominated, as shown in fig. 3.8, by the dramatic increase in the relative population of an extremely narrow, high temperature release peak. Over the range of fluences in which this peak grows, the trapping probability (*i.e.*, the ratio between trapped and incident helium fluences) increases by approximately 40%. This indicates that under these implantation conditions, fundamental changes in the nature of the trapping sites occur.

Although the peaks are too wide to allow analysis in terms of first order methods, the combined observations of the presence of a broad but distinct peak and the fluence dependent trapping coefficient do suggest that vacancies act as efficient trapping centres for the implanted helium and hence the observed peaks

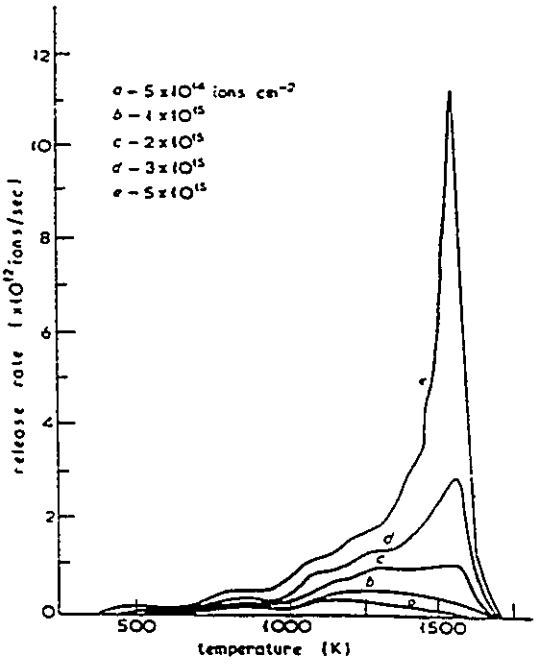

Fig. 3.8. Desorption rate spectra of 1 keV helium ions implanted randomly into a single crystal of nickel as a function of the incident fluence [Carter 1980].

may be attributed to the dissociation of HeVCs. These clusters were formed either during implantation or by agglomeration at the early annealing stages of the desorption cycle. The increase in the trapping probability with fluence is explained if it is assumed that helium occupancy of vacancies inhibits their annihilation by SIAs by a factor related to the number of helium atoms trapped in each site; then it follows that the total vacancy-related trap concentration, and hence the trapping probability, should increase with fluence. As for the variation of the trapping coefficient with the incident energy, a similar correlation with radiation-produced damage has been observed. Experiments on polycrystalline nickel give a 100% trapping probability for 20 keV helium ions up to the critical

fluence for blistering [Zelenskij *et al.* 1987].

At high fluences, helium release becomes more related to the kinetics of agglomeration and growth of bubbles rather than dissociation from simple traps. Although thermal desorption is not the primary technique used to characterize these processes, it has proven useful in associating high temperature release peaks to surface blister and bubble bursts. The work of Kornelsen *et al.* (1980) in detecting the early stages of helium bubble nucleation and growth in tungsten has been described in detail in Chapter 2. Significant helium release and surface deformation in the form of blisters has been found below 430 K on palladium samples implanted with 2×10^{22} 300 keV He/m^2 helium atoms at 90 K [Bauer *et al.* 1972]. The release was attributed to inter-bubble partial connection and the deformation of the surface due to high internal gas pressure. Desorption studies of nickel after 10^{21} ^{3}He/m^2 implantations have been analyzed by a single-step first order mechanism for the release below 570 K, while above that temperature, the opening of helium bubbles to the surface independent of any diffusion process was the release rate determining process [Ehrenberg *et al.* 1983].

3.4. Helium trapping in beryllium

Initial interest in the study of helium precipitation in beryllium developed when the metal was proposed as a cladding material for fission fuel pellets. The main area of study was the effect of helium swelling at high temperatures on the material performance [Barnes 1959]. With the advancement of the fusion

technology over the past two decades, beryllium has emerged as a leading candidate as both tritium-breeding blanket and low-Z coating material to plasma facing components in the International Thermonuclear Experimental Reactor (ITER). This candidacy received a major boost when beryllium was directly connected to the improved results obtained from the Joint European Torus (JET) [Thomas *et al.* 1990].

In these applications, beryllium provides the interface material between the plasma and the confinement structure. Helium is produced by three possible processes: direct bombardment from the burning plasma, the $^{9}Be(n,2n)2\alpha$ and $^{9}Be(n,\alpha)\,^{6}He(\beta^{-})\,^{6}Li(n,\alpha)\,^{3}H$ transmutation reactions and by the tritium natural decay to ^{3}He according to

$$^{3}H \xrightarrow[12.3\,y]{\beta^{-}} {}^{3}He \quad .$$

The main end product of all these processes is the accumulation of helium within the material bulk resulting in high levels of gas driven swelling and embrittlement at high temperatures. Plasma-facing materials are judged, among other factors, by their ability to retain their helium content under the reactor operating conditions. Thermalised helium atoms are oftenly referred to as "helium ash" and their removal from the plasma environment is an important issue in sustaining a long pulse D-T reaction [Krauss *et al.* 1990]. The atomistic nature of helium trapping and bubble nucleation and growth suggests that slightly porous beryllium microstructures (*e.g.*, from powder metallurgy), are more effective in retaining significant amounts of helium [Wilson *et al.* 1990].

Few experiments involving helium implantation of beryllium have been performed. The earliest published data on helium desorption from beryllium was obtained as part of a study on the diffusion and trapping of deuterium and the effect of helium on the deuterium release [Macaulay-Newcombe *et al.* 1991]. A reported spectrum of 30 keV helium implant to a fluence of 10^{21} m^{-2} showed two desorption peaks centred around 728 and 833 K, of which the latter was linked to trapping sites at microbubbles.

Another study of helium diffusion in beryllium at low concentrations ($<3\times10^{-6}$ appm) used isothermal and linear ramping of uniformally implanted foils [Jung 1993]. The desorption curves indicate a diffusion-controlled release mechanism with activation energy Q=0.6 eV. A strong dependence of the effective diffusivity on the helium concentration was also reported and the helium migration was strongly hampered by clustering causing substantial retention even at temperatures above 1200 K ($\approx 0.77\ T_m$).

Thermal desorption spectra of low energy (3 keV), low fluence ($\leq 4\times10^{19}$ $^3He/m^2$) implanted beryllium have shown that helium is released at three dominant peaks between 850 and 1150 K [Eleveld *et al.* 1994b]. The individual desorption peaks, shown in fig. 3.9, were too wide to be associated with a first order desorption process and have been attributed to a thermal vacancy assisted diffusion mechanism. When ^3He was implanted at a higher energy (30 keV) and to higher fluences (0.1, 0.95 and 7.7×10^{20} He/m^2), investigations through positron annihilation and neutron depth profile techniques have shown that helium bubbles nucleate around 500 K, before the helium release at $T>975$ K.

Increasing the fluence above 7.5×10^{20} He/m^2 has resulted in a reduction of the helium release temperature by more than 100 K. This is consistent with the helium residing in bubbles, since more time would be needed for bubble growth with lower fluences before reaching the surface, hence the higher release temperature. The authors reported no thermal desorption measurements on the 30 keV ^{4}He implantations.

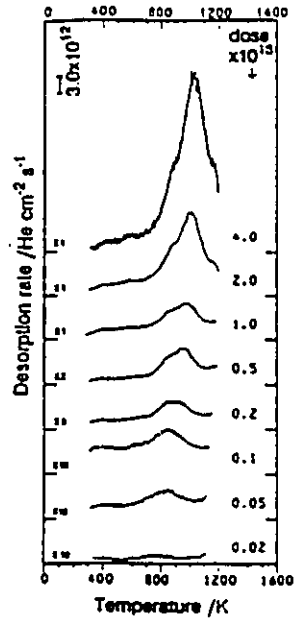

Fig. 3.9. Desorption rate spectra of 3 keV He^3 ions implanted into beryllium. The quoted fluence variation is in He/cm^2 [Eleveld *et al.* 1994b].

The maximum attainable helium concentration in beryllium is a strong function of the material microstructure (which defines the surface porosity) as well as the implantation energy and temperature (which are directly related to the profile of deposited helium within the bulk). Measurements for a 20 keV ^{4}He ion beam have shown that 100% helium retention is achieved before the critical

fluence for blister formation (at 2.6×10^{21} He/m^2 at room temperature and 2.3×10^{21} He/m^2 at 550 K for hot-rolled 99.5 % pure beryllium samples) [Ross *et al.* 1980]. An earlier investigation using 15 keV He^+ beam reported the formation of blisters at a fluence lower than 3×10^{21} He/m^2 for samples that were cut from sintered 99.8% pure material [Verbeek *et al.* 1974]. For 5 keV implantations in beryllium samples prepared in two stages (cold isostatic pressing followed by a hot isostatic pressing) helium shows 100% trapping up to a fluence of 1.75×10^{21} He/m^2 [Langley 1979]. High temperature implantations with 4 keV helium beam in high density beryllium have resulted in a critical fluence of 10^{21} He/m^2 at 675 K that is reduced substantially to $<2\times10^{18}$ He/m^2 at 975 K [Pontau *et al.* 1980].

CHAPTER 4

Experimental Procedures

4.1. Sample preparation

The material used in this study is 0.5 mm thick beryllium foils, prepared and denoted as PF-60 by Electrofusion Corporation. The specimens are manufactured by hot isostatic pressed (HIP) powder metallurgy with a quoted purity of 99.5 wt% Be, where BeO is the major impurity. The chemical composition of the samples as specified by the supplier is given in Table 4.1. All foils have been roughly polished and ultrasonically cleaned before shipment.

Table 4.1
Chemical composition in wt% of the beryllium samples as specified by the manufacture

Be	BeO	Fe	C	Si	Al	N	Others
99.5	<0.7	<0.05	<0.04	<0.02	<0.01	<0.01	<0.043

An etchant of 5% nitric acid in distilled water has been used to reveal the grain boundaries. Secondary electron images of the surface were taken using a 2 kV accelerating voltage from a LaB_6 electron source. Although the images

showed a distribution of grain sizes within the range 3 to 51 μm, the average grain size amounted to 18-21 μm.

Prior to the helium implantation all samples were mechanically polished in two stages. First a rough polish was given using 1% sulphuric acid in distilled water on 1200 grit silicon carbide paper. Then a mirror-like finish was developed on a polishing wheel using a slurry of 0.05 μm alumina in deionized water. Polishing particles were cleaned off after each stage by ultrasonic cleaning in acetone.

Some of the polished samples were annealed at 1023 K for 1 hour in a vacuum of $\approx 10^{-4}$ Pa to grow a thick surface oxide layer. Surface analysis of the oxide thickness and surface contaminants was performed by Rutherford Backscattering (RBS) before implantation. The unannealed samples were found to have a BeO layer with a uniform thickness of $\approx$3.3 nm after polishing compared to a minimum of 22 nm on the "as-received" surfaces. The deliberately corroded surfaces had a nonuniform layer of beryllium "oxy-carbide" with an average thickness of 28 nm.

4.2. Ion implantation

Over the course of this work, 70 beryllium samples were implanted with 30 keV ^{4}He ions incident normal to the sample surface. Total implantation fluences ranged from 1.5×10^{19} to 10^{21} He^+/m^2. This corresponds to a

maximum helium concentration in the range (0.1 - 7.5 at%) as predicted by the Monte Carlo TRIM95 code [Biersack *et al.* 1980]. The use of a mono-energetic beam for the implantation creates a well-defined helium deposition region and associated lattice defects. Damage is introduced along with the helium atoms due to the lattice displacements produced by the energetic implanted ions. This renders difficult measurements of perfect lattice diffusion parameters, but is ideal when defect trapping is the property of interest as in the present study. The peak helium concentration and the associated radiation damage for the investigated fluences are listed in Table 4.2.

Table 4.2
Implantation parameters

Implantation fluence (He m^{-2})	Peak helium concentration (at %)	Peak radiation damage (dpa)
1.5×10^{19}	0.11	0.02
1.0×10^{20}	0.75	0.12
2.5×10^{20}	1.88	0.30
5.0×10^{20}	3.76	0.60
7.5×10^{20}	5.64	0.90
1×10^{21}	7.52	1.20

The displacement dose and peak helium concentration were calculated assuming a 20 eV displacement threshold energy. According to these calculations, the atomic concentration of the injected helium is maximum at a depth of 335 nm below the specimen surface with an average range of 315.2 ± 54.5 nm. Each helium ion creates 61 Frenkel pairs on average. A schematic illustration of the depth distribution of 30 keV helium beam and the

associated atomic displacements predicted for a typical implantation in a beryllium target is shown in fig. 4.1. It should be noted here that TRIM calculations assume no diffusion of either the injected helium atoms or vacancies during implantation.

The pressure of the beam line was kept below 2.7×10^{-4} Pa by diffusion pumps and a liquid nitrogen trap in front of the sample holder. The ion beam was scanned in both the vertical and horizontal directions across an area of 2.5×10^{-3} m^2 to ensure uniform implantation fluences. For room temperature implantations, the beam heating effects on the samples were minimized by water-cooling the copper target holder to which the beryllium samples were clamped.

For each set of samples, the He^+ beam intensity at the target was maintained at a constant level, usually corresponding to the maximum derived current density from the machine just prior to the implantation. The aim was to avoid any break in the implantation to more than one session, hence raising the current to minimize the time required. The total time for all the implantations fluctuates between 40 minutes and 6 hours, with the implantation current density varying within the range of 1 to 7.4 mA/m^2 from run to run.

High temperature implantations were carried out at 600 and 773 K using a special sample stage, equipped with resistive heater coils with current capabilities sufficient to raise the target temperature up to 773 $\pm$ 10 K. The temperature was monitored during the implantation through a thermocouple attached to the sample holder.

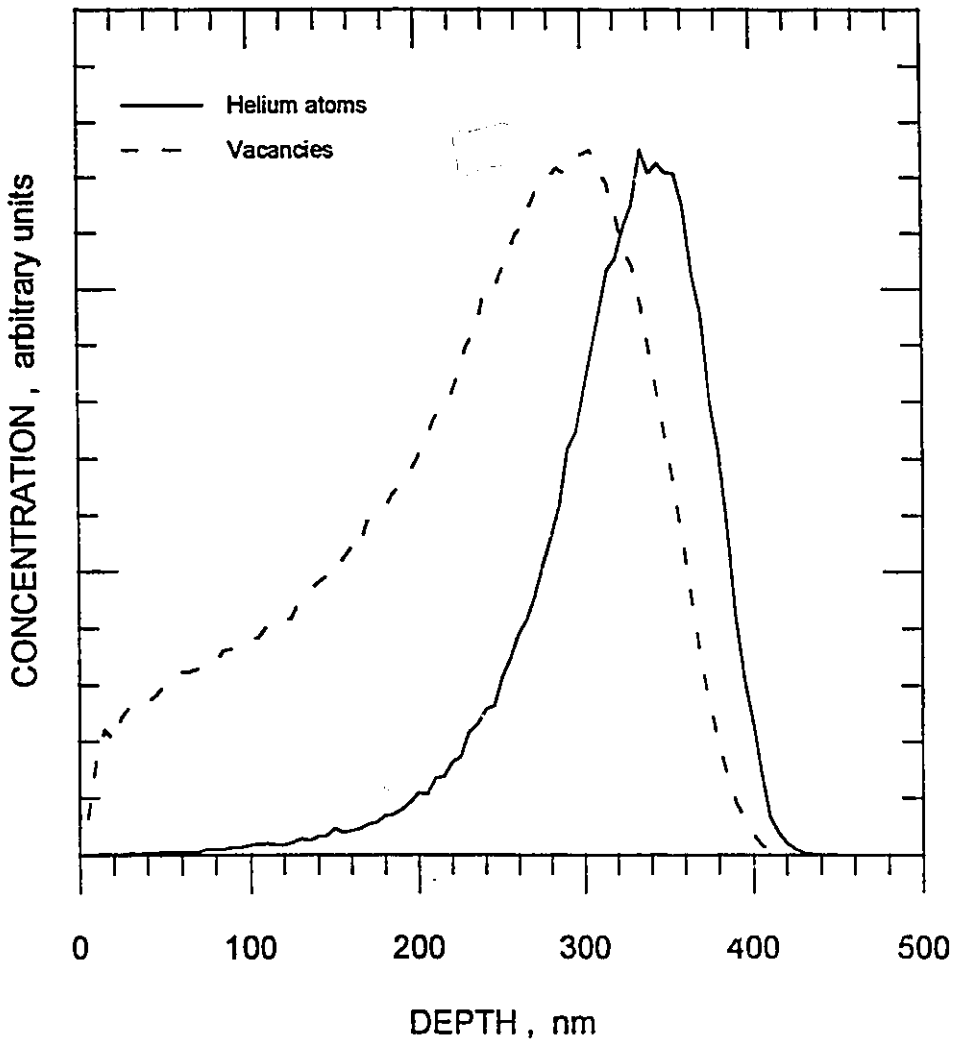

Fig. 4.1. Projected range and radiation damage distributions of 30 keV ^{4}He ion-implantation in Be for normal incidence as simulated by *TRIM95*. Total ions calculated= 75000, displacement energy= 20 eV, lattice binding energy= 2 eV, average range= 315.2 nm, range straggling= 54.2 nm, vacancies created per ion= 61.

4.3. Thermal desorption apparatus

An ultra-high vacuum apparatus, depicted in fig. 4.2, was used for thermal desorption measurements. The desorption chamber was pumped with a Leybold-Heraeus turbomolecular pump, model TMP 150, with a base pressure of 10^{-7} Pa at room temperature and 10^{-6} Pa when the sample is at elevated temperatures. The primary residual gases in the chamber were H_2, CO and CO_2. Turbomolecular pumps are characterized by a performance curve that shows a direct relationship between the quantity of gas (measured in pressure-volume units) pumped per unit time, φ, and the gas pressure below a certain threshold value. The proportionality constant is the pumping speed, s, and it depends generally on the mass of the species, so that for a specific gas component i, $\varphi_i = s_i P_i$, with P_i the partial pressure of the i^{th} gas. The TMP 150 is specified by the manufacturer as having $s_{He} = 0.135$ m^3/s for $P_{He} < 0.2$ Pa.

The helium partial pressure was measured with a Leybold-Heraeus quadrupole mass spectrometer (QMS), model Q-100. The QMS sensing head is equipped with an electron multiplier that enables it to measure partial pressures down to 10^{-11} Pa, corresponding to a minimum helium flux rate of 5.5×10^{12} molecules m^{-2} s^{-1}. Mass scans are controlled by feeding the sensing head with a DC voltage, in any user-specified fashion, to detect masses within the range of 1 to 100 amu. Two outputs may be drawn from the control panel, one for the total system pressure and another for the partial ion current reflecting the composition of the residual gas in the desorption chamber. The partial ion current signal is amplified and filtered by the mass spectrometer internal circuits

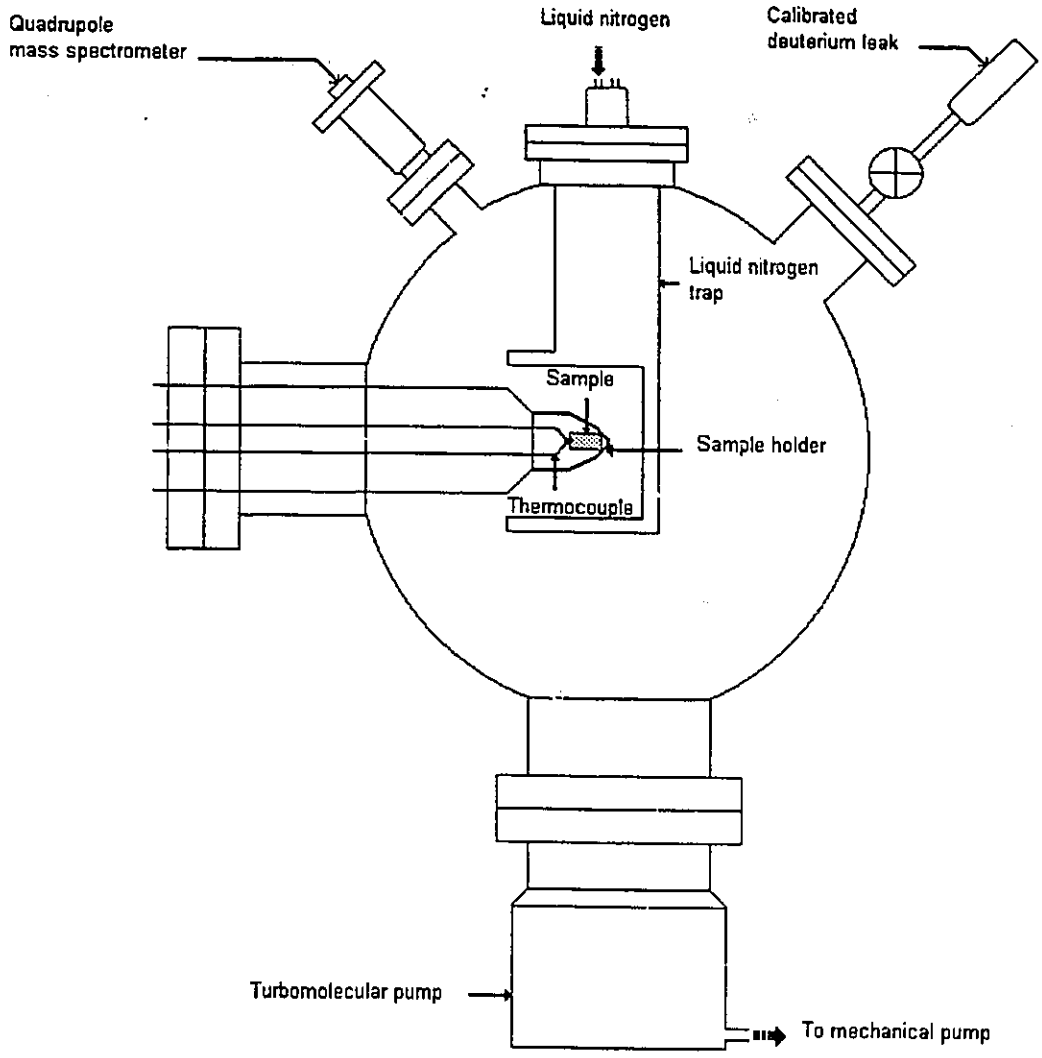

Fig. 4.2. Thermal desorption apparatus.

with both the time constant and the amplification range selected from the control panel.

The helium flux measurements were calibrated using a standard leak that provides a constant deuterium leak rate of 4.38×10^{12} mol/s. The leak value is quoted by the manufacturer as being accurate to within 10%. The linear pumping speed of the turbomolecular pump, when combined with the high sensitivity of the electron multiplier and the calibration procedure, enables accurate measurements of the residual gas intensities.

In order to minimize oxidation of the samples at high temperatures, the sample was shielded by a liquid nitrogen trap except in the direction facing the QMS. The cryopump was continuously supplied with liquid nitrogen from a reserve dewar and was kept filled during the desorption cycle. Furthermore, the desorption chamber was baked out between successive runs, normally at 353 K overnight, by a heater tape strapped around it. This significantly reduces the partial pressures of oxidizers such as H_2O, O_2 and carbon oxides in the desorption chamber.

Two approaches were used to control and measure the sample temperature during the ramping process. First, two tantalum wires were spot-welded near the edges of both the front and back surfaces of the sample. The wires were heated resistively which, in turn, heated the sample. The temperature was measured using a 0.25 mm chromel-alumel thermocouple spot-welded into a small notch filed on the unimplanted surface. However, considerable difficulties were

encountered in mounting the wires so that they did not break or pop off at high temperatures. Another arrangement was then used where a bee-hive shaped alumina coated evaporator was used to heat the sample. The heating wires were directly attached to the evaporator with the thermocouple simply pressing against the sample surface. This construction allowed the same configuration to be used for many thermal cycles, reducing the time lapse between consecutive runs. Thus replacing the samples could be carried out only in a few minutes and the time needed to bake out the chamber after each opening was significantly reduced.

Between implantation and desorption, samples were stored at room temperature in a desiccator. When the helium desorption curves exhibited a dependence on the ages of the implanted samples, the age factor was examined by storing a batch of implanted samples, directly after implantation, at liquid nitrogen temperature. It should be mentioned, however, that samples had to be brought back to room temperature for at least 8 hours before desorption when they were loaded into the desorption chamber and the system was left to pump down overnight.

The sample temperature was controlled with the aid of a Eurotherm digital controller, model 808. During the desorption regime, the controller sets a temporary temperature frequently, according to the ramping rate specified by the operator. The temperature is then compared to the feedback from the thermocouple and the output heating power to the sample holder is adjusted accordingly. The control accuracy as provided by the manufacturer is $\pm$ 1 K. The Eurotherm output passes through a proportional controller that provides an

AC voltage to a step down transformer which, in turn, drives a variable transformer (0 to 100% of input voltage) for better power control of the sample. The ramp rate was adjustable between 0.01 and 99 K/min. Through the controller, the temperature deviation was kept within $\pm$ 5 K of the desired value over the duration of the ramping. The deviation was usually within $\pm$ 2 K at temperatures $>$ 373 K.

Some samples were heated at a constant rate up to 1173 K with a ramping rate within the range of 2 to 20 K/min. Another desorption regime involved a step-annealing temperature rise, where the sample would be rapidly heated (20 K/min) to an elevated temperature (573 or 773 K), kept there for two hours and then heated again with a slower ramping rate (3 or 5 K/min) up to 1173 K.

4.4. Data acquisition

At the beginning of the desorption experiment, a ramping rate is selected and the controller set point is raised to the final temperature. This process causes a prompt start of the temperature ramping, with the option of turning the computer-controlled QMS on and off at any time. An existing data acquisition program, NUGATHER [Riehm 1990 and Shi 1991], has been expanded and renamed DESORBER to allow simultaneous monitoring of up to 8 species per scan of the chamber background gas composition, setting the initial and final temperatures as the boundary for the data collection cycle and allowing for on-line conversion of each of the collected signals to desorbed flux versus

temperature release spectrum.

During the desorption cycle, a residual gas analyzer (RGA) measured the mass 4 peak together with seven other user-specified "windows". Usually masses 1 (H), 2 (H_2, D), 3 (HD), 4 (He, D_2), 16 (O), 17 (HO), 18 (H_2O) and 19 (HDO) were monitored. The mass scan is computer controlled; the output from a digital-to-analog (D/A) converter is the input to the sensing head and the computer monitors the partial pressures of the residual species from the ion current output via an A/D converter. For each desorption run, there was a flux correction made on the collected spectra by calibrating the system at the end of the run.

The partial pressures of interest were scanned at regular intervals specified by the user (normally a complete scan per 10 seconds) and the signals saved periodically as a function of time. DESORBER terminates the data collection process when the temperature reaches its designated maximum value. In converting the helium partial current to its corresponding flux value, a stored value of the calibrated flux (F_{CAL1}) is used. At the end of the desorption run, and before letting the chamber to atmospheric pressure, the deuterium flux is calibrated again (F_{CAL2}) and the stored helium flux is corrected using the ratio (F_{CAL2} / F_{CAL1}). The saved files could then be scaled to the proper units, plotted and analyzed to determine the desorption parameters of interest after each run.

Surface structure changes have been observed by SEM at different stages of the implantation-desorption routine. At least one specimen from each sample set was investigated after desorption in an attempt to relate any surface

modification to the helium release process. For the samples desorbed by the step-annealing procedure, surfaces were investigated at the beginning and end of the waiting time interval within the desorption cycle, even if helium was never detected before the second ramping stage. However, the images proved useful in confirming the surface status at that stage and simultaneous X-ray analysis showed the growth of the surface oxide during the annealing stage.

CHAPTER 5

Results and Analysis

5.1. Introduction

Beryllium is considered a prime candidate for use as a plasma-facing material in fusion reactors where it will be subjected to continuous bombardment by helium ions and α-producing neutrons. In the present work a series of ion implantation/thermal desorption experiments have been designed to obtain fundamental insight on the behaviour of helium in beryllium. Electron microscope images have also been used to relate the observed desorption spectra to changes in the surface morphology. The nature of helium trapping and release mechanisms has been found to strongly depend on the concentration of defects in the samples as well as on the post-implantation annealing regime.

In section 5.2, the results of a parametric study of the dependence of the desorption parameters on the implantation fluence are presented. Included is an examination of the effect of sample ageing after implantation on the desorption spectra. Results from a step-annealing desorption procedure and thermal ramp desorption after high temperature implantations are given respectively in sections

5.3 and 5.4. Electron microscope images showed that helium desorption in these cases is associated with the formation of surface blisters and holes indicative of a transition from helium trapping at simple defects to the nucleation and growth of helium bubbles. Finally, section 5.5 presents the desorption results of beryllium samples that have been deliberately corroded before implantation to study the effect of the surface oxide on the trapping and release behaviour of helium.

5.2. Effect of the implantation fluence

5.2.1. TDS measurements

Thermal desorption was carried out with beryllium samples implanted at room temperature to different helium fluences in the range 10^{20} to 10^{21} He^+/m^2. The temperature was ramped from room temperature up to 1073 K ($\approx 70\%\ T_m$) at either 3 or 5 K/min. The results of the ramping rate variation for four of the investigated fluences are shown in figs. 5.1 to 5.4. Figure 5.5 displays a 5 K/min spectrum for the 10^{21} He^+/m^2 implantation. A low fluence of 1.5×10^{19} He^+/m^2 was also examined but the desorption spectra displayed no significant helium release even though, for one sample, the temperature was raised as high as 1273 K ($\approx 81\%\ T_m$).

The shapes of the helium release spectra indicate a gradual dependence on the implantation fluence. A distinction can be made between two observed

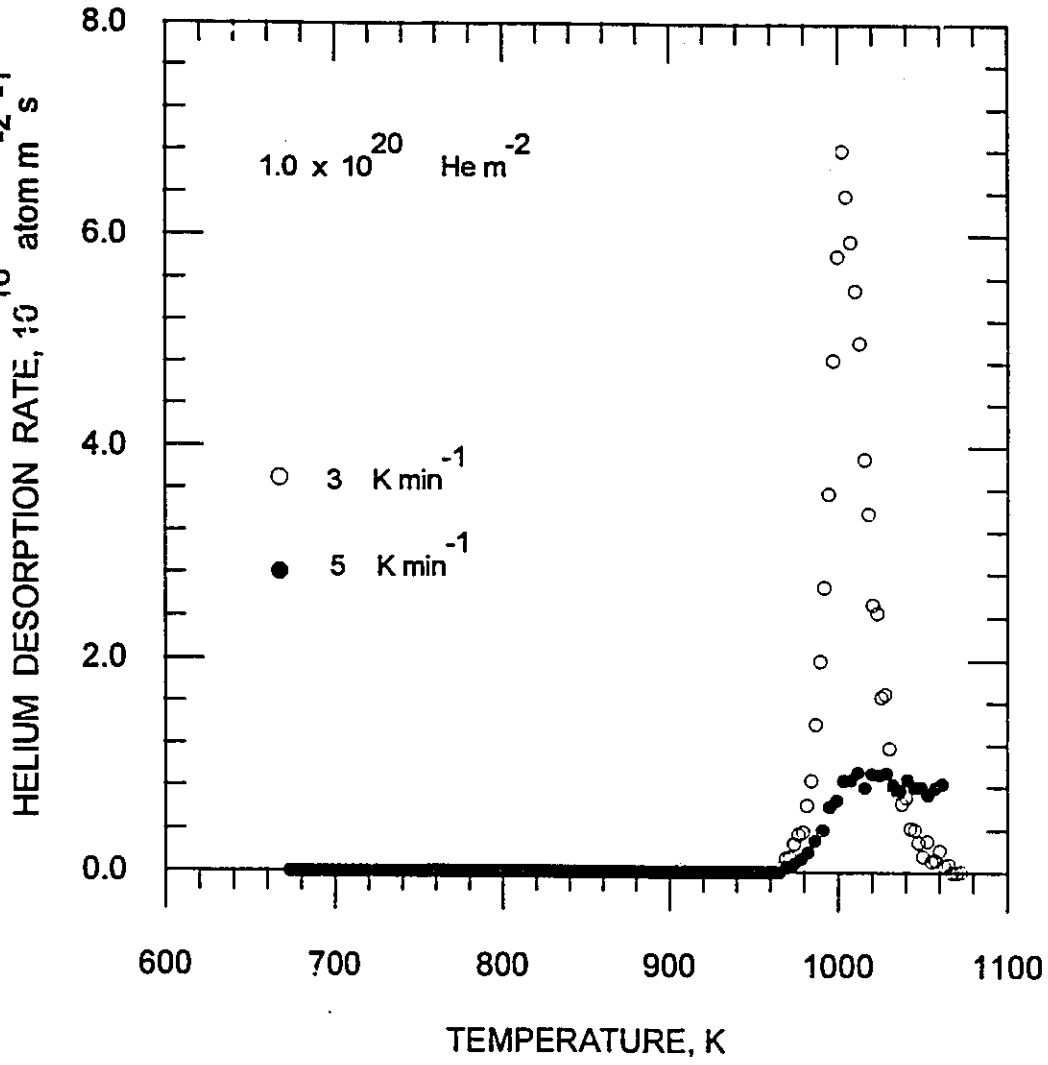

Fig. 5.1. Thermal desorption spectra for 30 keV helium implanted beryllium to a total fluence of 10^{20} He^+/m^2.

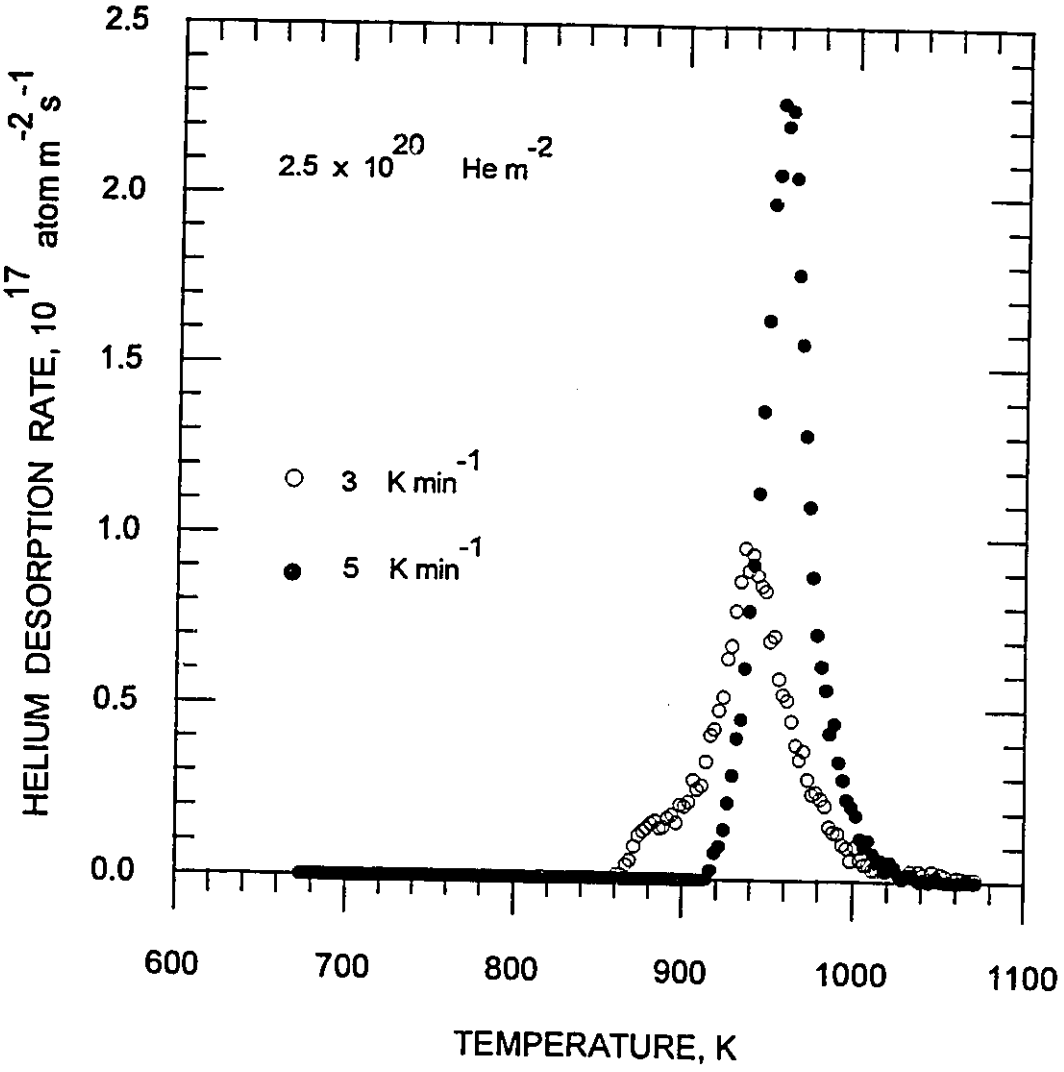

Fig. 5.2. Thermal desorption spectra for 30 keV helium implanted beryllium to a total fluence of 2.5×10^{20} He^+/m^2.

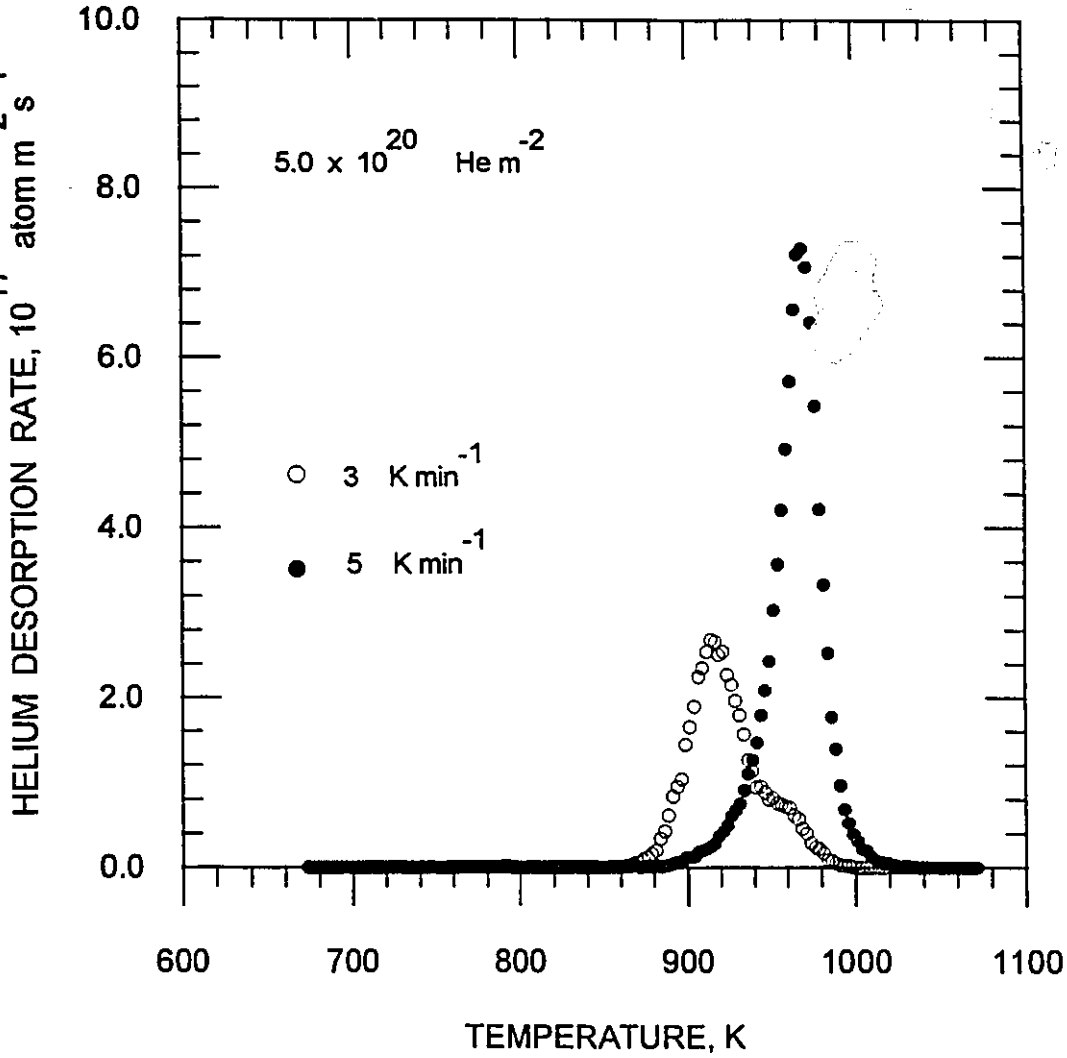

Fig. 5.3. Thermal desorption spectra for 30 keV helium implanted beryllium to a total fluence of 5×10^{20} He^{+}/m^{2}.

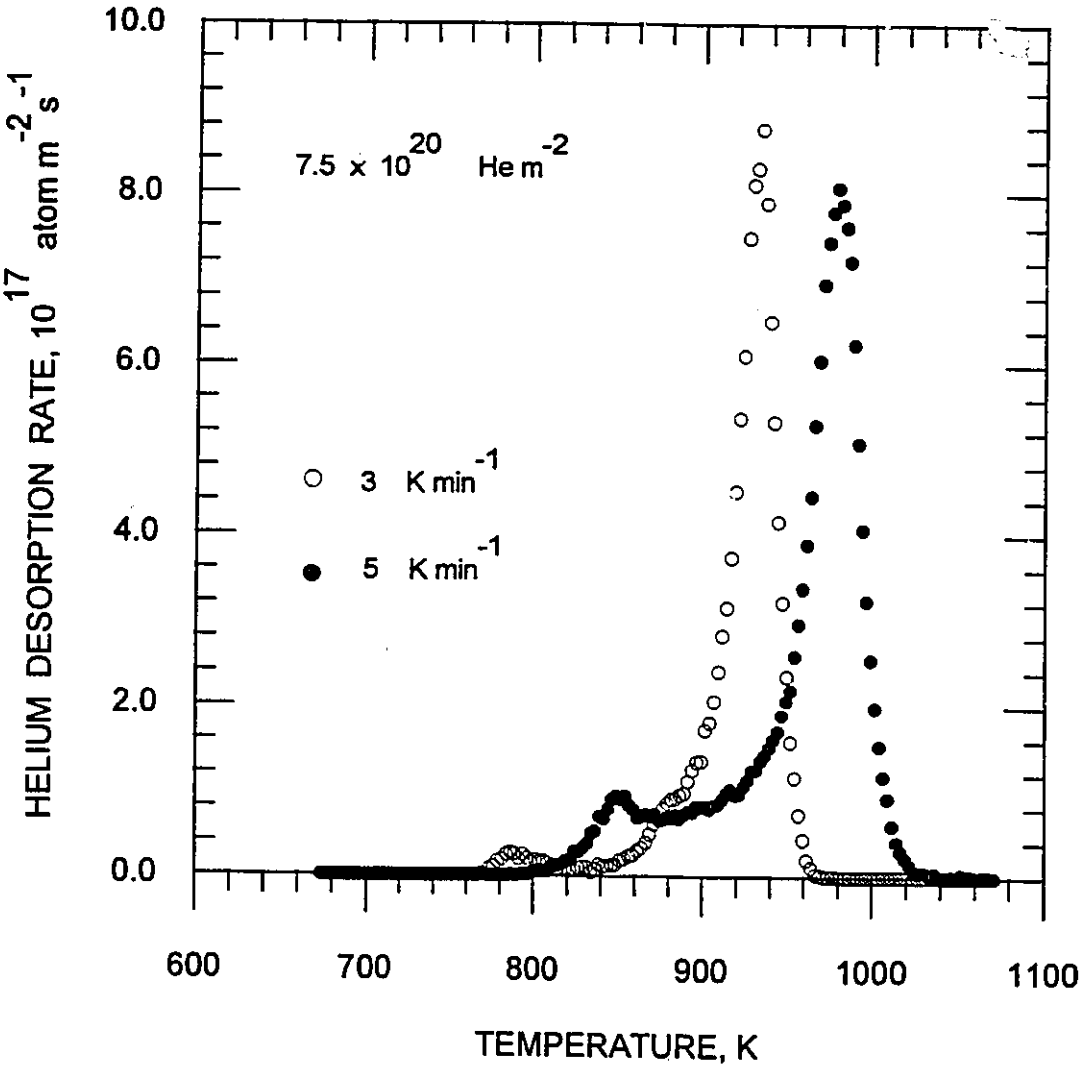

Fig. 5.4. Thermal desorption spectra for 30 keV helium implanted beryllium to a total fluence of 7.5×10^{20} He^+/m^2.

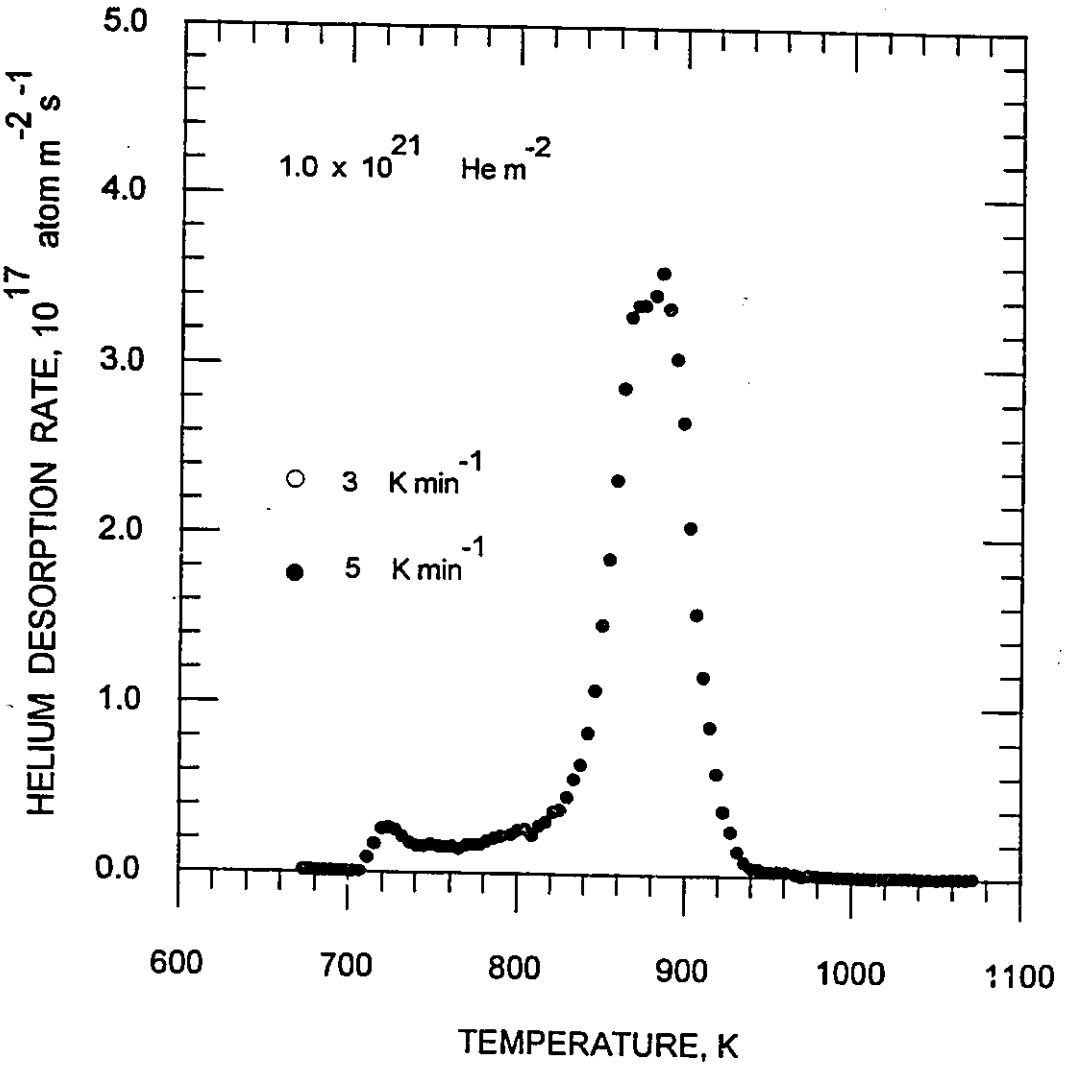

Fig. 5.5. Thermal desorption spectrum for 30 keV helium implanted beryllium to a total fluence of 10^{21} He^+/m^2. The ramping rate is 5 K/min.

desorption regions which in the following discussion are referred to as the "primary" and "secondary" regions, respectively. Up to a fluence of 5×10^{20} He^+/m^2, almost all of the desorption peak lay within the primary desorption region, with a maximum release temperature $T_P > 890$ K and the amount of helium release associated with this peak increased with increasing fluence. However, the population of the primary desorption region decreased significantly at 10^{21} He^+/m^2. The dependence of the primary desorption region population on the implantation fluence is depicted in fig. 5.6. At higher fluences of 7.5×10^{20} and 10^{21} He^+/m^2, another peak was also detected in a secondary desorption region with lower helium population and lower release temperatures ($T_P < 830$ K). Both peaks showed a decrease of their maximum release temperature when the ramping rate was lowered from 5 to 3 K/min. For the intermediate fluences of 2.5×10^{20} and 5×10^{20} He^+/m^2, lowering the ramping rate makes it possible to resolve finer structure in the primary desorption peak.

A common observation for all of the samples investigated was that the absolute amount of helium desorbed showed a strong dependence on the number of trapping sites which is directly proportional to the implantation fluence. The fraction of helium desorbed as a function of the implantation fluence is plotted in fig. 5.7. The average fraction of the helium desorbed increased from $23\pm15\%$ for an implantation fluence of 10^{20} He^+/m^2 to $64\pm9\%$ at a fluence of 7.5×10^{20} He^+/m^2. However, at the highest fluence of 10^{21} He^+/m^2, where the probability of helium trapping at helium-vacancy clusters increased, the fraction of helium released decreased again to less than 30% of the implantation fluence. The low fraction of helium released was also confirmed by the desorption spectra for the

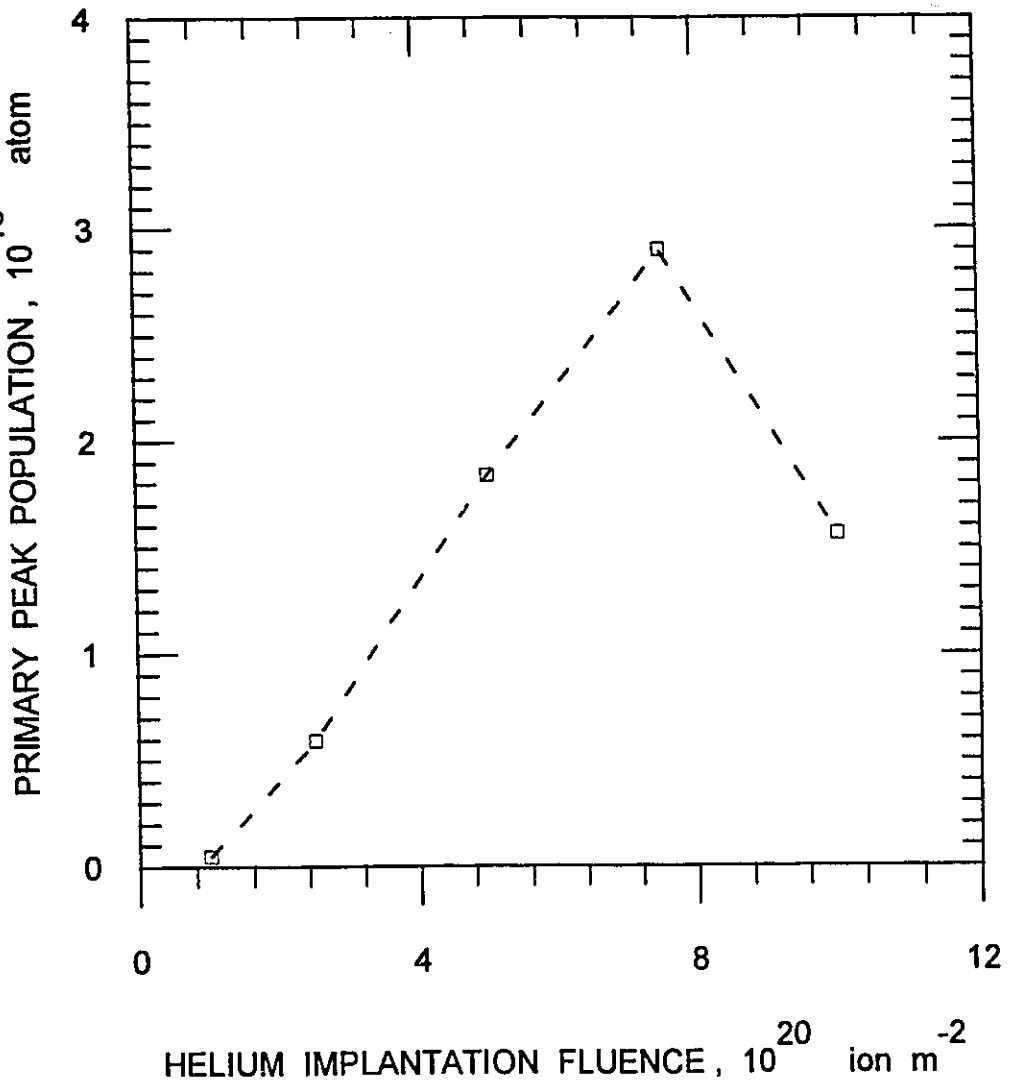

Fig. 5.6. Population of the primary desorption peak as a function of the implantation fluence.

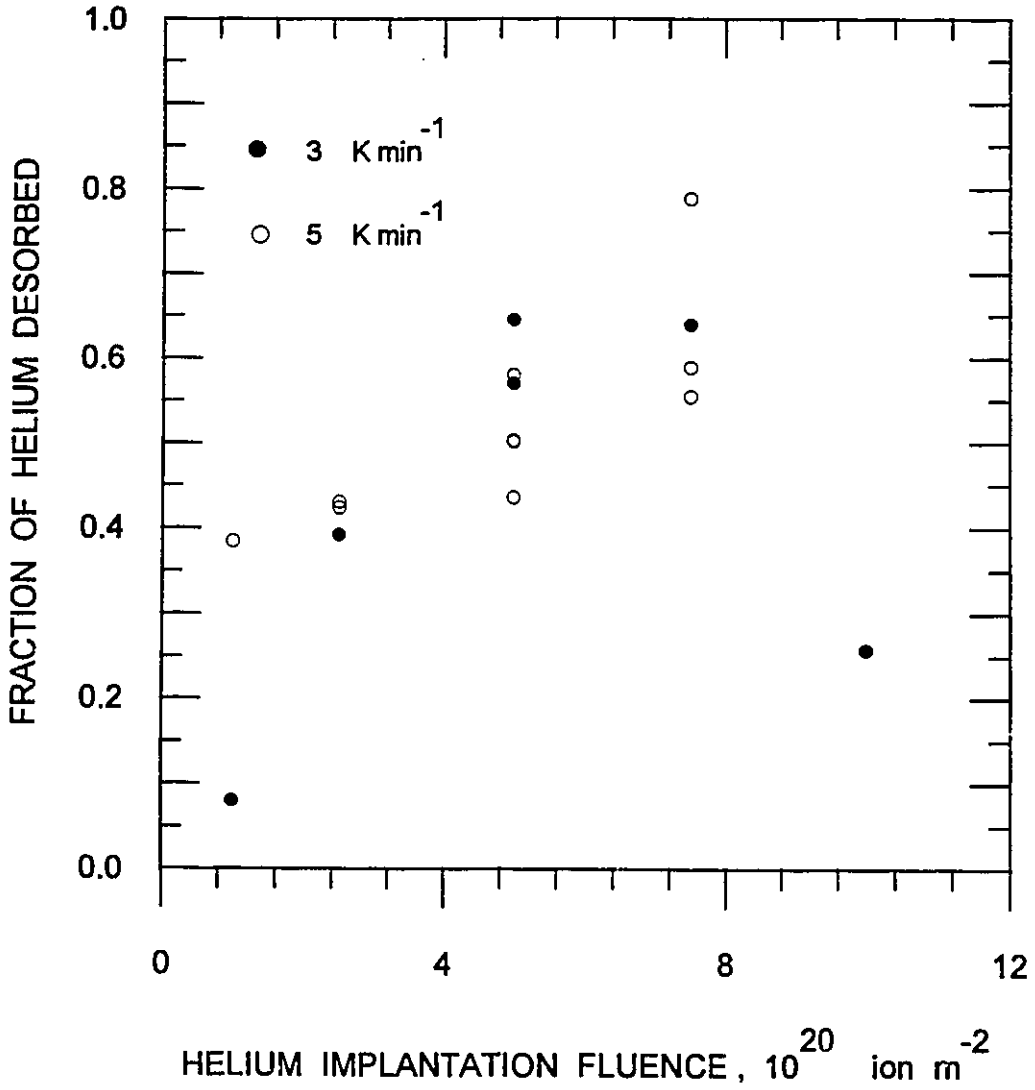

Fig. 5.7. Variation of the fraction of helium desorbed with the implantation fluence.

1.5×10^{19} He^+/m^2 implanted samples. The helium release from these samples was so insignificant (< 1% of the implanted fluence) that it may be concluded that essentially 100% retention was attained up to 1273 K ($\approx 81\%\ T_m$).

The threshold temperature for helium desorption decreases substantially with increasing fluence from 930 K at a fluence of 10^{20} He^+/m^2 to 710 K at 10^{21} He^+/m^2. The decrease in the threshold temperature together with the behaviour of the primary desorption region population indicates that as the fluence increases, the concentration of the primary trapping site increases until it approaches a saturation. At these higher fluences a secondary type of trap, with lower binding energy and therefore earlier release temperature, begins to contribute to the desorption curves.

5.2.2. Analysis of the desorption peaks

The possibility of the helium release being controlled by interstitial diffusion was investigated using the diffusivity expressions determined in 1974 by Bespalov [Dalle Donne *et al.* 1994]

$$D_{He} = 9.9\times10^{-17}\exp\left(\frac{-0.41\,eV}{kT}\right)\ m^2 s^{-1}\ ,\ T < 873K, \quad (5.1a)$$

and

$$D_{He} = 3.1\times10^{-6}\exp\left(\frac{-2.22\,eV}{kT}\right)\ m^2 s^{-1}\ ,\ T \geq 873K. \quad (5.1b)$$

For the temperature interval $873 \leq T\,(K) \leq 1073$, an effective diffusion coefficient, D^{eff} was obtained from

$$D^{eff} = \frac{\int D_{He}\, dT}{\int dT} \quad , \tag{5.2}$$

and the calculated value of 2.4×10^{-17} m^2/s seems to overestimate the amount of desorbed helium. Furthermore, as discussed in section 2.4.4, diffusion-controlled release implies high atomic concentrations of interstitial helium, c_{He}. This, however, does not account for the observed dependence of helium desorption on the implantation fluence. This dependence is expected to result only if the helium atoms reside in HeVCs rather than on interstitial sites.

A more recent diffusion study for low concentrations of implanted helium in beryllium reported the following effective diffusion coefficient below 1073 K [Jung 1993]

$$D_{He} = 2.3 \times 10^{-13} \exp\left(\frac{-0.60\,eV}{kT}\right) \quad m^2 s^{-1} \;,\; T < 1073 K. \tag{5.3}$$

This would result in a diffusion length, $L = (D_{He}\, t)^{1/2}$, of more than 600 nm at 900 K over a time period of two hours; conditions approximately equivalent to a 5 K/min desorption ramp up to 1073 K. This diffusion length is almost twice the projected range of the 30 keV He^+ beam used in the present work. Jung's

release curves indicate three desorption stages. A fraction less than 2% is released below 873 K, followed by a second step with a temperature range of about 1023 to 1423 K, while the major amount of released helium (> 85%) desorbs in a third large step close to the melting point (1560 K). This high retention confirms that the implanted helium is strongly trapped in beryllium. Helium desorption spectra from beryllium should therefore be analyzed under the assumption that helium release is not limited by diffusion in the beryllium bulk and that the temperatures and shapes of the observed peaks give information about the trapping sites in which radiation-produced vacancies are the primary centres.

The desorption curves of figs. 5.1 to 5.5 were examined in terms of the thermal desorption analysis techniques discussed in Chapter 3 to determine the desorption parameters (*i.e.*, the desorption order, energy, attempt frequency and surface coverage dependence). The first attempt was to use an easy and quick procedure, the skewness parameter method (see section 3.2.4), to try to define the possible desorption order associated with the observed peaks. The method, however, appeared to be inappropriate since both the halfwidth and three-quarter width parameters derived from all the reported peaks were out of the ranges defined for both first- and second-order desorption curves. The observed peaks were always too wide and the magnitude of the skewness parameters were always greater than the limits defined in Table 3.1. For example, the primary peak for the 5 K/min desorption curve shown in fig. 5.3 was characterized by $\chi_{1/2}$ and $\chi_{3/4}$ values of -33 and -20, respectively. Although the initial distributions of the implantation do broaden the desorption spectra significantly, compared to a release from an infinite slab, theoretical studies show that this alone cannot

explain the shape of wide desorption curves [Farrell *et al.* 1967]. The frequently very wide curves are most likely to result if more than one value of Q is operative in the metal, possibly even a distribution of energies, and analysis of these cases requires another method of examination.

The second procedure used in analyzing the thermal desorption curves was the peak temperature method (see section 3.2.3). It is clear from figs. 5.1 to 5.5 that the peak temperatures for both the primary and secondary desorption regions depend on the implantation fluence. Figure 5.8 shows that this dependence translates directly to T_P being a function of surface coverage for the primary peak and therefore it could not be ascribed to a first order fixed-energy desorption mechanism. Two possibilities remain, either the desorption is of second order or first order with a variable energy, $Q(\theta)$. The distinction can be made by studying the behaviour of the initial surface coverage, θ_o, as a function of T_P. A plot of $ln(\theta_o\ T_P^2)$ versus $(1/T_P)$ for the primary peak is shown in fig. 5.9. This scattered pattern could not be fit into a linear relationship and this means that the desorption is definitely not of the second order type but rather of first order with a variable energy that depends on the surface coverage. Such a desorption mechanism could not be analyzed by the peak temperature method.

Finally, it seems appropriate to use a complete method to derive the desorption parameters with no pre-assumptions in analyzing the release curves. A lineshape analysis has been conducted on the family of the obtained curves. It is worth mentioning here that this method depends on directly relating the measured surface coverages to the temperatures at which they occur. Since

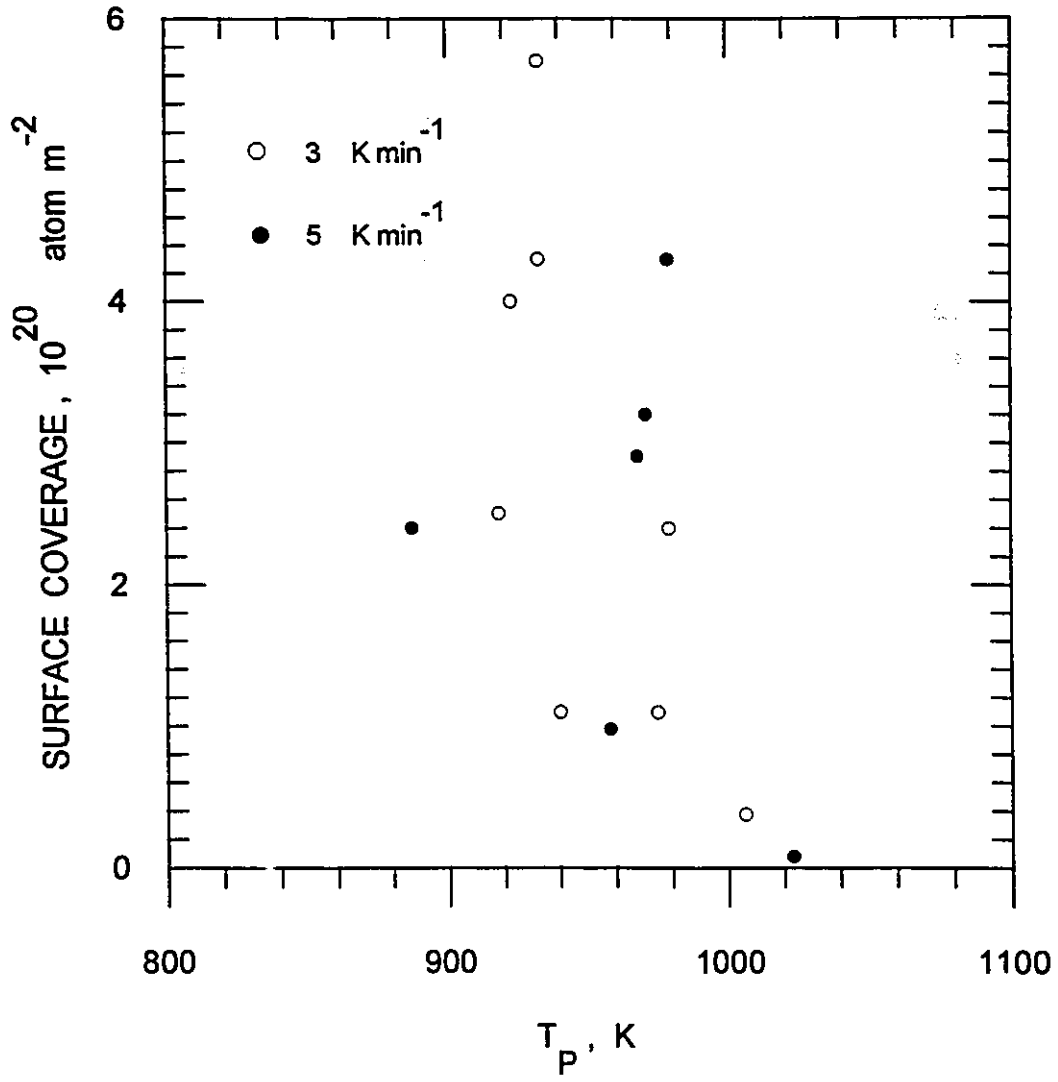

Fig. 5.8. First order desorption analysis of the primary peak by the peak temperature method.

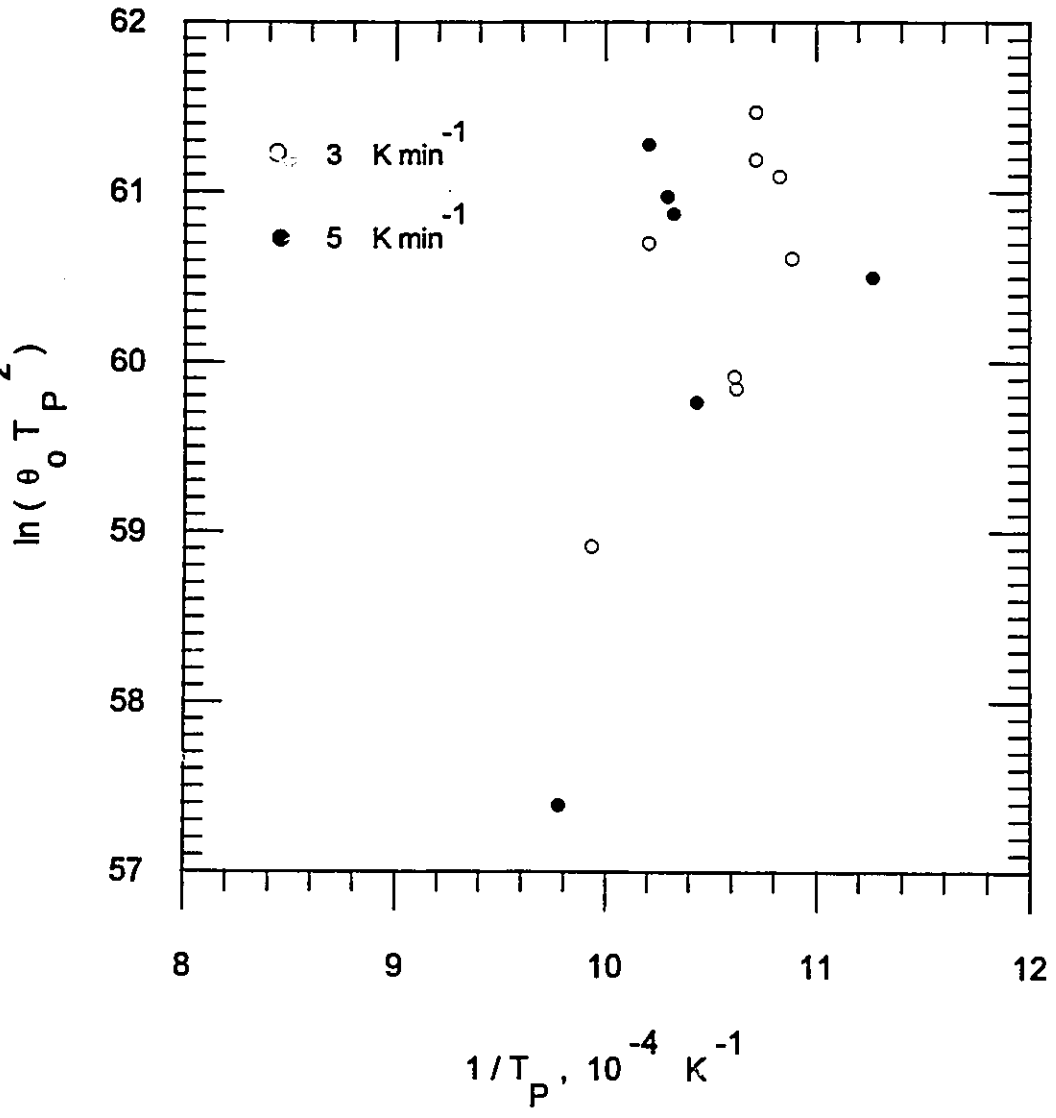

Fig. 5.9. Second order desorption analysis of the primary peak by the peak temperature method.

varying the ramping rate results in shifting the desorption spectrum, only those curves that correspond to a fixed ramping rate were used in the following analysis. The lower ramping rate (3 K/min) has been chosen since it was examined more often and a higher number of spectra exists to make the analysis statistically more accurate.

Five surface coverages were studied according to the procedure described in section 3.2.1. An Arrhenius plot of the variation of the desorption rate with temperature for each of the surface coverages is shown in fig. 5.10. Table 5.1 lists the slopes of a linear representation to each set of data, together with the respective calculated desorption energy and attempt frequency.

Table 5.1
Desorption parameters derived from the lineshape analysis procedure

Surface coverage, θ_t (He/m^2)	$-Q(\theta_t)/k$ (K)	Desorption energy, $Q(\theta_t)$ (eV)	ν (s^{-1})
1.0×10^{20}	- 34923	3.01 ± 0.24	1.0×10^{14}
2.0×10^{20}	- 33078	2.85 ± 0.14	1.0×10^{13}
3.0×10^{20}	- 32129	2.77 ± 0.08	2.5×10^{12}
3.5×10^{20}	- 31939	2.75 ± 0.03	1.6×10^{12}
4.0×10^{20}	- 31607	2.72 ± 0.01	1.0×10^{12}

It is clear from these calculations that the helium desorption energy increases at lower values of θ_t. This is consistent with the observation that the threshold temperature for the helium release increases at lower implantation fluences to the extent that for the 1.5×10^{19} He^+/m^2 implantation complete retention was obtained up to 1273 K. The calculated activation energies are also

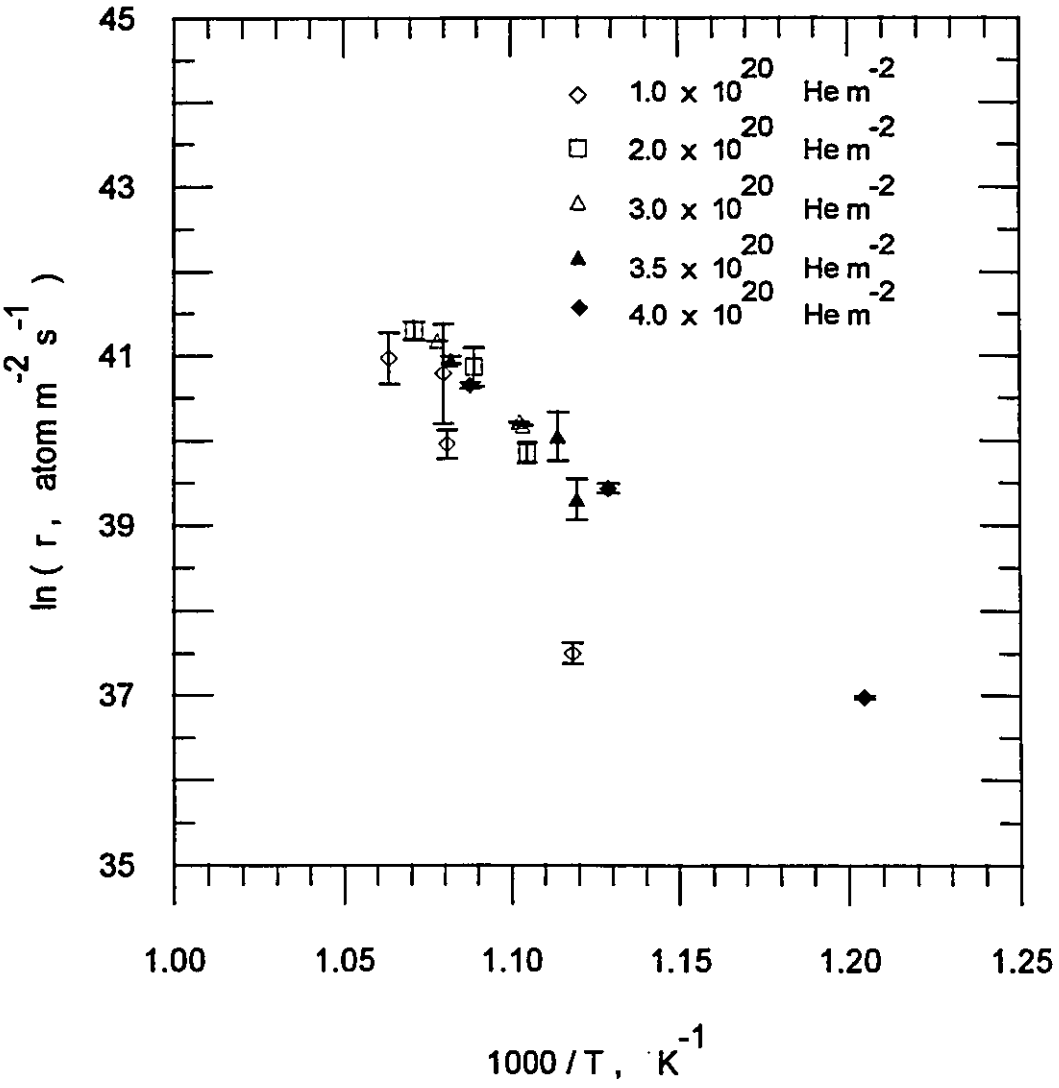

Fig. 5.10. Lineshape analysis of the primary desorption peak. Arrhenius plot of the variation of the desorption rate with temperature for different surface coverages.

much higher than the reported values of 1.71 and 1.63 eV for beryllium self diffusion [Dupouy *et al.* 1966]. Theoretical modelling of helium interatomic potentials and other experimental observations (see Chapter 2) have indicated that such activation energies are usually associated with substitutional detrapping of helium atoms.

As for the nature of the helium traps, two arguments may be made: either (a) there are at least three different trapping sites: two associated with the primary and secondary desorption regions and a third one (or more) with energy (or energies) greater than the upper limit reported in Table 5.1 that does not dissociate until the temperature is much closer to T_m; or (b) each observed value of T_P is related to a He_NV_M trapping site with a different stoichiometry depending on the helium concentration. It is the opinion of this author that the shapes of the desorption curves and their development with fluence favour the former suggestion for the nature of helium traps rather than the latter.

The maximum temperature for the primary desorption peak at a fluence of 10^{21} He^+/m^2 is more than 130 K lower than that at a fluence of 10^{20} He^+/m^2. If these peaks represent two different trapping sites (say; a deeper trap A in the case of the lower fluence and a shallower trap B for the higher one), one would expect that at the higher fluence trap A would be filled first (because it is energetically favourable) and then the excess helium would occupy other sites including site B. If this were the case the resultant spectrum from the 10^{21} He^+/m^2 linear desorption regime should contain both peaks (B followed by A) in the primary desorption region. However, as is evident from all the reported

spectra, the primary desorption region only contains one major peak. This points to the existence of one dissociation process in the primary region (with a variable energy) that contributes to the desorption curve independent of the fluence change. The same argument can be made concerning the secondary desorption peak but there is no available data on the tertiary trapping site to perform this kind of analysis.

The model of different $He_N V_M$ trapping sites formed with higher values of N at higher fluences predicts that during desorption the cluster will possibly dissociate to a different trap, $He_{N-1} V_M$ with the release of one helium atom. This would imply an increase in the relative amount of retained helium at higher fluences, in direct contradiction to the observed behaviour in beryllium between 10^{20} and 7.5×10^{20} He/m^2 (fig. 5.7). Another possibility is that helium detrapping may follow a pattern, similar to that depicted in fig. 2.5, where $i>10$ helium atoms will simultaneousiy dissociate at a certain temperature and a stable $He_{N-i} V_M$ will form. Although this may account for the observed increase in the absolute amount of desorbed helium with fluence, the behaviour of T_P with fluence in this case would be reversed; *i.e.*, at higher fluences where i increases, more stable complexes are expected to form resulting in an increase of the measured value of T_P.

The last column of Table 5.1 contains the attempt frequency as calculated from the y-axis intercepts of fig. 5.10. The intercepts on the Arrhenius plots are equivalent to $ln(\nu)+n\ ln(\theta_t)$ and therefore contain information on the attempt frequency. However, as previously mentioned in Chapter 3, unambiguous

determination of these parameters is only possible if there is a fixed value of ν independent of the surface coverage. Since it was concluded that helium desorption is of the first order, the attempt frequency was varied between 10^{12} and 10^{14} s^{-1}, with $\nu(\theta_t)$ increasing as the value of θ_t decreases. The lower value of 10^{12} s^{-1} results from a least-squares fit of the 4×10^{20} He/m^2 surface coverage data while the upper limit was assumed as the maximum possible value for ν [Redhead 1962].

5.2.3. Desorption dependence on post-implantation ageing

When multiple superimposed peaks were observed for the 3 K/min desorption spectra of the intermediate-fluence implantations (*i.e.*, figs. 5.2 and 5.3) trials were made to reproduce the results. A set of six samples was implanted to a total fluence of 5×10^{20} He^+/m^2. Two of the samples were desorbed with a 5 K/min heating rate at 3 and 16 days after the implantation, respectively, and both produced almost identical spectra with one desorption peak formed around 970 K. Four samples were desorbed with the lower 3 K/min rate at 4, 18, 25 and 37 days. Three of these spectra are shown in fig. 5.11 (the fourth, after 25 days, is the 3 K/min curve on fig. 5.3 and has been left out here for clarity of presentation). The results show a gradual shift of the peak temperature from T_P =980 K to T_P =910 K. Both peaks are in the primary desorption region and the final state of T_P is consistent with the behaviour expected since it is smaller than the 5 K/min value of T_P =968 K.

This instability in the energy associated with the helium trapping sites was

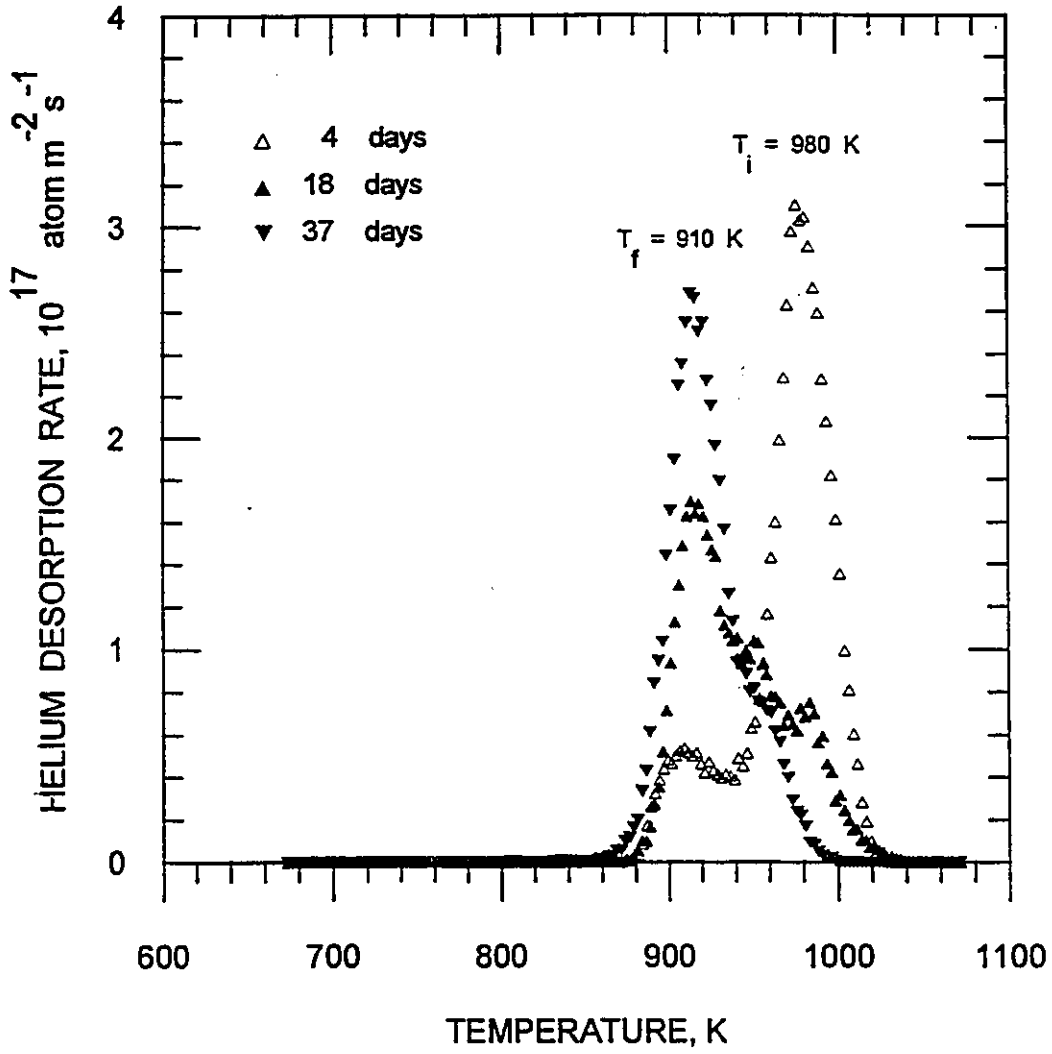

Fig. 5.11. Effect of post-implantation ageing on the desorption spectra of 30 keV He^+ implanted beryllium. The trapped helium seems to be shifting from an initial, T_i, to a final site, T_f. The total implantation fluence is 5×10^{20} m^{-2} and the ramping rate is 3 K/min.

also observed, though to a lesser extent, with the other intermediate fluence of 2.5×10^{20} He^{+}/m^{2}. The observations that the change of the helium detrapping energy is progressive with the time that the sample sits at room temperature before being subjected to thermal desorption and that this behaviour has not been detected at the higher ramping rate may be explained by assuming that the helium atoms are residing in two or more physically adjacent trapping sites with a small energy barrier between them. At room temperature, the helium atoms trapped in these sites are slowly reconfiguring, moving from an initial site characterized by $T_P = T_i$ to a final state, $T_P = T_f$. This reconfiguration is possibly taking place by defect migration and/or some association/dissociation mechanism between two simple HeV trapping sites. Any of these processes should be restricted by the energy barrier between these two sites, which has been estimated to be $\approx 0.18 \pm 0.02$ eV.

During desorption, the ramping rate clearly affects the helium dissociation process from these trapping sites. The 3 K/min rate seems to give enough time for the helium atoms to dissociate independently from the two sites while the higher rate does not allow for the detection of this process. The obtained results also indicate that the early stage of desorption, $T < 800$ K, does not affect the helium configuration attained at the end of the room temperature ageing period. This is possible only if the height of the energy barrier between the two trapping sites increases at higher temperatures so as to hinder the movement of the trapped helium atoms. If such increase happens at a greater rate than the thermal energy, kT, the trapped helium will "freeze" at their respective sites until the temperature at which the trap dissociates and the helium atoms become freely mobile.

Further investigation of the ageing effect has been carried out by implanting a set of samples to a total fluence of 2.5×10^{20} He^{+}/m^{2} and then allow them to age under liquid nitrogen instead of at room temperature. The aim was to impede the movement of the implanted helium atoms over the ageing period and see whether this would help in producing identical spectra irrespective of the sample age. Three samples were desorbed after 9, 27 and 35 days and the obtained curves are displayed in fig. 5.12. The most obvious observation is that the release curves show that a change is occurring even at 77 K. Two traps seem to be formed with two distinct values of T_P . These values are affected by the ageing process, with the low temperature trap shifting to lower values of T_P and the higher temperature one moving to a higher T_P. A study of the properties of point defects in beryllium observed Stage I annealing as the only recovery stage below 80 K [DeLaplace *et al.* 1968]. The recovery processes at this temperature are presumably due to thermal recovery of correlated close pairs as well as self-interstitial migration. The driving force for the observed changes in fig. 5.12 seems to be the high chemical potential in the highly damaged implant region and its high helium concentration ($\approx$1.9 at% at the peak).

Desorption occurs at relatively higher temperatures compared to the samples that were allowed to age at room temperature (fig. 5.2) which implies the formation of a more stable type of trapping and an interesting observation is that the three samples released almost exactly the same amount of helium ($\approx$74.5% of the implanted fluence). The most probable cause for this behaviour seems to be that the trapped helium atoms have agglomerated into larger clusters or microbubbles that, upon dissociation, released a larger fraction of the implanted

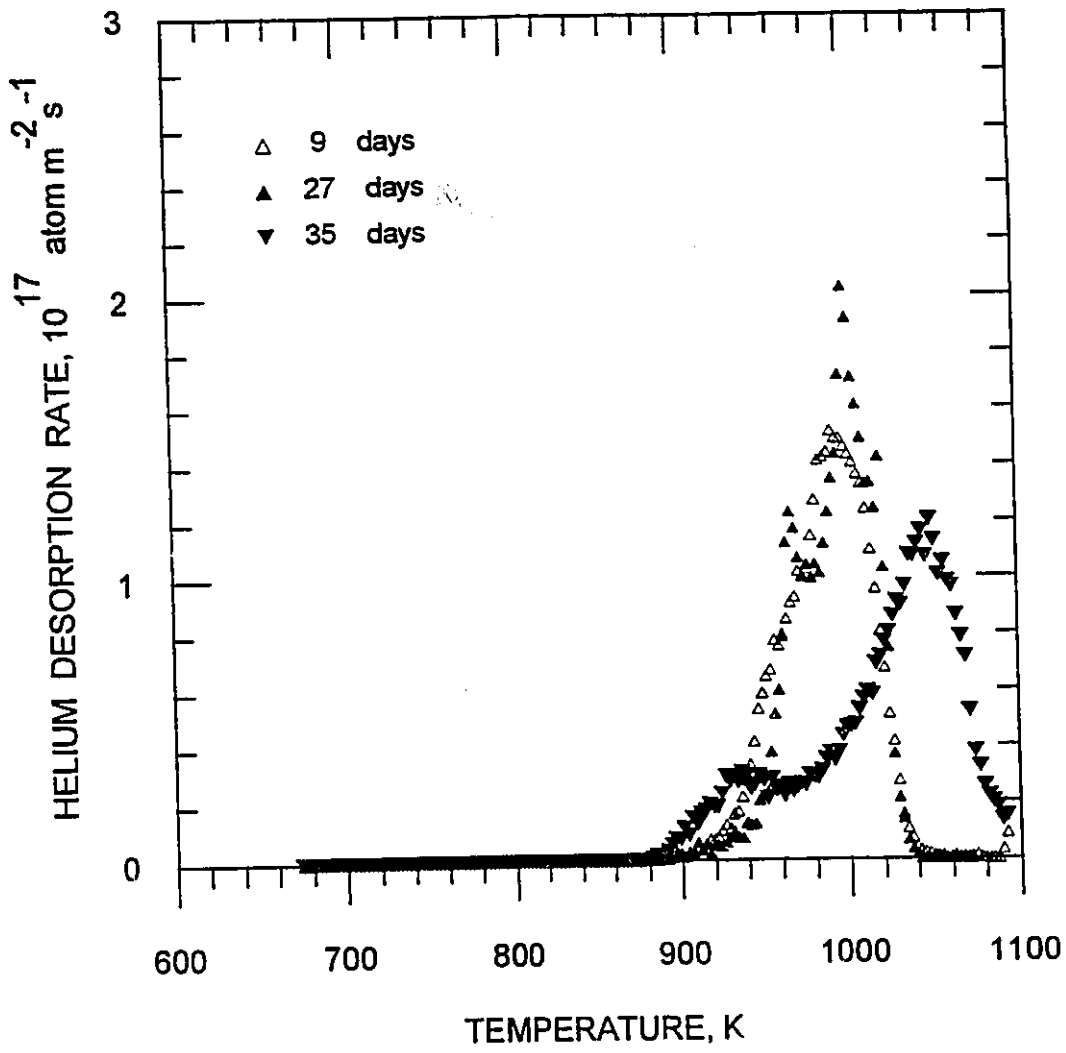

Fig. 5.12. Thermal desorption spectra of 30 keV He^+ implanted beryllium. Samples were allowed to age for the designated periods at liquid nitrogen temperature. The total implantation fluence is 2.5×10^{20} m^{-2} and the ramping rate is 3 K/min.

helium. Such agglomeration becomes more relevant at liquid nitrogen temperatures since the trapped helium is expected then to be highly immobilized in the implant region; enhancing the probability of helium-helium interactions.

5.2.4. Surface damage caused by helium desorption

Scanning electron microscopy examination of the beryllium surface morphology before and after desorption provides a sharp contrast between the implanted and the non-implanted regions. Figure 5.13 shows a typical image of an implanted beryllium surface before desorption. The darker shade reflects the part of the surface which was implanted while the lighter side results from the part of the surface under the holding clamp, *i.e.*, not implanted. No surface damage is observed after the implantation, nor was it possible to detect the existence of the grain boundaries. The difference in the shades is due to different electron reflectivities, probably due to carbon deposition on the implanted part of the surface, a common occurrence in diffusion-pumped implanters.

As can be seen in figs. 5.14 to 5.17, after desorption the implanted region is characterized by an increase in surface roughness due to the formation of irregular shaped blisters and flakes. The grain boundaries are clearly visible only where desorption took place, showing an estimated grain size of $\approx$ 21 μm. The blisters are observed to be randomly distributed across the surface and do not appear to be associated with the grain boundaries. It is notable that for the samples aged under liquid nitrogen (fig. 5.17) where the helium release was inferred to be the result of microbubbles burst, dome-shaped blisters are more

Fig. 5.13. Typical SEM micrograph of a beryllium surface implanted with 30 keV helium ions. The lighter shade marks the unimplanted part of the surface.

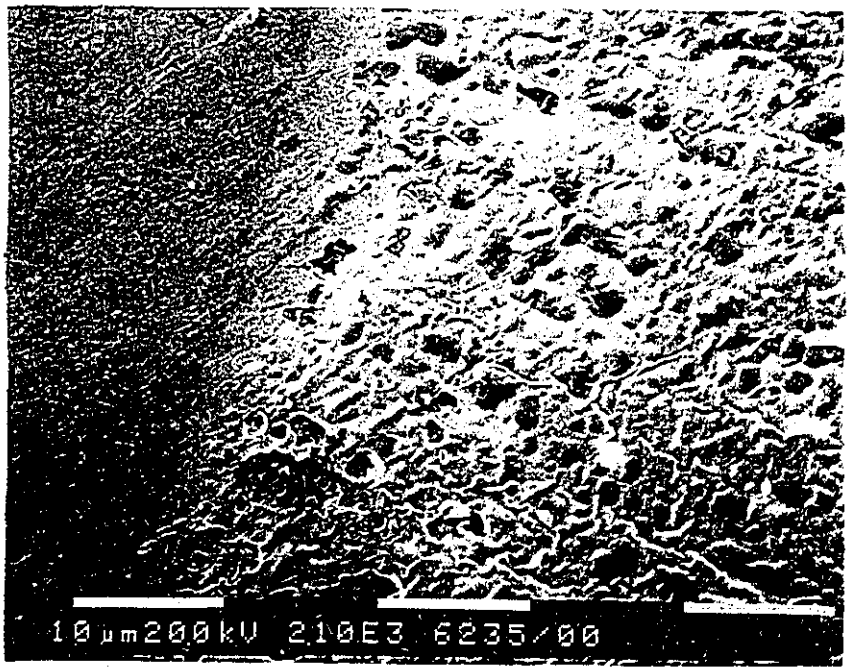

Fig. 5.14. SEM micrograph of a beryllium surface heated up to 1073 K after 2.5×10^{20} He/m^2 implantation at room temperature.

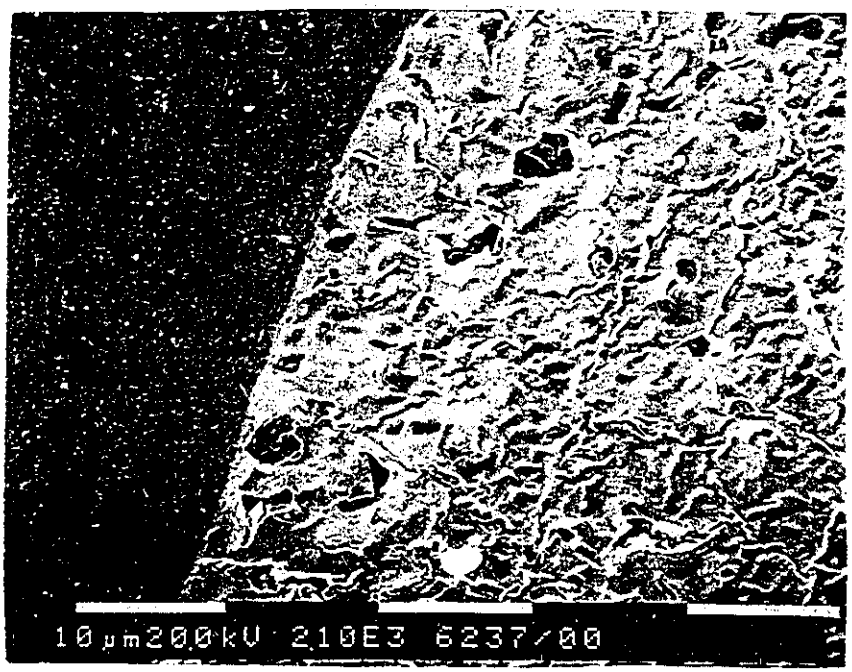

Fig. 5.15. SEM micrograph of a beryllium surface heated up to 1073 K after 5.0×10^{20} He/m^2 implantation at room temperature.

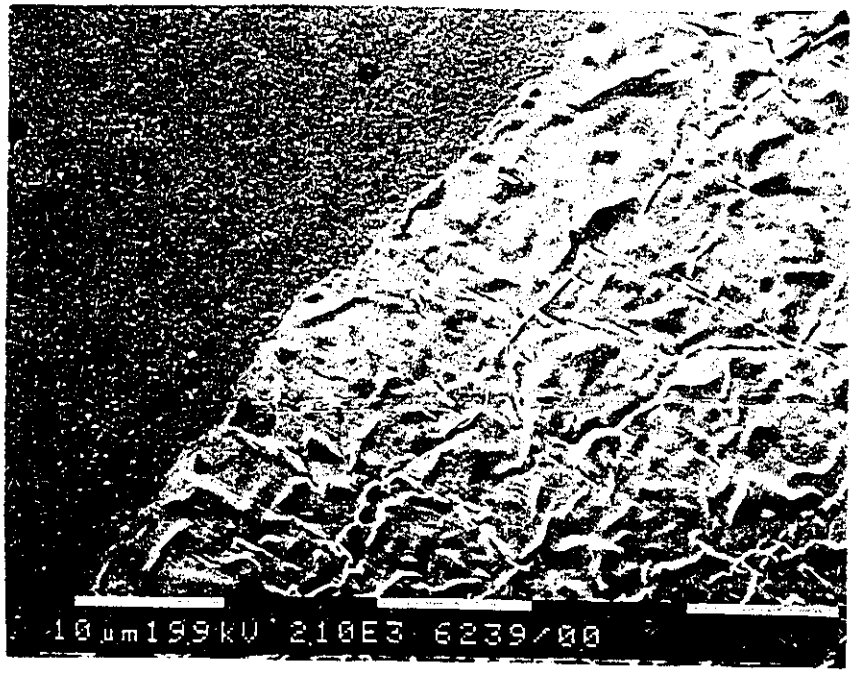

Fig. 5.16. SEM micrograph of a beryllium surface heated up to 1073 K after 7.5×10^{20} He/m^2 implantation at room temperature.

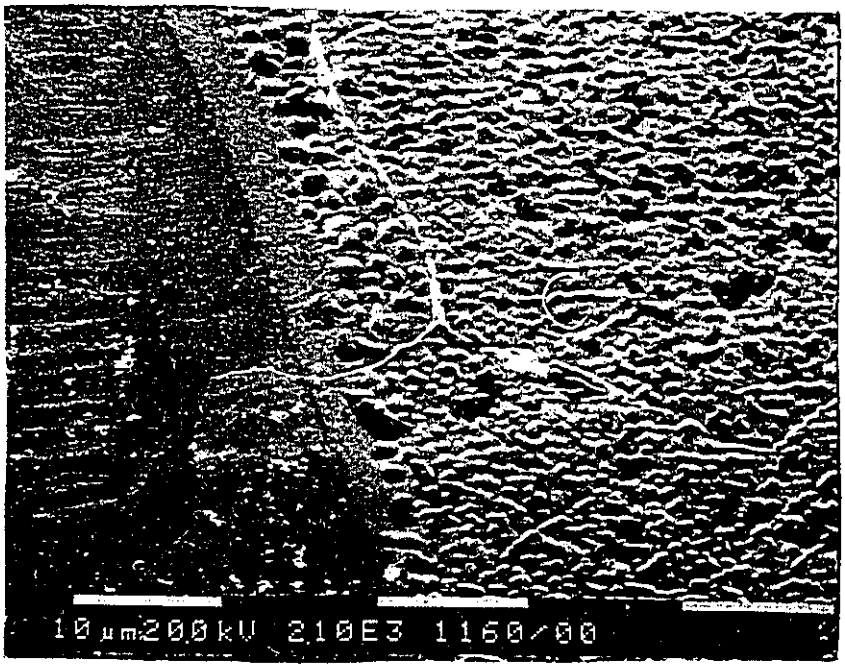

Fig. 5.17. SEM micrograph of a beryllium surface heated up to 1073 K after 2.5×10^{20} He/m^2 implantation at room temperature. After implantation, the sample was allowed to age at liquid nitrogen temperature.

frequently observed. Also significant is the observation that raising the implantation fluence from 2.5×10^{20} to 7.5×10^{20} has not resulted in any apparent variation in the desorbed surface features. This indicates that the same mechanism is controlling the helium release for the three fluences. The reverse in the shades between the implanted and unimplanted regions is possibly due to the oxidation of the surface carbon film during desorption although Rutherford backscattering analysis of the desorbed surfaces show no significant oxidation growth during the desorption cycle.

5.3. Step - annealing desorption

5.3.1. Experimental observations

The microstructural evolution of the precipitated helium in beryllium samples was studied by a step-annealing desorption procedure. Samples implanted at room temperature to a total fluence of 2.5×10^{20} He^+/m^2 were rapidly heated at 20 K/min to an elevated temperature where they were kept for two hours before a slower heating at 3 or 5 K/min was carried out up to 0.75 T_m. Two isotherms were investigated: 573 and 773 K. Both were below the lowest measured temperature for any significant helium release when the 2.5×10^{20} He/m^2 samples were thermally ramped without an anneal stage. The purpose was to investigate the mobility of the helium atoms before desorption by allowing the trapped helium to rearrange over the two-hour period.

Small HeVCs were shown to be mobile in beryllium at 500 K by neutron depth profile experiments [Eleveld *et al.* 1994a]. The absence of helium release up to $T>673$ K is a good indication that this process is not a significant mechanism for helium release, therefore the 573 K annealing temperature was chosen to enable short-range rearrangements of the trapped helium. The higher annealing temperature of 773 K was selected to increase the thermal vacancy concentration that has been recently reported as a possible mechanism for helium bubble growth in beryllium [Sannen *et al.* 1995]. The vacancy formation energy in beryllium was estimated at 1.11 eV [Igarashi *et al.* 1991]. This means that the thermal vacancy atomic concentration of 5.8×10^{-8} at 773 K is more than 11 orders of magnitude above the concentration at room temperature.

The desorption spectra obtained are shown in figs. 5.18 and 5.19. They indicate the formation of one well defined peak with a population and peak temperature that depends on the desorption regime. Compared to fig. 5.2, it can be seen that T_P for the step-annealed samples is considerably higher than that for the samples that were directly desorbed. The same can be said about the threshold temperature for helium release. The effect of the ramping rate on T_P however was similar to the expected behaviour, *i.e.*, lower value of T_P at lower ramping rates. This is a clear indication that the two-hour annealing period has transferred the trapped helium into a more stable configuration characterized by higher dissociation energies.

Inspection of the desorbed surfaces by SEM reveals the formation of helium blisters and holes on the surface area where desorption took place. The

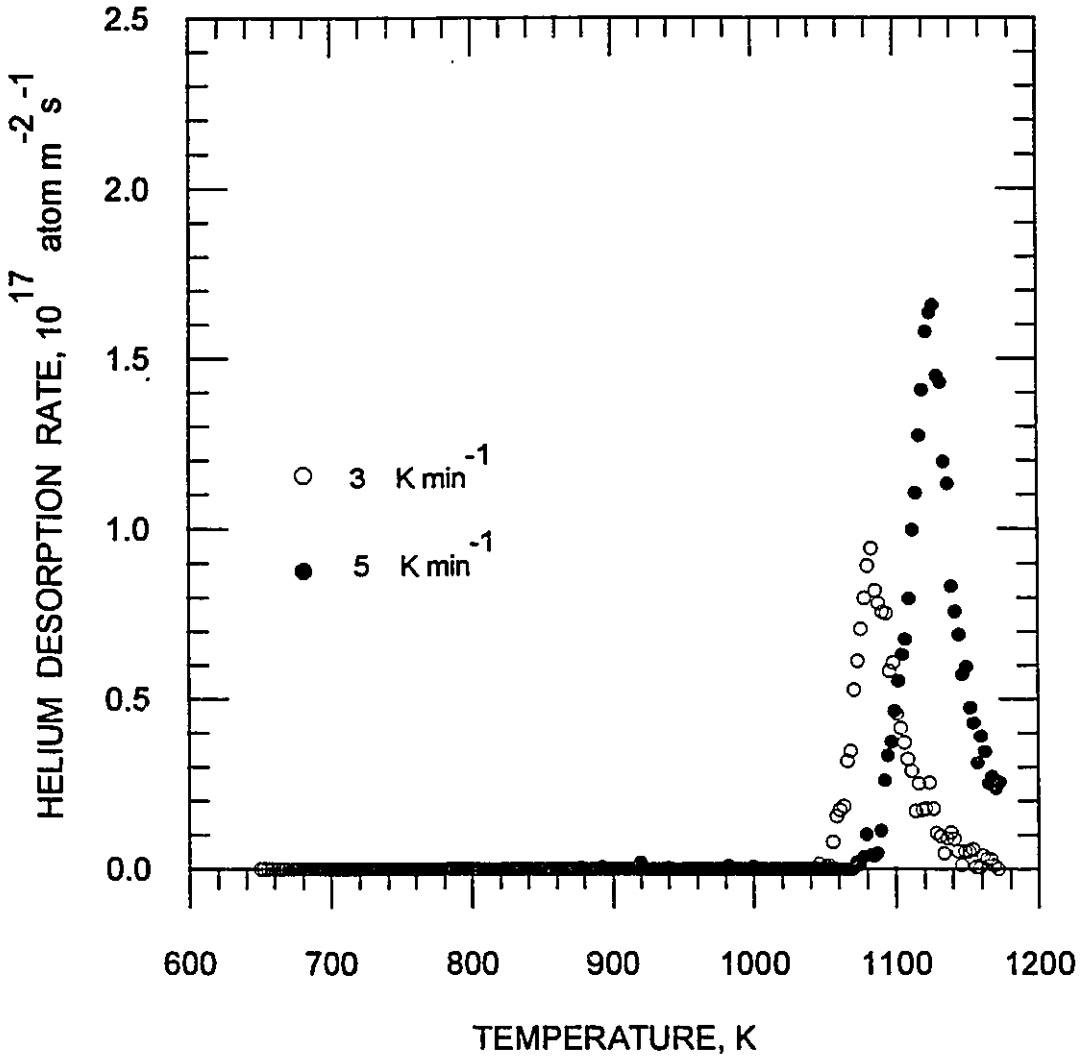

Fig. 5.18. Thermal desorption spectra for 30 keV helium implanted beryllium to a total fluence of 2.5×10^{20} He^{+}/m^{2}. During desorption, samples were kept for 2 hours at 573 K.

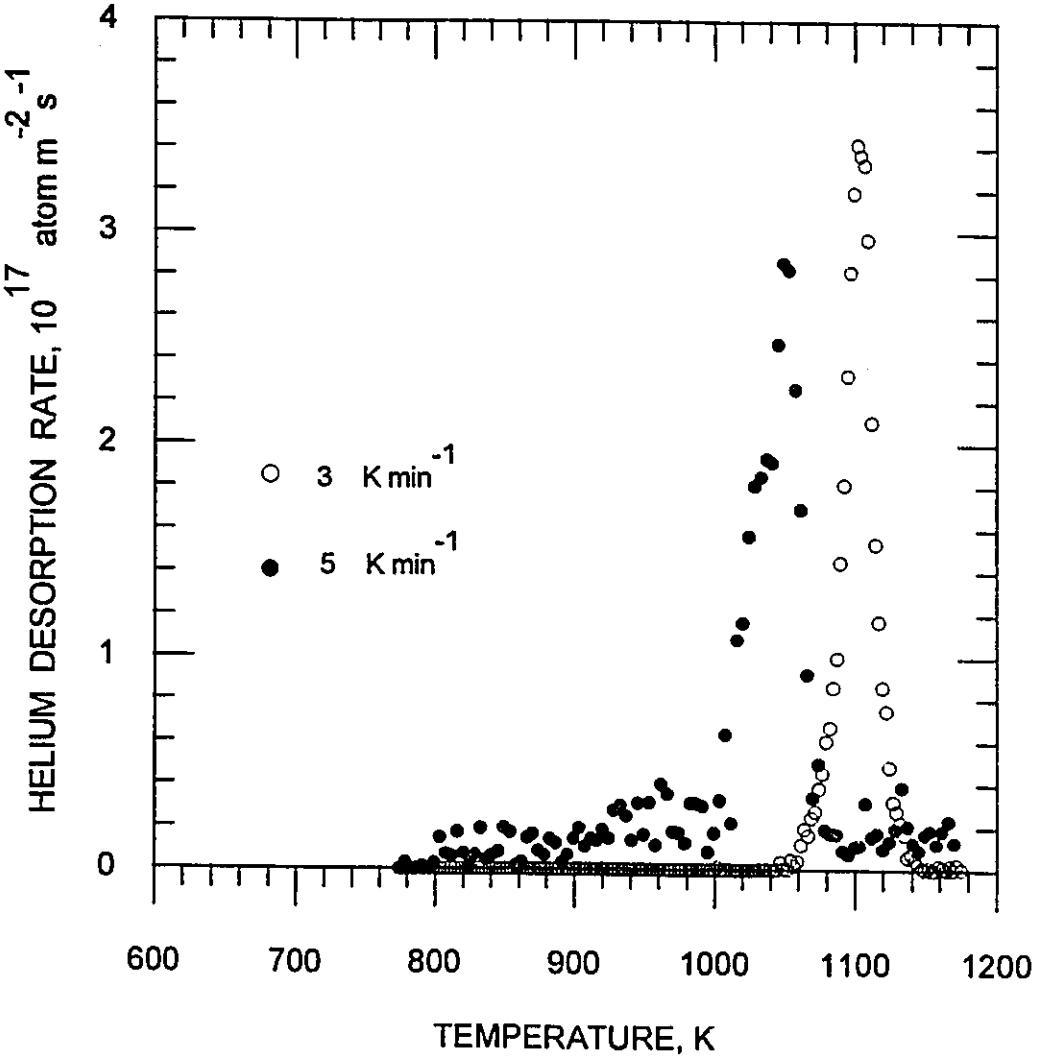

Fig. 5.19. Thermal desorption spectra for 30 keV helium implanted beryllium to a total fluence of 2.5×10^{20} He^+/m^2. During desorption, samples were kept for 2 hours at 773 K.

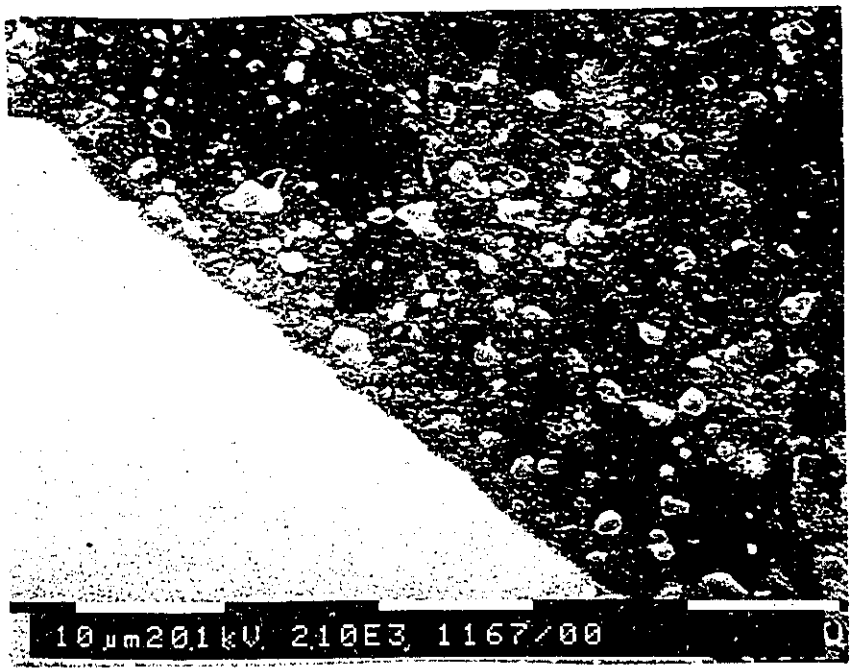

Fig. 5.20. SEM micrograph of a beryllium surface annealed at 573 K for 2 hours before being heated up to 1173 K. The sample was implanted with 2.5×10^{20} 30 keV He/m^2 at room temperature.

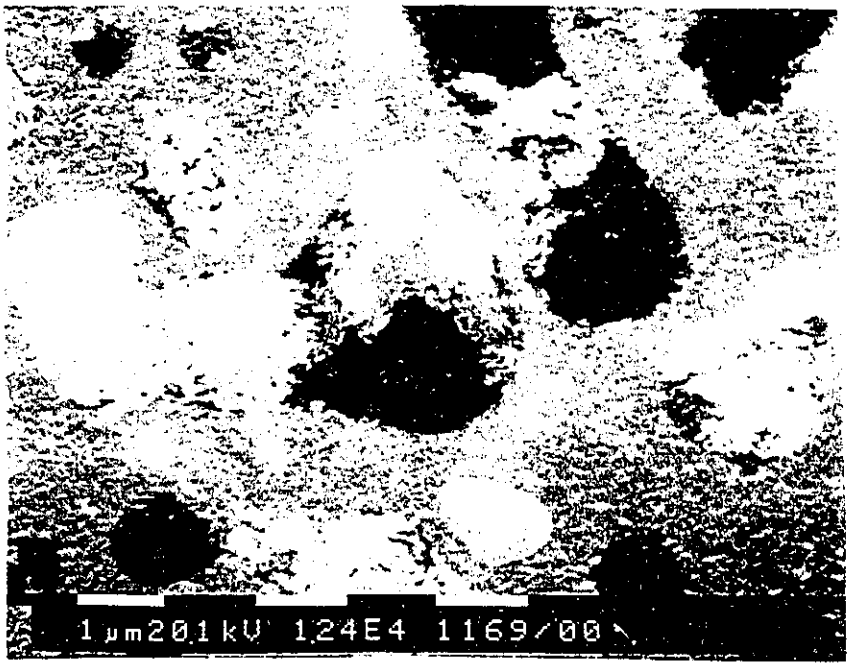

(a)

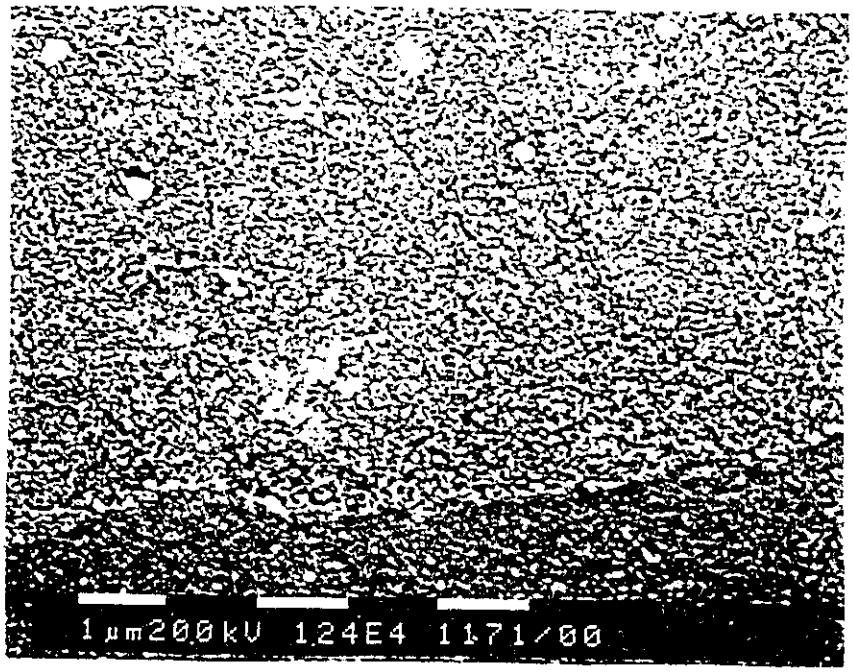

(b)

Fig. 5.21. SEM micrographs with higher magnifications of the same sample as in fig. 5.20: (a) implanted area; (b) unimplanted area.

Fig. 5.22. SEM micrograph of a beryllium surface annealed at 773 K for 2 hours before being heated up to 1173 K. The sample was implanted with 2.5×10^{20} 30 keV He/m^2 at room temperature.

(a)

(b)

Fig. 5.23. SEM micrographs with higher magnifications of the same sample as in fig. 5.22: (a) implanted area; (b) unimplanted area.

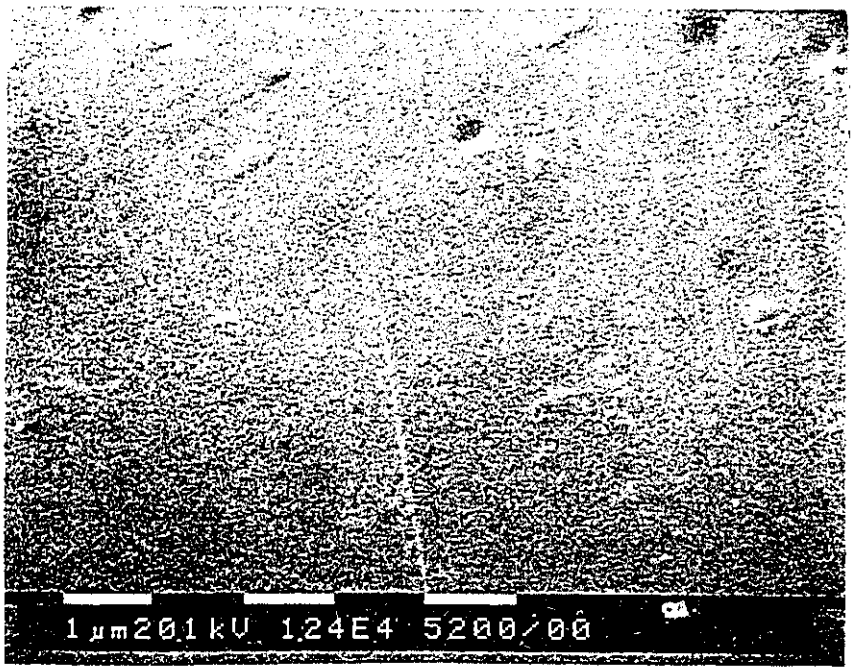

Fig. 5.24. SEM micrograph of a beryllium surface annealed at 773 K for 2 hours and then rapidly cooled to room temperature. The sample was previously implanted with 2.5×10^{20} 30 keV He/m^2 at room temperature. No helium desorption was detected during the desorption regime.

samples that were annealed at 573 K are shown in figs. 5.20 and 5.21. Holes formed randomly across the desorbed surface with sizes ranging between 0.4 and 4.5 μm. Smaller holes appear to overlap more frequently which may indicate that the larger-size holes have resulted from interconnections between small bubbles. Similar to the directly ramped samples, there is a sharp contrast between the implanted and unimplanted surfaces. The border region is clearly defined and even at higher magnification, the unimplanted surface looks completely unaffected by the helium release. It can be seen that a significant fraction of the blister lids were still attached to the surface and this occurs more frequently for the smaller bubbles. Although this does not necessarily indicate that helium is still retained behind these caps, it is worth noting that the images shown are for the 5 K/min sample which was still desorbing at 1173 K, as can be seen from fig. 5.18.

Figures 5.22 and 5.23 show the surfaces of the samples that were annealed at 773 K before being desorbed. The features are much larger than those observed for the lower annealing temperature and wide craters are formed on the desorbed areas as a result of the surface skin being blown off during the helium release. The formed holes are generally interconnected and they have an elliptical extended shape rather than the spherical domes observed in fig. 5.20. The different shades observed below the borders of the elongated holes are consistent with the construction of faceted bubbles. Such formation, as previously discussed in Chapter 2, would imply that the formed agglomerates of the implanted helium are highly immobile. The only similarity in the two surfaces shown in figs. 5.20 and 5.22 lies in that the unimplanted surface (appears in the lower right corner of fig. 5.22) remained intact after desorption.

Figure 5.24 shows a surface of a sample that was implanted at room temperature to 2.5×10^{20} He^{+}/m^{2}, ramped quickly up to 773 K where it was kept for two hours and then rapidly cooled down to room temperature. The sample surface has been studied by SEM in order to detect any early formation of the surface features observed after desorption. As is clear from the figure, no surface morphology changes occurred during the ramp up and anneal stages and this indicates that the observed surface deformations are directly linked to the helium release process. Another observation was the detection of a thick non-reflective layer deposited on this surface. An X-ray analysis for the surface composition showed a strong oxygen signal implying that even at the high vacuum conditions maintained in the desorption chamber, there were sufficient oxidants to increase the thickness of the surface oxide layer substantially.

Comparing the results from the step-annealing desorption procedure to those from the direct ramping experiments shows a clear transition of the trapping mechanism for the implanted helium from small HeVCs to bubbles. This explains the increase in the trapping energy, as implied by the higher desorption temperature, for the samples desorbed by the step-annealing regime. However, the mechanism by which these bubbles nucleate and grow can not be directly deduced from either the desorption curves or the SEM images. It is obvious that the change has happened during the anneal period and two possibilities have been investigated as controlling processes: (a) helium bubble growth by the absorption of thermal vacancies; and/or (b) migration and coalescence of HeVCs formed during the implantation.

5.3.2. Helium bubble growth by the absorption of thermal vacancies

In a recent study of the annealing-produced helium swelling in neutron-irradiated beryllium, samples were annealed at different temperatures in the range 473 to 1073 K for periods of 1 and 24 hours [Sannen *et al.* 1995]. Density measurements made after annealing showed much more swelling than after irradiation only. For helium concentrations up to 2.1 at%, no helium release was observed at annealing temperatures $\leq$673 K. However, samples with as low as 0.38 at% helium had $\approx$70% loss of their helium content after 24 hours annealing at 1073 K. Sannen *et al.* proposed that at elevated temperatures, beryllium self-diffusion allows bubbles to grow by absorption of thermal vacancies, and that this mechanism is the one responsible for the helium release. The following is a numerical calculation that was performed for helium bubble growth in beryllium at increasing temperatures in order to determine whether this mechanism can account for the helium desorption reported in the present study.

The growth rate of small helium bubbles by vacancy absorption is, to a first approximation, proportional to the vacancy atomic concentration, c_V, and the vacancy diffusion coefficient, D_V. The value of $c_V D_V$ is equal to the self-diffusion coefficient. Since the helium release process in question occurred around 0.7 T_m, the thermal vacancy concentration ($\approx 7.5\times10^{-6}$) dominates the concentration of the surviving radiation-produced vacancies since most of the radiation damage produced during the implantation annihilates promptly by the simultaneously produced SIAs. In this model, only the thermal vacancy contribution was considered.

By solving the steady-state diffusion equation for the thermal vacancy concentration outside a bubble, the bubble radius growth rate can be written as [Greenwood *et al.* 1959]

$$\frac{dR}{dt} = (D_s/R)\,[1-\exp\{-(P-2\gamma/R)\,\Omega/(kT)\}] \quad , \quad (5.4)$$

where D_s is the self-diffusion coefficient, P is the helium pressure, γ is the surface energy and Ω is the atomic volume. The helium pressure was calculated from the empirical equation derived in 1980 by Mills, Liebenberg and Bronson (MLB) [Mills *et al.* 1980]. A critical review of the different helium equations of state (EOS) judged the MLB equation as "the most accurate and convenient helium EOS" for studying the formation of helium bubbles in implanted metals [Donnelly 1983]. The MLB formulation states that a helium bubble molar volume, v, in cm^3 is related to the pressure in kilobars and the absolute temperature by

$$v = (22.575 + 0.0064655\,T - 7.2645\,T^{-1/2})\,P^{-1/3} + (-12.483 - 0.024549\,T)\,P^{-2/3}$$

$$+ (1.0596 + 0.10604\,T - 19.641\,T^{-1/2} + 189.84\,T^{-1})\,P^{-1} \,. \quad (5.5)$$

The calculation of the change in the radius of a helium bubble was done using eqs. (5.4) and (5.5) at the different desorption regimes investigated in the present work. Values of the parameters used in this calculation are listed in

Table 5.2. The bubble radii calculated are plotted in figs. 5.25 and 5.26 for the 3 and 5 K/min desorption rates, respectively.

Table 5.2
Values of the physical parameters used in the thermal vacancy absorption model

Physical property	Value
Self-diffusion activation energy (eV) [a]	1.63
Pre-exponential factor (m^2/s) [a]	5.2×10^{-5}
Atomic volume (m^3)	8.2×10^{-30}
Surface energy (J/m^2) [b]	3.13024, $T<780$ K
	$1.96+0.0015(T_m-T)$, $T<1560$ K
Melting temperature (K)	1560

[a] Dupouy *et al.* (1966).
[b] Dalle Donne *et al.* (1994).

It is obvious from these figures that there is no substantial increase in the helium bubble radius during the 2 hour annealing period. On the contrary, the annealing stage seems to generally delay the helium bubble growth in three of the four cases; a totally unexpected behaviour if the vacancy absorption mechanism is the rate-determining process. Also, the estimated radii for the bubbles are not consistent with the SEM results (*e.g.*, $R\approx30$ μm from fig. 5.25 compared to a measured value < 5 μm), although the observed increase in bubble dimensions with the annealing temperature has been successfully predicted. Based on these observations, it was concluded that the helium bubble growth by thermal vacancy absorption is not sufficient by itself to account for the reported results.

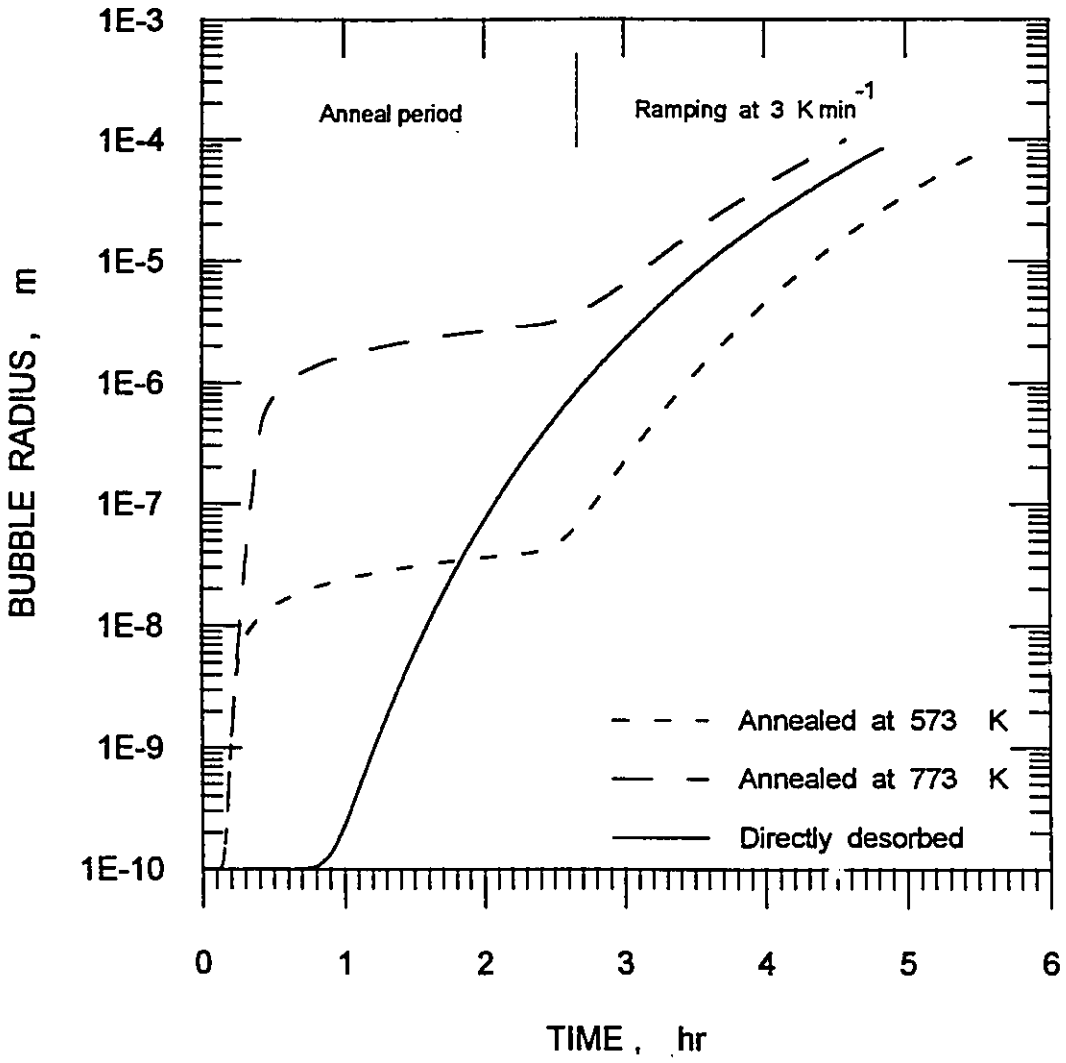

Fig. 5.25. Numerical estimates for the helium bubble radius in beryllium as a function of the annealing time for three different desorption regimes. The ramping rate is 3 K/min for the directly desorbed curve and for the step-annealed curves after the 2 hours isothermal period.

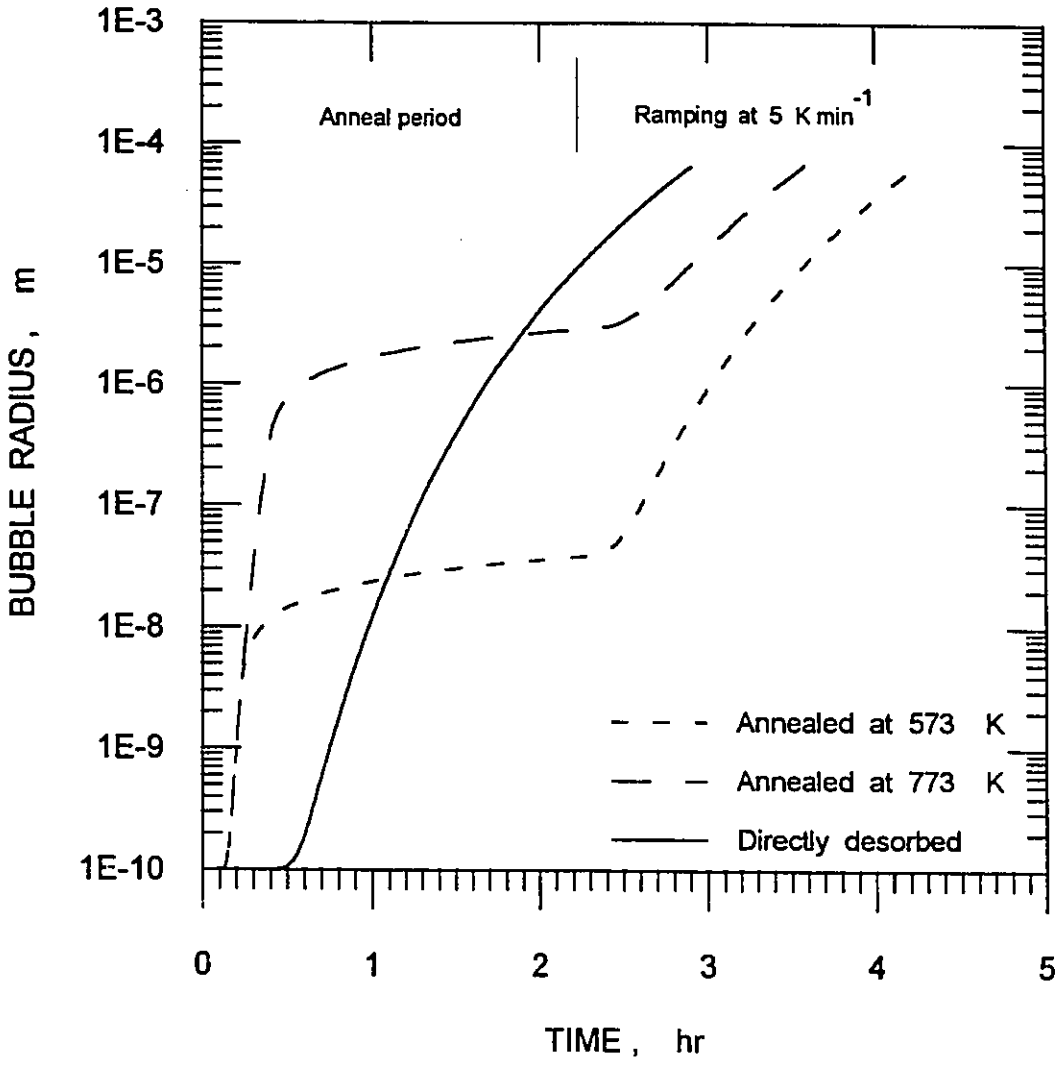

Fig. 5.26. Numerical estimates for the helium bubble radius in beryllium as a function of the annealing time for three different desorption regimes. The ramping rate is 5 K/min for the directly desorbed curve and for the step-annealed curves after the 2 hours isothermal period.

5.3.3. Migration and coalescence of trapped helium clusters

The regions where implanted helium atoms first nucleate as gas bubbles are those that act as vacancy sources in the material. In early experimental observations, it was found that free surfaces and grain boundaries can act as both sources and conductors of vacancies while line defects (*e.g.*, dislocations) may conduct but not produce vacancies [Barnes 1960]. In the present study, the boundary between the beryllium bulk and the surface oxide film was considered as the most probable vacancy source for helium bubble growth since the implantation mean range, r_{av} , of 0.32 ± 0.05 μm provides a much shorter diffusion length compared to the measured average grain size of 19.5 ± 1.5 μm.

A study of the diffusion and precipitation of helium in BeO resulted in the following relation for the helium diffusion coefficient [Gmelin 1971]

$$D = 2.5 \times 10^{-7} \exp\left(\frac{-3.45\,eV}{kT}\right) \quad m^2/s\,, \tag{5.6}$$

The same study reported that helium bubble nucleation in BeO begins at 870 K and peaks around 1470 K, which means that when helium defects are relatively mobile in a beryllium substrate, a surface layer of BeO can serve as an effective permeation barrier that hinders the helium release from the bulk material.

Under the assumption that helium desorption is controlled by the nucleation of gas bubbles at the bulk-oxide interface and that migration of the

trapped helium is governed by beryllium self-diffusion, the diffusion length for the two-hour annealing period can be estimated as a function of temperature. Using the beryllium self diffusion equation [Peterson 1978]

$$D = 5.2 \times 10^{-5} \exp\left(\frac{-1.63\,eV}{kT}\right) \quad m^2 s^{-1}, \tag{5.7}$$

the diffusion time for helium to migrate over the distance r_{av} as a function of the annealing temperature has been calculated and is summarized in Table 5.3.

Table 5.3
Be self-diffusion data for a diffusion length of r_{av}, the implantation mean range

Annealing temperature (K)	Diffusion time (s)
300	4.61×10^{18}
473	4.45×10^{8}
573	4.15×10^{5}
773	80.97
873	4.91
1073	0.09

These results indicate that annealing at 573 K for two hours would not be enough for significant amounts of the trapped helium to diffuse to the interface. However, such migration accelerates rapidly at 773 K and should result in substantial deposition of helium at the Be/BeO interface. In both cases, helium atoms that do not dissociate from their traps before 1073 K would spontaneously

migrate to the nearest interface. This would justify the relative increase in the average amount of desorbed helium from $\approx 30\%$ for the samples annealed at 573 K to $\approx 75\%$ for those annealed at 773 K. The delayed release at the lower annealing temperature can also be explained as due to the agglomeration of smaller, relatively immobile bubble nuclei that would require longer time periods to grow to reach the surface. The formation of these nuclei is evident from the absence of the desorption peaks previously observed when the samples were directly ramped from room temperature (figs. 5.1 to 5.5).

For the samples annealed at 773 K this growth period was much shorter, as can be seen from fig. 5.19. Raising the temperature above 773 K provided the driving force that initiated some helium release shortly after the isothermal stage for the 5 K/min sample, with a major release peak around 1050 K. The fact that no helium release was detected during the isothermal annealing implies that while the agglomerates were mobile, helium remains strongly bound. Hence the helium release is controlled by a detrapping mechanism. For the 3 K/min annealed sample, the observed behaviour is, to some extent, anomalous. Not only did the sample display a high retention level up to 1073 K, inconsistent with the expected behaviour, but the release peak was also shifted to a temperature higher than T_P for the 5 K/min ramping. However, almost 76% of the implanted helium was desorbed at $T > 1073$ K. This would still imply that migration and coalescence did take place, but that bubble nucleation may have occurred in the implant zone rather than at the oxide interface, hence the longer waiting period and the higher temperature for the helium release.

From the two investigated models, it is reasonable to assert that the transition in the nature of the helium trapping is controlled by migration to a boundary surface. This surface acts as a vacancy source, providing the rate-limiting mechanism for bubble growth and the subsequent helium release at higher temperatures is controlled by detrapping from the formed bubbles. The effect of the surface corrosion layer on the helium desorption characteristics will be further examined in section 5.5.

5.4. High temperature implantations

Thermal desorption was carried out for beryllium samples implanted with 2.5×10^{20} 30 keV He^+/m^2 at 600 K (0.38 T_m) and 773 K (0.49 T_m). Release curves for both sets of implantations are given in figs. 5.27 and 5.28, respectively. When helium implantations are done at high temperatures, the radiation-produced point defects will be in a dynamic state of production and annihilation concurrent with the gradual introduction of helium. Consequently, less frequent trapping and more detrapping of helium are expected as well as more overall helium mobility. However, from the helium re-emission data quoted in section 3.4, it seems reasonable to expect 100% retention during the implantation for these temperatures and this fluence.

Sample surfaces were examined by SEM after both implantations and, as shown in fig. 5.29, a difference in shade between the implanted and unimplanted surfaces is the only observed change, similar to the room temperature

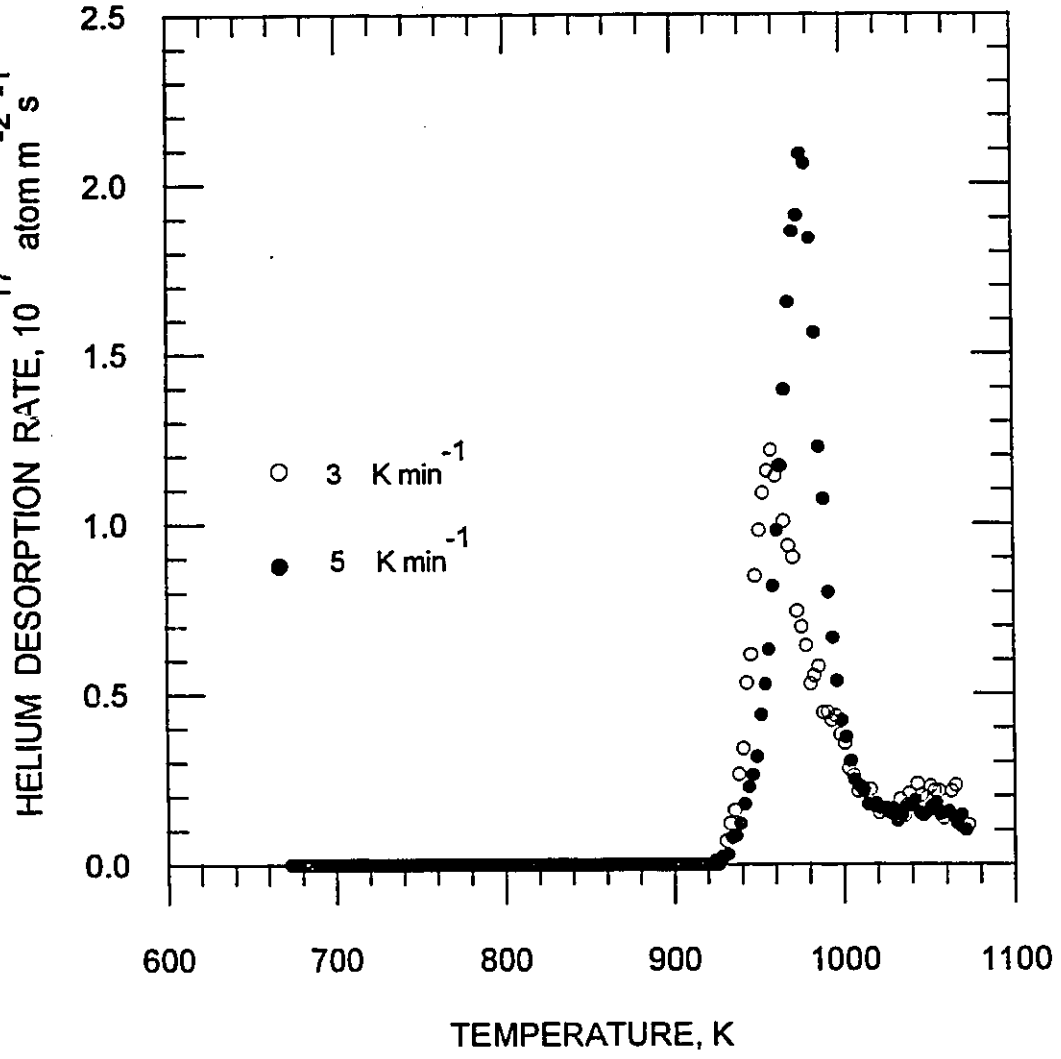

Fig. 5.27. Thermal desorption spectra for 30 keV helium implanted beryllium. Implantations were carried out at 600 K to a total fluence of 2.5×10^{20} m^{-2}.

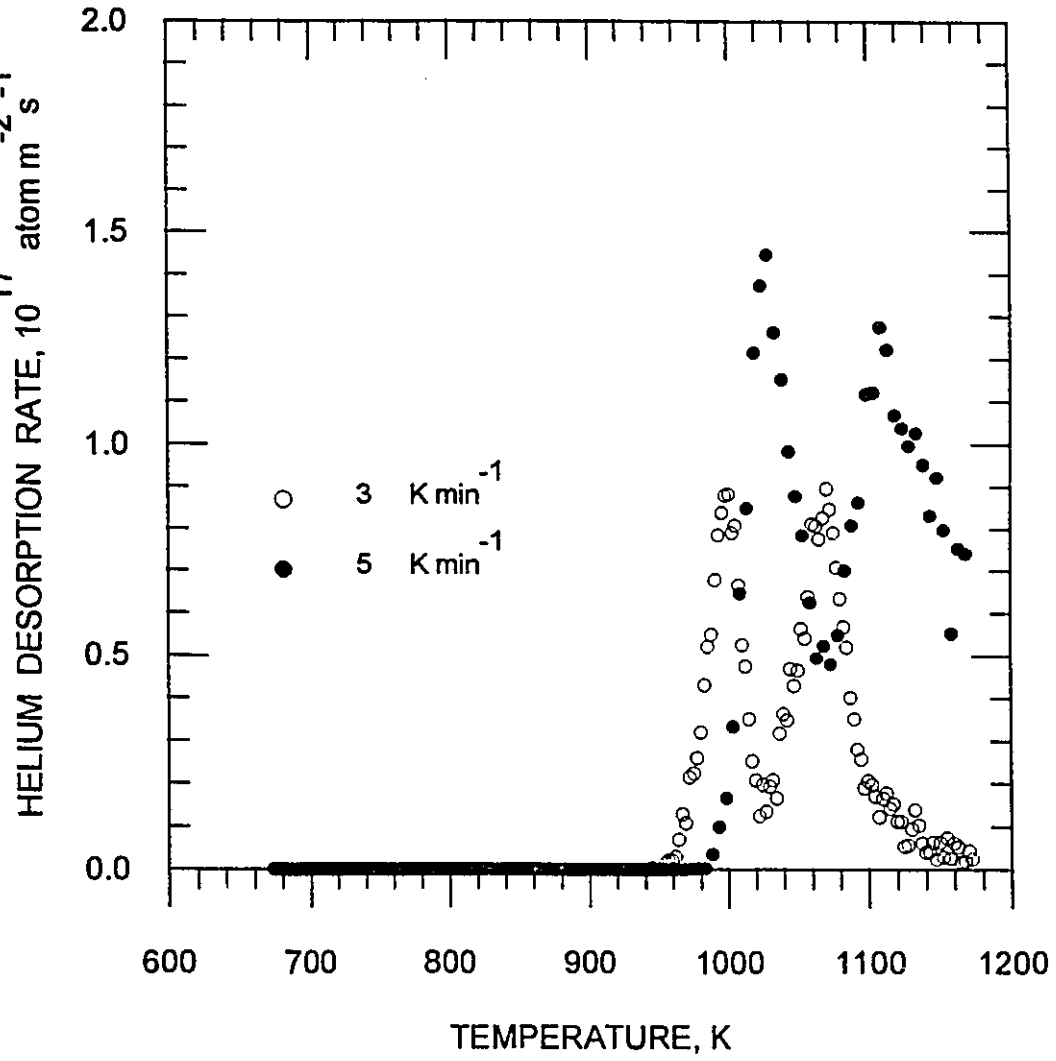

Fig. 5.28. Thermal desorption spectra for 30 keV helium implanted beryllium. Implantations were carried out at 773 K to a total fluence of 2.5×10^{20} m^{-2}.

implantations (fig. 5.13). It should be noted, though, that the surfaces implanted at high temperature appeared to be cleaner after the implantation, *i.e.*, the surface has retained the mirror-like reflectivity obtained at the end of the polishing stage and the mark left by the implantation clamp was difficult to see.

The desorption spectra for the 600 K implantations show the formation of one desorption peak, with T_P =960 K at 3 K/min and 980 K at 5 K/min, after which the desorption rate does not drop to zero. The lower ramping rate spectrum yields a relatively smaller second peak around 1050 K. For the 773 K implantations, the release curves show the formation of two distinct peaks, both at higher temperatures than the T_P values for the 600 K implantation. The threshold temperature for helium release has been found to increase with the implantation temperature. Figure 5.30 shows typical SEM images for a desorbed beryllium surface from the set implanted at 600 K. The main topographical feature is the formation of holes with an average diameter of 0.23 μm and an average density of $\approx 10^{11}$ m^{-2}. These holes are not limited, as in the micrographs discussed in the last two sections, to the implanted region, but extend (with a sharply lower density) to the unimplanted region as well. It is obvious in some areas, where the hole density is above average, that cracking has resulted in connections between the forming holes.

The same argument made in section 5.3 about higher temperature peaks being associated with more stable trapping forms is valid for this case. The high-temperature implantation would result in diffusion-broadening of the implantation profile and therefore a reduction in the peak helium concentration. Since helium

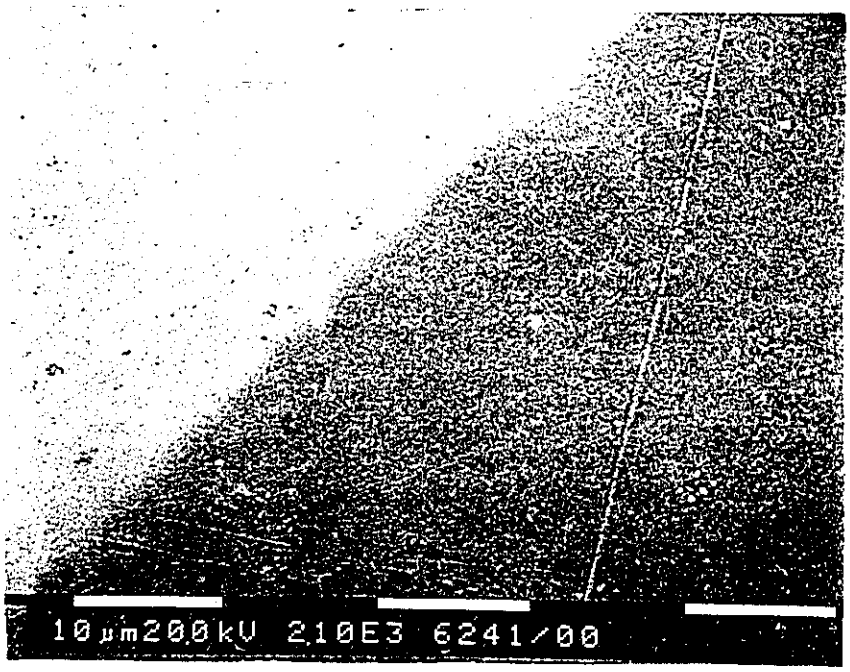

Fig. 5.29. SEM micrograph of a beryllium surface implanted with 2.5×10^{20} 30 keV He/m^2 at 773 K. The lighter shade marks the unimplanted part of the surface.

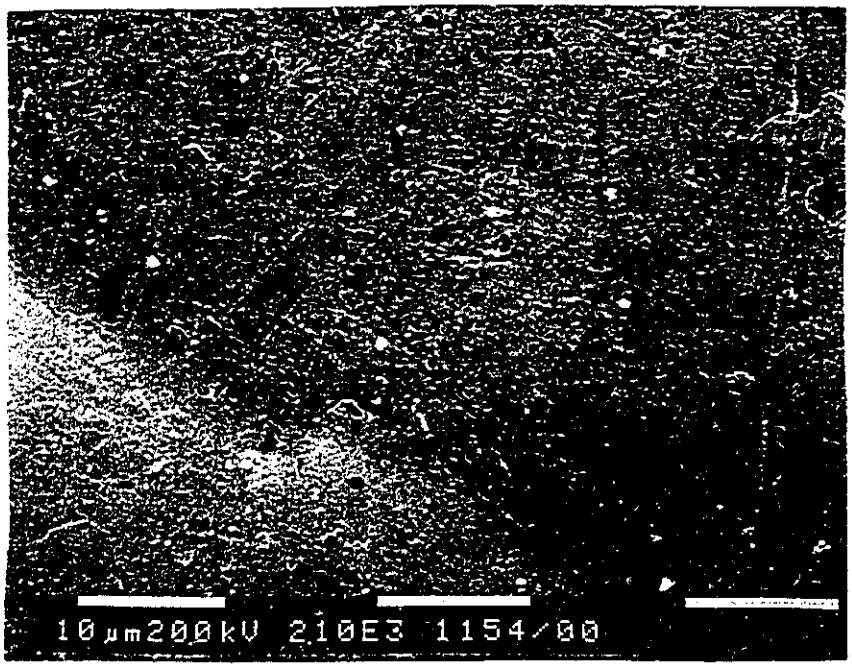

(a)

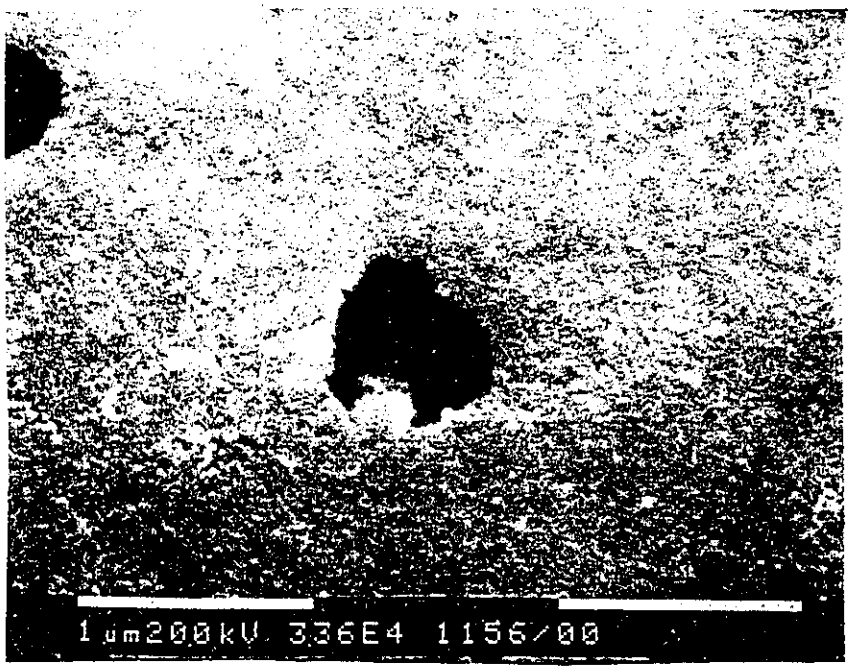

(b)

Fig. 5.30. (a) Typical SEM micrographs of a desorbed beryllium surface that was implanted with 30 keV helium ions at elevated temperatures. This image is for a sample implanted at 600 K and subsequently heated up to 1073 K; (b) the implanted surface at higher magnification.

can diffuse during the implantation, precipitation into gas bubbles is expected to occur. The rate of precipitation is proportional to the concentration of the gas and to the helium diffusion coefficient. Upon annealing the samples, these bubbles start to grow via the thermal vacancy absorption mechanism. Agglomeration however would not be as efficient as in the case of step-annealing desorption due to the widening of the helium distribution and the lower diffusivity of the growing bubbles. The formation of holes on the desorbed surface suggests that helium is released by the opening of helium bubbles at the surface. Implanted helium desorption at high temperatures has been ascribed to hole formation in the surfaces of nickel [Ehrenberg *et al.* 1983], copper [Johnson *et al.* 1980] and silver [Yamauchi *et al.* 1992]. For these three metals, the desorption was believed to be the result of bubble growth by thermal vacancy absorption mechanism.

A possible explanation for the double-peak structure of the spectra obtained from the 773 K implantations may be that the free surface acts as a source for thermal vacancies while the helium microbubbles are formed in two or more subsequent layers (see section 2.6.5). Vacancies diffusing from the surface would be absorbed in the closest layer, allowing a substantial degree of growth of the bubbles in that layer until the bubbles intersect the surface. Subsequently, desorption could take place from the deeper layers either by the formation of an interconnected network of cavities or by diffusion of thermal vacancies from the new surface. Such a mechanism can also explain the increase in population of the high temperature peak when the helium implantation was at 773 K, where the helium atoms are more mobile and therefore would precipitate

with higher concentrations into the deeper traps.

More helium is retained upon post-implantation annealing of a low-temperature implant ($\approx$ 62% at room temperature) than by direct implantation at higher temperatures ($\approx$ 47% at 773 K). This is another indication of the effect of the mobility of both the helium atoms and the radiation produced defects during the implantation. Similar behaviour has been also reported for other metals [Roth *et al.* 1976] and is expected to result from the change in the nature of helium trapping to bubbles when helium is implanted at elevated temperatures.

5.5. Effect of surface corrosion on desorption

Figure 5.31 shows thermal desorption curves for beryllium samples with deliberately corroded surfaces (see section 4.1) that were implanted at room temperature to a total fluence of 10^{21} He^+/m^2. When compared to fig. 5.5, the corroded surfaces show the presence of an additional broad high temperature desorption peak that was not detected for the "clean" surface. The other two peaks correspond reasonably well to the primary and secondary peaks analyzed in detail in section 5.2.

The broad additional peak could be ascribed to diffusion-limited release through the surface oxide. This layer, as mentioned in section 4.1, had a non-uniform thickness and therefore the formation of the primary and secondary desorption peaks was still possible if part of the detrapped helium from the

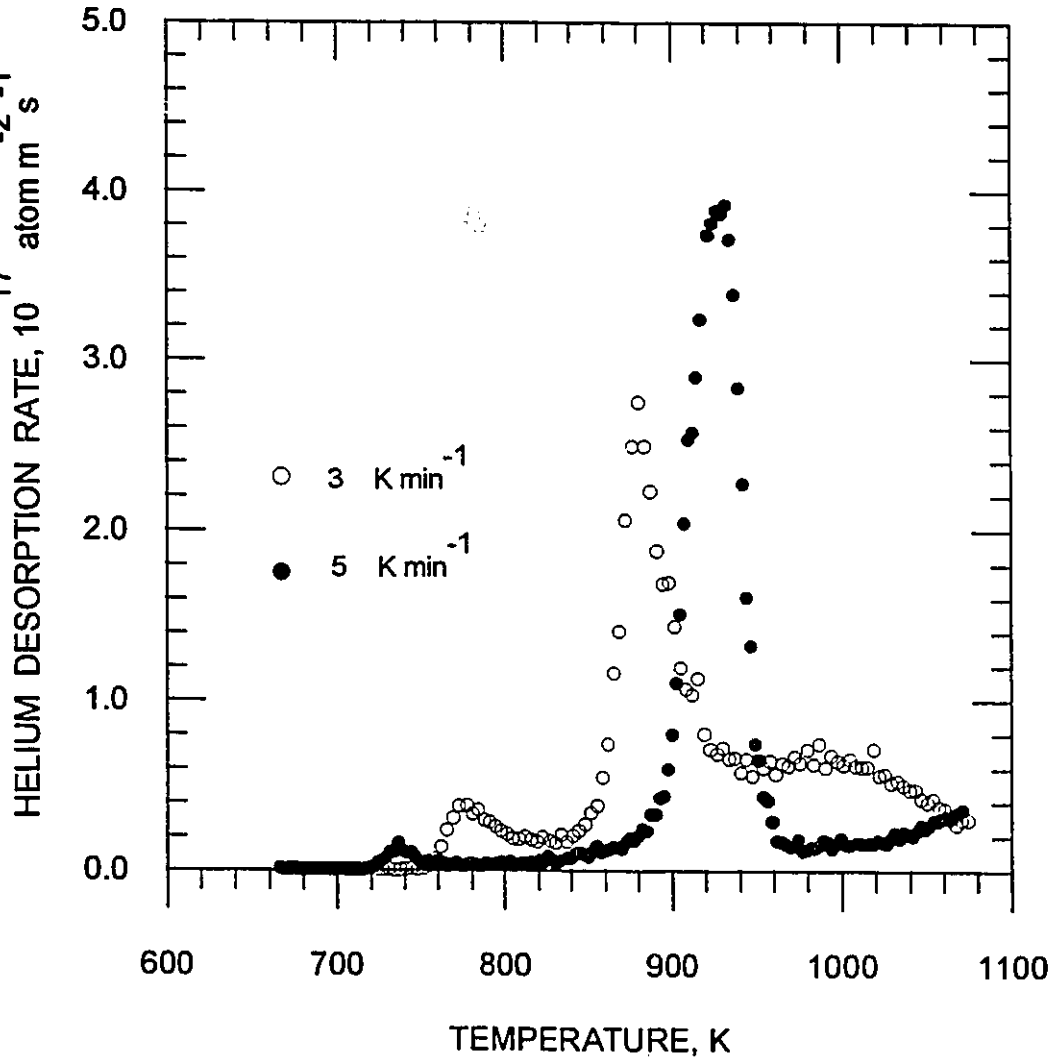

Fig. 5.31. Thermal desorption spectra for 30 keV helium implanted beryllium to a total fluence of 10^{21} He^+/m^2. Before implantation, the samples were deliberately corroded.

material bulk diffuses out of the thinner oxide layer. However, a fraction of the desorbed helium is expected to accumulate below the surface areas with thicker oxide. Surface effects are not new phenomena in helium release measurements from metals. Helium accumulation was first reported in the oxide surface layer of another hcp metal (α-Zr) when implanted with 200 keV beam and the depth profile measured at different temperatures between 300 and 898 K [Lewis *et al.* 1986]. Similar observations were also made in titanium, another hcp metal [Lewis 1987].

Two more comments can be made about fig. 5.31 that are directly related to the presence of a thick surface corrosion layer. First, the values of T_P for both the primary and secondary peaks were shifted to higher values for the corroded surfaces. For example T_P for the 5 K/min desorbed samples was observed at 887 and 723 K for the uncorroded samples, compared to 929 and 739 K for the corroded ones. Second, the integrated areas under each peak are considerably smaller for the corroded samples. The population of the primary peak in the case of corroded surfaces was down to 18% from 25% in the case of clean surfaces and the population of the secondary peak was at 0.5% compared to 1.1%. All percentages are relative to the implantation fluence. Both observations strongly indicate that the surface contaminants act as a diffusion barrier that delays the helium release significantly.

Such a mechanism is in a sense similar to the one reported in section 5.3 (surface layer delaying the helium release). They differ however in the nature of the migrating helium. In the case of step-annealing desorption, helium is in a

bubble form that agglomerates at the bulk/surface interface while in the case of the corroded surface implantations, helium is diffusing in its atomic form out of the bulk material, then is re-trapped in the surface layer. Its desorption, as judged by the width of the release tail, is controlled by a diffusion mechanism.

CHAPTER 6

Conclusions

In the present work, the thermal desorption behaviour of helium and related surface morphology changes have been investigated for 30 keV ^{4}He ion-implanted beryllium. To the best of the author's knowledge, this is the first systematic investigation of ion-implanted helium in beryllium. It proves how useful the experimental techniques of thermal desorption spectroscopy and scanning electron microscopy are in detecting the evolution of helium-related defects in beryllium.

The obtained results for beryllium are, in general, consistent with observations made for the behaviour of helium in other metals. However, the quantitative analysis for the detrapping energies is the first made for beryllium and the ageing phenomenon, both at 300 and 77 K, is the first ever reported for helium-implanted metals. The main results of the present work are summarized as follows:

1. Thermal desorption of implanted helium from beryllium has a strong dependence on the implantation fluence. The binding energy of the traps appears to increase at lower helium fluences, to the extent that for peak concentrations below 0.11 at%, complete retention is achieved at up to 80% of the melting temperature.

2. For the range of fluences investigated, helium thermal release takes place in two distinct regions. The amount of helium released was less than the implanted fluence, suggesting the presence of at least one more trapping site with a dissociation energy greater than 3 eV.

3. The primary desorption peak has a peak temperature higher than 890 K and is characterized by an activation energy that varies with the helium population so as to increase the trapping efficiency at lower implantation fluences.

4. The desorption curves for the 7.5×10^{20} and 10^{21} 30 keV He^{+}/m^{2} implants reveal two well-separated identifiable peaks. In the case of the highest fluence there is a drop in the population of the primary desorption peak. The evolution of this feature indicated that the filling of the secondary trapping site (with a maximum desorption temperature below 830 K) may be related to

the saturation of the primary trapping site.

5. For the intermediate fluences, prior to the formation of the secondary peak, the desorption spectra display a dependence on the room temperature ageing of the implanted samples. The primary desorption peak seems to incorporate a number of closely adjacent trapping sites that become distinguishable only when temperature is ramped slowly enough; < 5 K/min.

6. All of the samples implanted at room temperature show the same surface morphology changes after desorption. This indicates that helium release is governed by the same dissociative mechanism, independent of the implantation fluence.

7. Step-anneal helium release curves showed the formation of only one desorption peak at temperatures higher than 1050 K. The release peak was inferred to be the result of helium detrapped from bubbles grown by the migration and coalescence mechanism.

8. When helium is implanted at high temperatures, the desorption curves indicated that the helium resides in more stable traps. In this case, helium desorption was inferred to result from small helium bubble growth by the thermal vacancy assisted mechanism.

9. The presence of surface films containing oxygen and carbon acts as a diffusion barrier, delaying the helium release. This was seen in deliberately corroded samples, as well as in the samples desorbed by step-annealed desorption regime.

It might be useful for future investigations of helium effects in beryllium to expand the present work to map the fluence range investigation to elevated temperatures. If the ion implantations were to be carried out using thin beryllium films, the evolution of helium bubble deposition and growth would be easily accessible. Also, of primary importance to the fusion technology is to study the synergistic effects for the presence of helium together with hydrogen isotopes. For beryllium, the only system that was extensively studied was the helium-tritium one. The role played by the presence of deuterium in stabilizing the helium defects and vice versa is another interesting area to be examined.

BIBLIOGRAPHY

Baldwin, D.L., Slagle, O.D. and Gelles, D.S. "Tritium Release from Irradiated Beryllium at Elevated Temperatures", Journal of Nuclear Materials, 179-181 (1991), 329-334.

Barnes, R.S., Redding, G.B. and Cottrell, A.H. "The Observation of Vacancy Sources in Metals", Philosophical Magazine, 3 (1958), 97-99.

Barnes, R.S. and Redding, G.B. "The Behaviour of Helium Atoms Injected into Beryllium", Journal of Nuclear Energy A, 10 (1959), 32-35.

Barnes, R.S. "The Generation of Vacancies in Metals", Phil. Mag., 5 (1960), 635-646.

Barnes, R.S. and Mazey, D.J. "The Migration and Coalescence of Inert Gas Bubbles in Metals", Proceedings of the Royal Society A, 275 (1963), 47-57.

Baskes, M.I. and Wilson, W.D. "A Statistical Model of Low Temperature Blister Formation in Helium-Implanted Metals", Radiation Effects, 37 (1978), 93-98.

Baskes, M.I. and Melius, C.F. "Pair Potentials for FCC Metals", Physical Review B, 20 (1979), 3197-3204.

Baskes, M.I., Fastenau, R.H.J., Penning, P., Caspers, L.M. and van Veen, A. "On the Low-Temperature Nucleation and Growth of Bubbles by Helium Bombardment of Metals", J. Nucl. Mater., 102 (1981), 235-245.

Baskes, M.I. and Wilson, W.D. "Kinetics of Helium Self-Trapping in Metals", Phys. Rev. B, 27 (1983), 2210-2217.

Bauer, W. and Thomas, G.J. "Helium Release and Electron-Microscopy of Helium-Implanted Palladium", J. Nucl. Mater., 42 (1972), 96-100.

Biersack, J.P. and Haggmark, L.G. "A Monte Carlo Computer Program for the Transport of Energetic Ions in Amorphous Targets", Nuclear Instruments and Methods, 174 (1980), 257-269.

Brailsford, A.D. and Bullough, R. "The Stress Dependence of High Temperature Swelling", J. Nucl. Mater., 48 (1973), 87-106.

Carter, G. "Thermal Resolution of Desorption Energy Spectra", Vacuum, 12 (1962), 245-254.

Carter, G., Armour, D.G., Donnelly, S.E., Ingram, D.C. and Webb, R.P. "The Injection of Inert Gas Ions into Solids: Their Trapping and Escape", Rad. Eff., 53 (1980), 143-174.

Caspers, L.M., van Veen, A., van Gorkum, A.A., van den Beukel, A. and van Baal, C.M. "Helium Desorption from a (110) Mo Crystal", Physics Status Solidi (A), 37 (1976), 371-383.

Caspers, L.M., Fastenau, R.H.J., van Veen, A. and van Heugten, W.F.W.M. "Mutation of Vacancies to Divacancies by Helium Trapping in Molybdenum", Phys. Stat. Sol. (A), 46 (1978), 541-546.

Caspers, L.M., Ympa, M.R., van Veen, A. and van der Kolk, G.J. "The Atomistics of Helium Bubble Nucleation in B.C.C. Metals", Phys. Stat. Sol. (A), 63 (1981), K183-K188.

Chan, C.-M., Aris, R. and Weinberg, W.H. "An Analysis of Thermal Desorption Mass Spectra. I.", Applications of Surface Science, 1 (1978), 360-376.

Chernikov, V.N., Trinkaus, H., Jung, P. and Ullmaier, H. "The Formation of Helium Bubbles near the Surface and in the Bulk in Nickel during Post-Implantation Annealing", J. Nucl. Mater., 170 (1990), 31-38.

Cottrell, A.H. An Introduction to Metallurgy. London: Edward Arnold, 1967.

Crank, J. The Mathematics of Diffusion. Oxford: Clarendon Press, 1979.

Dalle Donne, M., Scaffidi-Argentina, F., Ferrero, C. and Ronchi, C. "Modelling of Swelling and Tritium Release in Irradiated Beryllium", J. Nucl. Mater., 212-215 (1994), 954-960.

Das, S.K., Kaminsky, M. and Fenske, G. "The Significance of a Correlation of Blister Diameter with Skin Thickness for Ni and Be for Blistering Models", J. Nucl. Mater., 76 & 77 (1978), 215-220.

Das, S.K., Kaminsky, M. and Fenske, G. "On the Correlation of Blister Diameter and Blister Skin Thickness in Helium-Ion-Irradiated Nb", Journal of Applied Physics, 50 (1979), 3304-3311.

Das, S.K. "The Role of Inert Gases in First Wall Phenomena in Fusion Devices", Rad. Eff., 53 (1980), 257-266.

Delaplace, J., Nicoud, J.C., Schumacher, D. and Vogl, G. "Low-Temperature Neutron Radiation Damage and Recovery in Beryllium", Phys. Stat. Sol., 29 (1968), 819-824.

Donnelly, S.E., Lucas, A.A., Vigneron, J.P. and Rife, J.C. "The Density of Helium in Bubbles in Implanted Materials: Results from VUV Absorption and EEL Spectroscopy", Rad. Eff., 78 (1983), 337-347.

Donnelly, S.E. "The Density and Pressure of Helium in Bubbles in Implanted Metals: A Critical Review", Rad. Eff., 90 (1985), 1-47.

Dupouy, J.-M., Mathie, J. and Adda, Y. "Autodiffusion du Béryllium", Mémoires Scientifiques Revue Métallurgique, LXIII (1966), 481-487.

Edwards, D. Jr. and Kornelsen, E.V. "The Kinetics of the Desorption of Helium Implanted into a Nickel (100) Crystal", Surface Science, 44 (1974), 1-10.

Edwards, D. Jr. "Peak Widths of Elementary First and Second Order Desorption Transients", Surface Sci., 54 (1976), 1-5.

EerNisse, E.P. and Picraux, S.T. "Role of Integrated Lateral Stress in Surface Deformation of He-Implanted Surfaces", J. Appl. Phys., 48 (1977), 9-17.

Ehrenberg, J., Scherzer, B.M.U. and Behrisch, R. "Thermal Desorption Spectroscopy of He from Ni at and below Saturation", Rad. Eff., 78 (1983), 405-416.

Ehrlich, G. "Kinetic and Experimental Basis of Flash Desorption", J. Appl. Phys., 32 (1961), 4-15.

Eleveld, H., van Veen, A., Labohm, F. and de Moor, M.W. "Thermal Desorption of Helium Irradiated Beryllium Studied by THDS, NDP, PA and SEM", J. Nucl. Mater., 212-215 (1994a), 971-975.

Eleveld, H., van Veen, A., Clement, M. and de Moor, M.W. "Helium Deffect Interactions in Vanadium and Beryllium", Plasma Devices and Operations, 3 (1994b), 65-78.

Evans, J.H. "An Interbubble Fracture Mechanism of Blister Formation on Helium-Irradiated Metals", J. Nucl. Mater., 68 (1977), 129-140.

Evans, J.H. "The Role of Implanted Gas and Lateral Stress in Blister Formation Mechanisms", J. Nucl. Mater., 76 & 77 (1978), 228-234.

Evans, J.H., van Veen, A. and Caspers, L.M. "Direct Evidence for Helium Bubble Growth in Molybdenum by the Mechanism of Loop Punching", Scripta Metallurgica, 15 (1981), 323-326.

Falconer, J.L. and Schwarz, J.A. "Temperature-Programmed Desorption and Reaction: Applications to Supported Catalysts", Catalysis Review: Science and Engineering, 25 (1983), 141-227.

Farrell, G. and Carter, G. "Diffusive Processes in a Solid During Tempering", Vacuum, 17 (1967), 15-19.

Fastenau, R.H.J., Caspers, L.M. and van Veen, A. "Small Clusters of Vacancies and Helium in Molybdenum", Phys. Stat. Sol. (A), 34 (1976), 277-289.

Foreman, A.J.E. and Singh, B.N. "Gas Diffusion and Temperature Dependence of Bubble Nucleation during Irradiation", J. Nucl. Mater., 141-143 (1986), 672-676.

Foreman, A.J.E., English, C.A. and Phythian, W.J. "Molecular Dynamics Calculations of Displacement Threshold Energies and Replacement Collision Sequences in Copper Using a Many-Body Potential", Phil. Mag. A, 66 (1992), 655-669.

Ghoniem, N.M., Sharafat, S., Williams, J.M. and Mansur, L.K. "Theory of Helium Transport and Clustering in Materials under Irradiation", J. Nucl. Mater., 117 (1983), 96-105.

Gibson, J.B., Goland, A.N., Milgram, M. and Vineyard, G.H. "Dynamics of Radiation Damage", Phys. Rev., 120 (1960), 1229-1253.

Glasgow, B.B. and Wolfer, W.G. "Comparison of Mechanisms for Cavity Growth by Athermal and Thermal Processes", J. Nucl. Mater., 122&123 (1984), 503-508.

Gmelin, E. "Diffusion et Precipitation de l'Helium dans l'Oxyde de Beryllium Irradie et Recuit", J. Nucl. Mater., 38 (1971), 150-162.

Goodhew, P.J. and Tyler, S.K. "Helium Bubble Behaviour in B.C.C. Metals below 0.65 T_m ", Proc. R. Soc. (London) A, 377 (1981), 151-184.

Greenwood, G.W., Foreman, A.J.E. and Rimmer, D.E. "The Role of Vacancies and Dislocations in the Nucleation and Growth of Gas Bubbles in Irradiated Fissile Material", J. Nucl. Mater., 1 (1959), 305-324.

Greenwood, G.W. and Speight, M.V. "An Analysis of the Diffusion of Fission Gas Bubbles and its Effect on the Behaviour of Reactor Fuels", J. Nucl. Mater., 10 (1963), 140-144.

Gruber, E.E. "Calculated Size Distributions for Gas Bubble Migration and Coalescence in Solids", J. Appl. Phys., 38 (1967), 243-250.

Habenschaden, E. and Küppers, J. "Evaluation of Flash Desorption Spectra", Surface Sci., 138 (1984), L147-L150.

Heinisch, H.L. and Singh, B.N. "On the Structure of Irradiation-Induced Collision Cascades in Metals as a Function of Recoil Energy and Crystal Structure", Phil. Mag. A, 67 (1993), 407-424.

Igarashi, M., Khantha, M. and Vitek, V. "*N*-Body Interatomic Potentials for Hexagonal Close-Packed Metals", Phil. Mag. B, 63 (1991), 603-627.

Jäger, W., Manzke, R., Trinkaus, H., Zeller, R., Fink, J. and Crecelius G. "The Density and Pressure of Helium in Bubbles in Metals", Rad. Eff., 78 (1983), 315-325.

Johnson, P.B. and Mazey, D.J. "The Gas-Bubble Superlattice and the Development of Surface Structure in He^+ and H^+ Irradiated Metals at 300 K", J. Nucl. Mater., 93 & 94 (1980), 721-727.

Jung, P. and Schroeder, K. "Diffusion and Agglomeration of Helium in FCC Metals", J. Nucl. Mater., 155-157 (1988), 1137-1141.

Jung, P. "Diffusion and Clustering of Helium in Noble Metals", Fundamental Aspects of Inert Gases in Solids. Edited by S.E. Donnelly and J.H. Evans. New York: Plenum Press, 1991, 59-66.

Jung, P. "Diffusion and Retention of Implanted Helium in Beryllium", J. Nucl. Mater., 202 (1993), 210-215.

Kaletta, D. "The Growth of Gas Bubbles in Solids under Irradiation at Elevated Temperatures around 0.5 T_m ", Rad. Eff., 78 (1983), 245-259.

Kelly, R. and Jech, Č. "Inert-Gas Diffusion as a Probe for Lattice Defects in Ionic Crystals", Proceedings of the British Ceramic Society, 9 (1967), 243-257.

King, D.A. "Thermal Desorption from Metal Surfaces: A Review", Surface Sci., 47 (1975), 384-402.

Konvalinka, J.A. and Scholten, J.J.F. "Sorption and Temperature-Programmed Desorption of Hydrogen from Palladium and from Palladium on Activated Carbon", Journal of Catalysis, 48 (1977), 374-385.

Kornelsen, E.V. "The Interaction of Injected Helium with Lattice Defects in a Tungsten Crystal", Rad. Eff., 13 (1972), 227-236.

Kornelsen, E.V. and Edwards, D. Jr. "Observation of Ion Bombardment Damage in a Ni (100) Crystal by Helium Ion Injection", Applications of Ion Beams to Metals. Edited by S.T. Picraux, E.P. EerNisse and F.L. Vook. New York: Plenum Press, 1974, 521-529.

Kornelsen, E.V. and van Gorkum, A.A. "A Study of Bubble Nucleation in Tungsten Using Thermal Desorption Spectrometry: Clusters of 2 to 100 Helium Atoms", J. Nucl. Mater., 92 (1980), 79-88.

Krauss, A.R., Auciello, O., Brooks, J.N., Mattas, R., McGrath, R., Nygren, R. and Smith, D.L. "Helium Pumping Strategies for D-T Fusion Devices", MRS Bulletin, (July 1990), 47-49.

Langley, R.A. "Interaction of Implanted Deuterium and Helium with Beryllium: Radiation Enhanced Oxidation", J. Nucl. Mater., 85 & 86 (1979), 1123-1126.

Lewis, M.B. and Farrell, K. "Migration Behaviour of Helium under Displacive Irradiation in Stainless Steel, Nickel, Iron and Zirconium", Nuclear Instruments and Methods in Physics Research, B16 (1986), 163-170.

Lewis, M.B. "Diffusion and Trapping of Ion-Implanted Helium in Nickel", J. Nucl. Mater., 149 (1987), 143-149.

Macaulay-Newcombe, R.G., Thompson, D.A. and Smeltzer, W.W. "Deuterium Diffusion, Trapping and Release in Ion-Implanted Beryllium", Fusion Engineering and Design, 18 (1991), 419-424.

Manuaba, A., Pászti, F. and Kótai, E. "Experimental Investigation of the Channel Network Formed by High-Dose He Implantaion", J. Nucl. Mater., 175 (1990), 158-162.

Manzke, R., Jäger, W., Trinkaus, H., Crecelius, G., Zeller, R. and Fink, J. "Quantitative Determination of the Pressure of He in Bubbles in Al and Ni", Solid State Communications, 44 (1982), 481-484.

Mills, R.L., Liebenberg, D.H. and Bronson, J.C. "Equation of State and Melting Properties of ^{4}He from Mesurements to 20 kbar", Phys. Rev. B, 21 (1980), 5137-5148.

Marochov, N., Perryman, L.J. and Goodhew, P.J. "Growth of Inert Gas Bubbles after Implantation", J. Nucl. Mater., 149 (1987), 296-301.

Nelson, R.S. "The Stability of Gas Bubbles in an Irradiation Environment", J. Nucl. Mater., 31 (1969), 153-161.

Niemantsverdriet, J.W., Dolle, P., Market, K. and Wandelt, K. "Thermal Desorption of Strained Monoatomic Ag and Au Layers from Ru (001)", Journal of Vacuum Science and Technology A, 5 (1987), 875-878.

Niwase, K., Ezawa, T., Tanabe, T. and Fujita, F.E. "Obsrvation of Micro-Cavities in Nickel during He^+ and D^+ Irradiation and Post-Irradiation Annealing", J. Nucl. Mater., 160 (1988), 229-241.

Peterson, N.L. "Self-Diffusion in Pure Metals", J. Nucl. Mater., 69 & 70 (1978), 3-37.

Philipps, V., Sonnenberg, K. and Williams, J.M. "Diffusion of Helium in Nickel", J. Nucl. Mater., 107 (1982), 271-279.

Philipps, V. and Sonnenberg, K. "Interstitial Diffusion of He in Nickel", J. Nucl. Mater., 114 (1983), 95-97.

Picraux, S.T. "Defect Trapping of Gas Atoms in Metals", Nucl. Inst. and Meth., 182/183 (1981), 413-437.

Pisani, C., Rabino, G. and Ricca, F. "Statistical Analysis and Model Determination for Thermal Desorption Spectra: Nitrogen on Tungsten", Surface. Sci., 41 (1974), 277-292.

Poker, D.B. "Release of Ion-Implanted and Transmutation-Produced Helium from Nickel", Rad. Eff., 78 (1983), 101-104.

Pontau, A.E., Bauer. W. and Conn, R.W. "He Pumping in the Presence of an H Beam", J. Nucl. Mater., 93 & 94 (1980), 564-568.

Redhead, P.A. "Thermal Desorption of Gases", Vacuum, 12 (1962), 203-211.

Reed, D.J. "A Review of Recent Theoretical Developments in the Understanding of the Migration of Helium in Metals and its Interaction with Lattice Defects", Rad. Eff., 31 (1977), 129-147.

Riehm, M. P. The Diffusion and Solution of Hydrogen Isotopes in Solids and the Development of a Hydrogen Permeation Barrier. Hamilton: McMaster University, 1990.

Rimmer, D.E. and Cottrell, A.H. "The Solution of Inert Gas Atoms in Metals", Phil. Mag., 2 (1957), 1345-1353.

Ross, G. and Terreault, B. "Dommage de Surface et Profiles de Teneur en Gaz Piégé dans le Béryllium sous Irradiation d'He^+ de 20 keV", J. Nucl. Mater., 89 (1980), 383-391.

Roth, J., Picraux, S.T., Eckstein, W., Bøttiger, J. and Behrisch, R. "Temperature Dependence of He Trapping in Niobium", J. Nucl. Mater., 63 (1976), 120-125.

Sannen, L., de Raedt, Ch., Moons, F. and Yao, Y. "Helium Content and Induced Swelling of Neutron Irradiated Beryllium", Fusion Eng. Des., 29 (1995), 470-474.

Schilling, W. "Diffusion of Helium in Metals", Point Defects and Defect Interactions in Metals. Edited by J.-I. Takamura, M. Doyama and M. Kiritani. Tokyo: University of Tokyo Press, 1982, 303-308.

Sciani, V. and Jung, P. "Diffusion of Helium in FCC Metals", Rad. Eff., 78 (1983), 87-99.

Seitz, F. "Prismatic Dislocations and Prismatic Punching in Crystals", Phys. Rev., 79 (1950), 723-724.

Shi, S.-Q. Permeation and Thermal Desorption Studies of Deuterium Diffusion and Trapping in Ion-Implanted Nickel. Hamilton: McMaster University, 1991.

Thomas, G.J., Swansiger, W.A. and Baskes, M.I. "Low-temperature Helium Release in Nickel", J. Appl. Phys., 50 (1979), 6942-6947.

Thomas, G.J. and Bastasz, R. "Direct Evidence for Spontaneous Precipitation of Helium in Metals", J. Appl. Phys., 52 (1981), 6426-6428.

Thomas, G.J. "Experimental Studies of Helium in Metals", Rad. Eff., 78 (1983), 37-51.

Thomas, P.R. and The JET Team "Results of JET Operation with Beryllium", J. Nucl. Mater., 176 &177 (1990), 3-13.

Trinkaus, H. "Precipitation of Helium and its Effects on Mechanical Properties of Metals", Point Defects and Defect Interactions in Metals. Edited by J.-I. Takamura, M. Doyama and M. Kiritani. Tokyo: University of Tokyo Press, 1982, 312-318.

Trinkaus, H. "Energetics and Formation Kinetics of Helium Bubbles in Metals", Rad. Eff., 78 (1983), 189-211.

Trinkaus, H., Singh, B.N. and Foreman, A.J.E. "Influence of Cascade Damage on Helium Diffusion and Bubble Nucleation", J. Nucl. Mater., 174 (1990 a), 80-85.

Trinkaus, H. "Possible Effects of Collision Cascades on Bubble and Void Nucleation in Metals", J. Nucl. Mater., 174 (1990 b), 178-189.

Tyler, S.K. and Goodhew, P.J. "Direct Evidence for the Brownian Motion of Helium Bubbles", J. Nucl. Mater., 92 (1980), 201-206.

Ullmaier, H. "Helium in Metals", Rad. Eff., 78 (1983), 1-10.

van Veen, A., van Gorkum, A.A., Caspers, L.M., Nihoul, J., Stals, L. and Cornelis, J. "Helium desorption from a Molybdenum Single Crystal", Phys. Stat. Sol. (A), 32 (1975), K123-K126.

van Veen, A., Caspers, L.M., Kornelsen, E.V., Fastenau, R., van Gorkum, A. and Warnaar, A. "Vacancy Creation by Helium Trapping at Substitutional Krypton in Tungsten", Phys. Stat. Sol. (A), 40 (1977), 235-246.

Vassen, R., Trinkaus, H. and Jung, P. "Diffusion of Helium in Magnesium and Titanium before and after Clustering", J. Nucl. Mater., 183 (1991), 1-8.

Verbeek, H. and Eckstein, W. "Radiation Blistering after H^+ , D^+ and He^+ Ion-Implantation into Surfaces of Stainless Steel, Mo and Be", Applications of Ion Beams to Metals. Edited by S.T. Picraux, E.P. EerNisse and F.L. Vook. New York: Plenum Press, 1974, 597-610.

Wiedersich, H., Burton, J.J. and Katz, J.L. "Effect of Mobile Helium on Void Nucleation in Materials During Irradiation", J. Nucl. Mater., 51 (1974), 287-301.

Wiedersich, H. and Hall, B. O. "Effect of Mobile Helium on Void Nucleation", J. Nucl. Mater., 66 (1977), 187-192.

Wilson, K.L., Thomas, G.J. and Bauer, W. "The Response of Plasma-Sprayed Beryllium to He^+ Bombardment", Transactions of the American Nuclear Society, 27 (1977), 272-273.

Wilson, K.L., Causey, R.A., Hsu, W.L., Mills, B.E., Smith, M.F. and Whitley, J.B. "Beryllium-a Better Tokamak Plasma-Facing Material?", J. Vac. Sci. Technol. A, 8 (1990), 1750-1759.

Wilson, W.D. and Bisson, C.L. "Inert Gases in Solids: Interatomic Potentials and their Influence on Rare-Gas Mobility", Phys. Rev. B, 3 (1971), 3984-3992.

Wilson, W.D. and Johnson, R.A. "Rare Gases in Metals", Interatomic Potentials and Simulation of Lattice Defects. Edited by P.C. Gehlen, J.R. Beeler, Jr. and R.I. Jaffee. New York: Plenum Press, 1972, 375-390.

Wilson, W.D. and Bisson, C.L. "Atomistics of Helium Diffusion in Copper and Tungsten", Rad. Eff., 19 (1973), 53-58.

Wilson, W.D. and Bisson, C.L. "Rare Gas Complexes in Tungsten", Rad. Eff., 22 (1974), 63-66.

Wilson, W.D., Bisson, C.L. and Baskes, M.I. "Self-Trapping of Helium in Metals", Phys. Rev. B, 24 (1981), 5616-5624.

Winterbottom, W.L. "Application of Thermal Desorption Methods in Studies of Catalysis", Surface Sci., 37 (1973), 195-204.

Yamauchi, T., Yamanaka, S. and Miyake, M. "Thermal Release Behavior of Helium Implanted into Silver", J. Nucl. Mater., 189 (1992), 217-221.

Yoshida, N., Xu, Q., Watanabe, H., Miyamoto, Y. and Muroga, T. "Effect of Cyclic Temperature Change on Microstructural Evolution in Austentic Steels under Fission Neutron Irradiation", J. Nucl. Mater., 212-215 (1994), 417-475.

Zelenskij, V.F., Neklyudov, I.M., Ruzhitskij, V.V., Rybalko, V.F., Bendikov, V.I. and Khazan, S.M. "Thermal Desorption of Helium from Polycrystalline Ni Irradiated to Fluences Ranging from 1×10^{17} to 1×10^{18} He/cm^2 ", J. Nucl. Mater., 151 (1987), 22-33.